Title
High-fidelity operation of a radioactive trapped-ion qubit, ^{133}Ba$^+$

Author
Christensen, Justin

Publication Date
2020

Peer reviewed|Thesis/dissertation

UNIVERSITY OF CALIFORNIA
Los Angeles

High-fidelity operation of a radioactive trapped ion qubit, $^{133}Ba^{+}$

A dissertation submitted in partial satisfaction
of the requirements for the degree
Doctor of Philosophy in Physics

by

Justin E. Christensen

2020

ABSTRACT OF THE DISSERTATION

High-fidelity operation of a radioactive trapped ion qubit, $^{133}Ba^{+}$

by

Justin E. Christensen
Doctor of Philosophy in Physics
University of California, Los Angeles, 2020
Professor Eric R. Hudson, Chair

$^{133}Ba^{+}$ has been identified as an attractive ion for quantum information processing due to the unique combination of its spin-1/2 nucleus, visible wavelength electronic transitions, and long D-state lifetimes ($\tau \sim$1 min). Using a microgram source of radioactive material, we trap and laser-cool the synthetic $A = 133$ radioisotope of barium II ($\tau_{1/2} \approx 10.5$ yr) in a radio-frequency ion trap. To demonstrate high fidelity qubit operations, a number of unknown state energies were needed. We measure the isotope shift and hyperfine structure of the $6^2P_{1/2} \leftrightarrow 5^2D_{3/2}$ electronic transition needed for laser cooling, state preparation, and state detection of the clock-state hyperfine and optical qubits. For high-fidelity operations with electron shelving, we report measurements of the $6^2P_{3/2}$ and $5^2D_{5/2}$ hyperfine splittings, as well as the $6^2P_{3/2} \leftrightarrow 6^2S_{1/2}$ and $6^2P_{3/2} \leftrightarrow 5^2D_{5/2}$ transition frequencies. Using these transitions, we demonstrate high-fidelity $^{133}Ba^{+}$ hyperfine qubit manipulation with electron shelving detection to benchmark qubit state preparation and measurement (SPAM). Using single-shot, threshold discrimination, we measure an average SPAM fidelity of $\mathcal{F} = 0.99971(3)$, a factor of ≈ 2 improvement over the best reported performance of any qubit. Finally, we report the $6^2P_{1/2} \leftrightarrow 5^2D_{3/2}$ electronic transition isotope shift for the rare $A = 130$ and 132 barium nuclides, completing the spectroscopic characterization necessary for laser cooling all long-lived barium II isotopes.

The dissertation of Justin E. Christensen is approved.

HongWen Jiang

Paul Hamilton

Wesley C. Campbell

Eric R. Hudson, Committee Chair

University of California, Los Angeles

2020

To my parents and wife

for unconditional support and encouragement

TABLE OF CONTENTS

LIST OF FIGURES

LIST OF TABLES

ACKNOWLEDGMENTS

I like to think of life as a road map, you've got places to go, but there are an endless number of ways to get there. Sometimes you drive in a few circles, perhaps get a flat tire, or maybe take the "scenic" route (not always intentional...), but eventually you find your way.

It's hard for me to imagine that only 12 years ago, and already 25 years old, I was cleaning swimming pools in southern California, had never learned calculus, and was unaware my undergraduate university even existed. Nevertheless, with a lot of work, and a lot of help, I've been lucky enough to take part in a great experiment with a great community of people.

To my friends, we certainly did most of that driving in circles together, but the ride was worth it! The character that you all posses, dedication to our friendship, and years of good time past and to come I will always cherish. Stark, Copeland, Gaynor, Ryan, you guys are the best.

To my family, thanks for the unconditional love and support. Every child needs to believe they can do more, learn to accept defeat, and continue to push towards a better life. It is no understatement to say the foundation of my achievements begin atop your shoulders.

To Tony, I guess we'll never try for those magnetic monopoles! What a journey my friend. Endless hours upon endless days working and learning together. I am forever grateful for the help along the way, and the guidance to get me into a field I now feel like was always right. I can only say how happy I am for your success, and look forward to a lifelong friendship.

To Dave, well, you always said your goal was to become a useless postdoc.... Okay so you didn't quite make that goal, but you did give me the tools I needed to become successful. You always made it a priority to teach me something I didn't understand, and that is something only a lucky few get to experience. I am forever grateful. Also, Ohio State rules, Linux for life, Dave's money, and I am going to beat you at Tecmo Super Bowl one day.

To Eric, I really don't know what to say. Being a part of your group and working on the barium experiment has been the best experience of my life (except being with my wife of

course...). You've provided great leadership, knowledge, and always shown me a tremendous level of respect. Take it from someone with a little extra life experience, you are doing an amazing thing.

To my wife, boy oh boy, I still like to think about what your parents thought when you told them you were moving to Berkeley with me. I can't believe how much we've shared and done together over the last 11 years. You've seen me at my best and worst, and helped me realize one of my biggest dreams; I love you forever. I don't know how to describe what's next: A right turn? A road trip? Cruising with the top down? Either way our son will be a ride!

VITA

2009–2011	Moorpark College
2011	Summer Undergraduate Research Fellowship, Jet Propulsion Laboratory
2011–2013	B.A. Physics and B.A. Astrophysics, University of California Berkeley
2013	United States Particle Accelerator School (USPAS), Duke University
2013–present	University of California Los Angeles

PUBLICATIONS

Hucul, D., Christensen, J. E., Hudson, E. R., and Campbell, W. C. Spectroscopy of a synthetic trapped ion qubit. *Phys. Rev. Lett.* **119**, 100501 (2017)

Christensen, J. E., Hucul, D., Campbell, W. C. and Hudson, E. R. High fidelity manipulation of a qubit enabled by a manufactured nucleus. *NPJ Quantum Inf* **6**, 35 (2020)

CHAPTER 1

Introduction

The introduction of Shor's factoring algorithm [Sho94] more than 25 years ago demonstrated the first quantum computation of practical and economic importance to the world. Shor showed that using a quantum computer, integer factorization could be performed efficiently, i.e., that the factorization time scaled at most as a polynomial with number size. This is almost exponentially faster than best known classical factoring algorithm [BLP93], and means that if a quantum computer could be realized, Shor's algorithm could be used to break the widely used RSA encryption scheme.

While the work of Shor and others [Gro96, MMK95, CZ95] provided a great deal of interest in the field, it was DiVencenzo who first described the necessary requirements for a quantum computer. These have famously become known as DiVincenzo's criteria [DP97], and are given by:

- Well characterized qubits with a Hilbert-space that grows exponentially in system size.
- Initialization of the quantum system into a fiducial starting state.
- A system well isolated from the environment with coherence times much longer than the required quantum computation time.
- A universal set of quantum gates.
- The ability to faithfully readout the quantum state.

In addition to this list, and perhaps assumed, the ability to implement fault-tolerant quantum computation will allow a quantum computer to perform an arbitrarily long computation

reliably [Pre97].

Following these criteria, there is a natural question to ask: What physical 2-level quantum system should we use as our quantum bit? The answer of course is not straight forward, and qubits have been demonstrated across a variety of platforms, including but not limited to: quantum dots, Josephson junctions, optical cavity modes, and neutral and charged atoms [NPT99, WMI98, LD98, CY95, GKP01]. A detailed excursion into the variety of architectures, along with their pros and cons will be left to the reader. Instead, we focus on the the field of trapped-ion quantum computing, the focus of this thesis.

The choice of atomic species as qubit host relies on the availability of long-lived electronic states to use a qubit levels, as well as relatively simple electronic structure enabling Doppler cooling, state manipulation, state preparation, and state readout. Alkaline-earth metals, coulmn IIB transition metals, and Yb of the Lanthanides are ideal choices offering hydrogen-like structure when singly ionized.

Generally, trapped-ion qubits fall into three categories, with qubit frequencies ($\Delta\nu_q$) spanning many orders of magnitude: (1) Zeemen qubits, two state separated by the Zeeman interaction, typical in nuclear spin (I) zero specicies ($\Delta\nu_q \approx$ MHz), (2) hyperfine qubits, defined on two hyperfine levels when $I \neq 0$ ($\Delta\nu_q \approx$ GHz), and (3) optical qubits, defined on a ground state and long-lived metastable state separated by optical frequencies ($\Delta\nu_q \approx$ THz). Each type of qubit and its respective atomic host confer a different set of advantages. These are most easily demonstrated in Table 1.1, where the best reported gate and state preparation and measurement (SPAM) fidelities are given along with their qubit host[1].

[1]Fidelities reported in Table 1.1 are highest amongst all qubit platforms.

Operation	Method	Fidelity	Atomic Species	(I)	Cooling Wavelength	Reference
Single-Qubit Gate						
	Microwave	0.999999	$^{43}Ca^{+}$	7/2	397 nm	[HAB14]
	Raman	0.99996	$^{9}Be^{+}$	3/2	313 nm	[GTL16]
	Optical	0.99995	$^{40}Ca^{+}$	0	397 nm	[BXN17]
	Raman	0.99993	$^{43}Ca^{+}$	7/2	397 nm	[BHL16]
Two-Qubit Gate						
	Raman	0.9991(6)	$^{9}Be^{+}$	3/2	313 nm	[GTL16]
	Raman	0.999	$^{43}Ca^{+}$	7/2	397 nm	[BHL16]
	Light-shift	0.9974	$^{171}Yb^{+}$	1/2	369 nm	[BBF20]
	Optical	0.996	$^{40}Ca^{+}$	0	397 nm	[EWP19]
SPAM						
	Electron shelving	0.99971(3)	$^{133}Ba^{+}$	1/2	493 nm	This work
	Hyperfine-selective	0.99931(6)	$^{171}Yb^{+}$	1/2	369 nm	[CCV19]
	Electron shelving	0.99932(5)	$^{43}Ca^{+}$	7/2	397 nm	[HAB14]
	Optical	0.9989	$^{88}Sr^{+}$	0	422 nm	[KCA11]

Table 1.1: Highest reported fidelities for fundamental qubit operations. Cooling wavelengths do not include frequencies required to repump low lying D states in Ca^{+}, Sr^{+}, Ba^{+}, and Yb^{+} of 866 nm, 1092 nm, 650 nm, and 935 nm respectively.

There are two important points to highlight from Table 1.1: (1) no single atomic species dominates the qubit gate and SPAM fidelities, (2) implementing fault-tolerant error correction is still too resource intensive given the current state-of-the-art [FMM12]. With no single species presenting an obvious advantage, and fault-tolerant implementation currently inaccessible, it was conceivable to start looking for new qubit hosts outside of the "established" available atomic species.

While $^{133}Ba^{+}$ had been previously considered by the trapped-ion community [Die09], the 10.5 yr half-life seems to have discouraged its previous implementation as qubit hosts. However, while a graduate student at the University of Maryland, David Hucul recognized that $^{133}Ba^{+}$ combined many of the best features of various qubits in one species, and began advocating for its use. These include a spin-1/2 nucleus, visible wavelength electronic transitions required for Doppler cooling and qubit manipulations, and the longest D-state lifetimes of any alkali-earth or alkali-earth like element. The spin-1/2 nucleus allows fast, high-fidelity state initialization requiring only frequency control [OYM07], and a ground state hyperfine qubit defined on a pair of "clock" states, well protected from magnetic field noise [Fis97, WUZ17]. The visible wavelength electronic transitions allow the use of photonic technologies for manipulating and directing electromagnetic radiation, unavailable in the ultraviolet (UV). The long $^{2}D_{5/2}$ lifetime ($\tau \approx 30$ s) with its additional clock-states allow for high-fidelity electron shelving detection, as well as additional hyperfine and optical qubits separated by ≈ 83 MHz and $\approx$ 170.128 THz respectively.

What was needed, and has now been demonstrated or measured in this work, was a technique for efficient trap loading from a microgram source requiring minimal radiation safety overhead, and unknown state energies required for high-fidelity qubit operations. With the nearly ideal electronic structure and available photonic technologies in the visible, straight forward trapping and laser cooling of a single $^{133}Ba^{+}$ ion has also been demonstrated, followed by the first characterization of high-fidelity qubit operations. Using a composite pulse sequence for high-fidelity state transfer, as well as optically pumped electron shelving state detection, we measure an average single-shot SPAM fidelity of $\mathcal{F} = 0.9997(3)$, the lowest

reported to date on any qubit platform.

In the near term, an increased effort is underway to find a quantum computation that can outperform a classical computer without the need for fault-tolerant error correction, termed the noisy intermediate-scale quantum (NISQ) era. Under these conditions, single-shot SPAM infidelity (ϵ_s) causes a reduction in computational fidelity that is exponential in qubit number, $\mathcal{F}_s = (1 - \epsilon_s)^{N_q}$ (uncorrelated errors). While state readout error correction techniques can effectively lower measurement infidelity, they generally require a number of measurements that grows exponentially with N_q and single-shot readout infidelity [SD12]. It is therefore important to develop new means to reduce ϵ_s and increase N_q. With current the limit on $^{133}Ba^+$ SPAM fidelity technical, this work provides both a near-term and long-term path for improved computational accuracy on noisy intermediate-scale quantum (NISQ) devices. In addition, work is already underway to benchmark single- and two-qubit gate operations, which will complete the characterization of its utility as a trapped-ion qubit.

Finally, and perhaps most satisfying, is the recent adoption of $^{133}Ba^+$ amongst four research groups in the US. We hope we have done the community justice in our attempt to demonstrate $^{133}Ba^+$ as a new trapped-ion qubit. We gave it our best effort, and I am certainly looking forward to what future experiments may bring.

CHAPTER 2

Ion Trapping

"*I knew I should have checked that showboating Globetrotter algebra.*" - Professor Hubert J. Farnsworth

Any qubit host needs to be well localized to allow for repeated interrogation during a quantum information process. While a given for solid-state devices, free atoms and molecules pose a unique challenge due to their size and potential interaction with other nearby free particles. Charged species offer an advantage since practically achievable voltages in the lab produce forces well above what's required for confinement.[1]

To help motivate a form for the confining potential, we can start with something fundamental and well known, the harmonic oscillator $V(x,y) = V_0(\frac{x^2+y^2}{r_0^2})$ (we use 2D for simplicity, but all the results that follow generalize to 3D). Unfortunately, this does not satisfy Laplace's equation $\nabla^2 V = 0$, but note that simply changing the sign in front of one of the terms will, $V(x,y) = V_0(\frac{x^2-y^2}{r_0^2})$. The factor inside the parenthesis is the equation for a hyperbola, so by constructing hyperbolic electrodes and applying $\pm V_0$ to the opposing pair in x and y, our potential now satisfies Laplace's equation at both the interior and boundaries of the confinement region. Figure 2.1 shows a contour plot of the potential for hyperbolic shaped electrodes.

While we have now satisfied Laplace's equation, we immediately see that the force is confining in one direction and anti-confining in the other. This is a direct result of Earnshaw's theorem [Ear42], which states that charged particles cannot be confined with static fields. However, by applying an appropriate combination of time-dependent and static voltages, we

[1] Traps with potential depths reaching $\approx 10^5$K are commonly achieved.

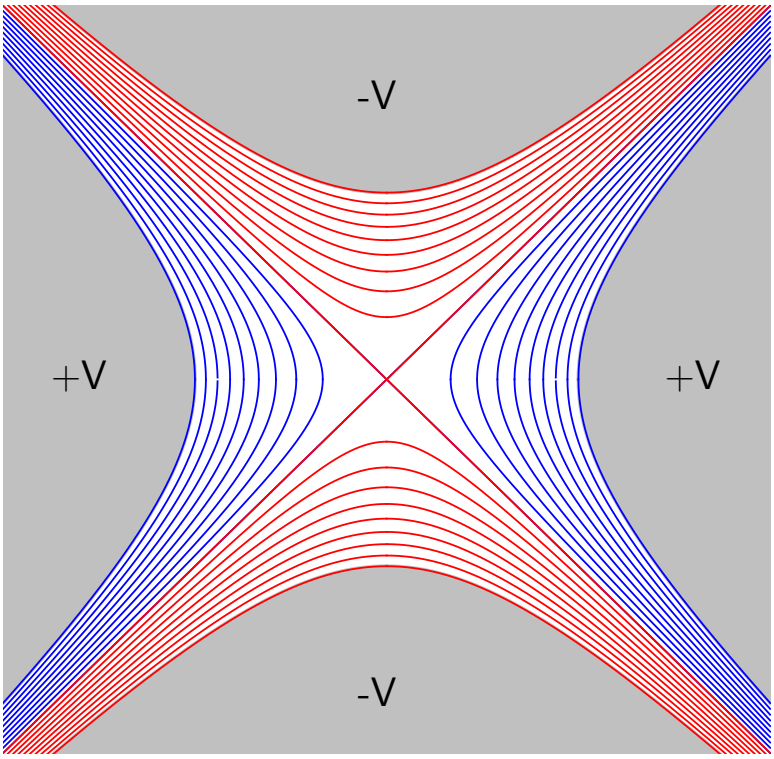

Figure 2.1: Contour plot of the potential for a 2D linear RF Paul trap. The inner electrode surfaces (grey) are hyperbolas with blue and red lines representing positive and negative potential contours.

can show confinement is possible. This is known as the RF Paul trap [POF58], and while many variations of the Paul trap exist, we focus here on the "four-rod" design used in this experiment (Fig. 2.2).

Before we begin, it will helpful to gain some intuition for how a time-dependent electric field can generate a time-averaged confining force, as well as further motivate our choice of a potential with quadratic terms. Consider a charged particle at the center of a parallel plate capacitor where the voltage difference applied to the plates oscillates sinusoidally in time. At $t = 0$, the particle is at rest and the field begins to turn on with the force directed in the positive direction (1D example). For the first half of the period, the particle's velocity increases, displacing it in the positive direction. Over the second half of the period, the velocity decreases to zero and the particle is again displaced in the positive direction by the same amount as in the first half of the period. As the cycle repeats the particle continually drifts in the positive direction. This is a direct result of the uniform electric field generated

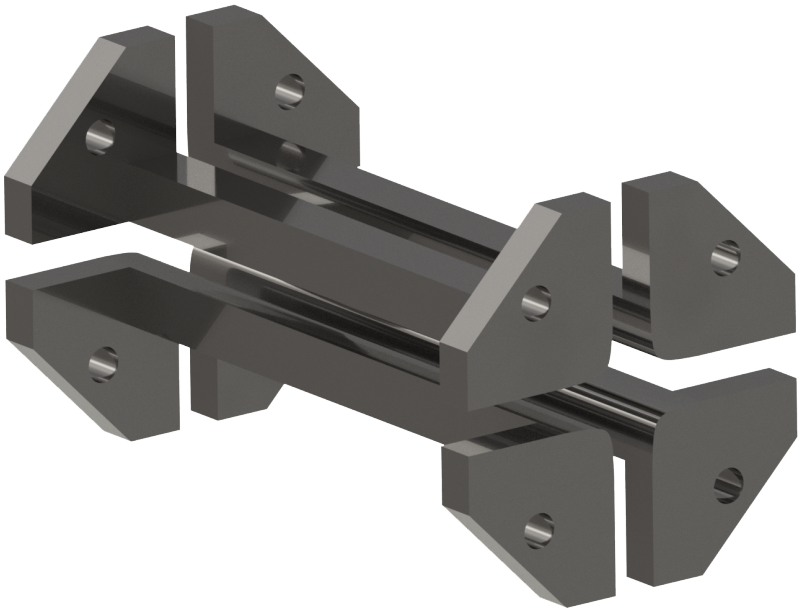

Figure 2.2: RF Paul trap used in the $^{133}Ba^{+}$ experiment. To reduce the contribution from non-harmonic terms in the trapping potential, the inner surfaces of the trap were cut using a wire EDM to better represent a hyperbolic surface. Closest distance from trap center to rod is $r_0 = 3$ mm.

by the parallel plate capacitor. To obtain a time-averaged net force, a non-uniform electric field is required. Using the same example, lets imagine we've bent the plates of the capacitor to create a quadratic potential near the center. Over the first half of the period, the particle increases velocity and is displaced in the positive direction. However, during the second half of the period, the particle sees a larger force in the negative direction since the field is larger the farther the particle is from the center. For the correct field amplitude and frequency, a particular charge to mass ratio will see a net time-averaged restoring force, exhibiting stable motion with components at the drive frequency of the parallel plate capacitor, and a slower, larger amplitude "secular" frequency.

2.1 Pseudopotential Approximation

With our confining potential properly motivated we begin by considering the "pseudopotential" approximation, first demonstrated by Kapitsa [Kap51], referencing [Kin99] for the

derivation. The force a charged particle experiences in our time-depenent potential (neglecting DC for now) can be written as:

$$\vec{F} = e\vec{E} = -e\nabla\frac{(x^2 - y^2)}{r_0^2}V_0\cos(\omega_{\mathrm{rf}}t) \tag{2.1}$$

with the equations of motion given by:

$$\ddot{x} = -\frac{2eV_0\cos(\omega_{\mathrm{rf}}t)}{mr_0^2}x \tag{2.2}$$

$$\ddot{y} = \frac{2eV_0\cos(\omega_{\mathrm{rf}}t)}{mr_0^2}y. \tag{2.3}$$

Considering only the x-motion, we will make the assumption that the particle experiences a large amplitude "low" frequency secular motion (x_s), and a small amplitude "high" frequency oscillation called micromotion (x_{mm}). We rewrite the equation of motion as:

$$\ddot{x}_s + \ddot{x}_{\mathrm{mm}} = -\frac{2eV_0\cos(\omega_{\mathrm{rf}}t)}{mr_0^2}(x_s + x_{mm}). \tag{2.4}$$

Given our initial assumptions, we have $\ddot{x}_{\mathrm{s}} << \ddot{x}_{\mathrm{mm}}$ and $x_{\mathrm{mm}} << x_{\mathrm{s}}$, leading to the equation:

$$\ddot{x}_{\mathrm{mm}} \approx -\frac{2eV_0\cos(\omega_{\mathrm{rf}}t)}{mr_0^2}x_s. \tag{2.5}$$

We assume x_{s} is approximately constant over the relevant timescales of x_{mm}, allowing us to only consider the cosine function in the integration:

$$x_{\mathrm{mm}} \approx \frac{2eV_0\cos(\omega_{\mathrm{rf}}t)}{mr_0^2\omega_{\mathrm{rf}}^2}x_{\mathrm{s}}. \tag{2.6}$$

This is the approximate equation for the micromotion, where the amplitude is dependent on the position from the center of the trap. We can now plug Equations 2.5 and 2.6 back in to 2.4 to determine the secular motion:

$$\ddot{x}_{\mathrm{s}} = -\frac{2eV_0\cos(\omega_{\mathrm{rf}}t)}{mr_0^2}\left(\frac{2eV_0\cos(\omega_{\mathrm{rf}}t)}{mr_0^2\omega_{\mathrm{rf}}^2}x_{\mathrm{s}}\right). \tag{2.7}$$

Time averaging over one RF period eliminates the cosine squared term leaving:

$$\ddot{x}_{\mathrm{s}} = -\frac{2e^2V_0^2}{m^2r_0^4\omega_{\mathrm{rf}}^2}x_{\mathrm{s}} \tag{2.8}$$

which has the well-known form of a harmonic oscillator with secular frequency $\omega_{\text{sec}} = \frac{\sqrt{2}eV_0}{mr_0^2\omega_{\text{rf}}}$. Combining our two solutions for the total motion:

$$x \propto \cos(\omega_s t)\left[1 + \frac{2eV_0\cos(\omega_{\text{rf}}t)}{mr_0^2\omega_{\text{rf}}^2}\right] \tag{2.9}$$

which is plotted in Figure 2.9.

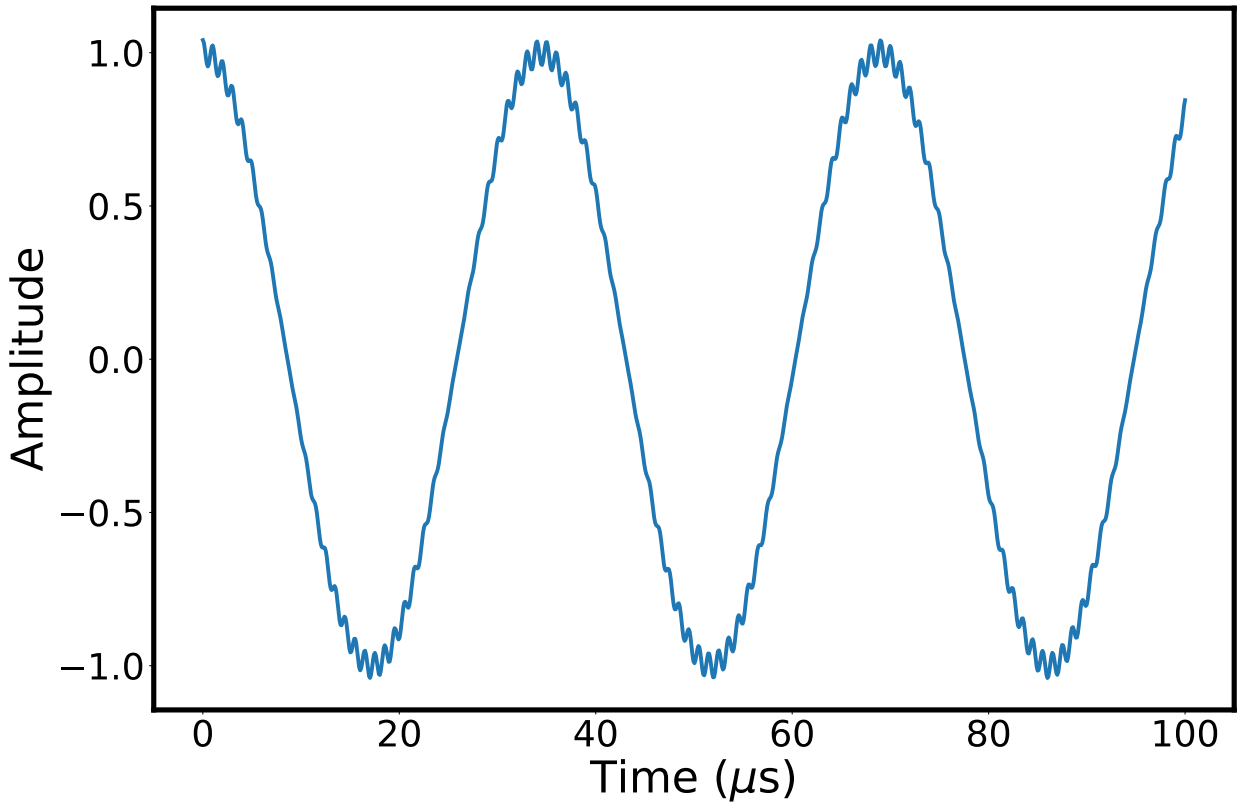

Figure 2.3: Plot of the ion motion using Equation 2.9 derived using the pseudopotential approximation. Parameters used are from the current experiment with $\omega_{\text{rf}} \approx 2\pi \times 1$ MHz, $r_0 = 3$ mm, $m = 133$ amu. In practice, the voltage used in the experiment is $V_0 \approx 200$ V, however in this figure $V_0 = 20$ V to remain well within the approximation that the micromotion amplitude is much less than the secular motion amplitude.

2.2 Mathieu Solutions

We can now turn to a more rigorous derivation for the equations of motion, again considering electrodes with hyperbolic surfaces. While the theory is often derived by assuming

$+V_0\cos(\omega_{\rm rf}t)$ is applied to one pair of electrodes and $-V_0\cos(\omega_{\rm rf}t)$ to another, in practice it is much simpler to keep one pair of opposing electrodes at ground (DC rods) and apply RF to the other pair (RF rods). In addition, we include the possibility of additional DC voltages applied to the RF rods (U_0). Finally, while the RF will provide some confinement in the axial direction, we include an additional DC voltage applied to endcaps ($U_{\rm EC}$) to further constrain the motion axially. The general potential can be written as:

$$V(x,y,z,t) = \left(\frac{V_0 cos(\omega_r f t) + U_0}{2}\right)\left(1 + \frac{x^2 - y^2}{r_0^2}\right) + U_{\rm EC}\left(\frac{2z^2 - x^2 - y^2}{z_0^2}\right) \tag{2.10}$$

with z_0 the characteristic length in the axial direction. The equations of motion become:

$$\ddot{x} = \left(\frac{2eU_{\rm EC}}{mz_0^2} - \frac{V_0\cos(\omega_{\rm rf}t) + U_0}{mr_0^2}\right)x \tag{2.11}$$

$$\ddot{y} = \left(\frac{2eU_{\rm EC}}{mz_0^2} + \frac{V_0\cos(\omega_{\rm rf}t) + U_0}{mr_0^2}\right)y \tag{2.12}$$

$$\ddot{z} = \frac{-4eU_{\rm EC}}{mz_0^2}z. \tag{2.13}$$

For z we get the equation for a harmonic oscillator with secular frequency $\omega_z = 2\sqrt{eU_{\rm EC}/mz_0^2}$. For x and y, we can use the substitution $\xi = \frac{\omega_{\rm rf}t}{2}$ to cast each into the form of the Mathieu equations [Duh92].

$$\frac{d^2x}{d\xi^2} + [a_x + 2q_x\cos(2\xi)]x = 0 \tag{2.14}$$

$$\frac{d^2y}{d\xi^2} + [a_y + 2q_y\cos(2\xi)]y = 0 \tag{2.15}$$

with

$$a_x = \frac{4eU_0}{m\omega_{\rm rf}^2 r_0^2} - \frac{8eU_{\rm EC}}{m\omega_{\rm rf}^2 z_0^2} \tag{2.16}$$

$$a_y = -\left(\frac{4eU_0}{m\omega_{\rm rf}^2 r_0^2} + \frac{8eU_{\rm EC}}{m\omega_{\rm rf}^2 z_0^2}\right) \tag{2.17}$$

$$q_x = \frac{2eV_0}{m\omega_{\rm rf}^2 r_0^2} = -q_y. \tag{2.18}$$

The solutions to the Mathieu equations have been well studied in the context of ion trapping, and a general form of the solution is given by Floquet's theorem:

$$r_i(\xi) = A_i e^{iu_i\xi} \sum_{-\infty}^{\infty} C_{2n,i} e^{i2n\xi} + B_i e^{-iu_i\xi} \sum_{-\infty}^{\infty} C_{2n,i} e^{-i2n\xi} \tag{2.19}$$

where u_i ($i \in \{x, y\}$) and the coefficients $C_{2n,i}$ depend only on a_i and q_i, and the constants A_i and B_i depend on initial conditions. Using Euler's formula we re-express the exponentials to get:

$$r_i(\xi) = A_i' \sum_{-\infty}^{\infty} C_{2n,i} \cos([2n + u_i]\xi) + iB_i' \sum_{-\infty}^{\infty} C_{2n,i} \sin([2n + u_i]\xi). \tag{2.20}$$

We now plug this back into Equation 2.14 to get:

$$\begin{aligned} A_i' \sum_{-\infty}^{\infty} C_{2n,i}(2n + u_i)^2 \cos([2n + u_i]\xi) + iB_i' \sum_{-\infty}^{\infty} C_{2n,i}(2n + u_i)^2 \sin([2n + u_i]\xi) = \\ A_i' \sum_{-\infty}^{\infty} C_{2n,i}(a_i + 2q_i \cos(2\xi)) \cos([2n + u_i]\xi) + \\ iB_i' \sum_{-\infty}^{\infty} C_{2n,i}(a_i + 2q_i \cos(2\xi)) \sin([2n + u_i]\xi). \end{aligned} \tag{2.21}$$

Looking at the cosine terms we have:

$$- A_i' \sum_{-\infty}^{\infty} C_{2n,i}(2n + u_i)^2 \cos([2n + u_i]\xi) + \tag{2.22}$$

$$A_i' \sum_{-\infty}^{\infty} C_{2n,i}(a_i + 2q_i \cos(2\xi)) \cos([2n + u_i]\xi) = 0.$$

Invoking the product to sum trigonometric identity in the second term and rearranging we have:

$$\begin{aligned} A_i' \sum_{-\infty}^{\infty} C_{2n,i}(a_i - (2n + u_i)^2) \cos([2n + u_i]\xi) + \\ A_i' \sum_{-\infty}^{\infty} q_i C_{2n,i} \cos([2n + 2 + u_i]\xi) + \\ A_i' \sum_{-\infty}^{\infty} q_i C_{2n,i} \cos([2n - 2 + u_i]\xi) = 0 \end{aligned} \tag{2.23}$$

which we can finally write as:

$$A_i' \sum_{-\infty}^{\infty} C_{2n,i}(a_i - (2n+u_i)^2)\cos([2n+u_i]\xi) + A_i' \sum_{-\infty}^{\infty} q_i C_{2n+2,i}\cos([2n+u_i]\xi) + A_i' \sum_{-\infty}^{\infty} q_i C_{2n-2,i}\cos([2n+u_i]\xi) = 0 \tag{2.24}$$

giving us the following recursion relationship:

$$C_{2n+2,i} + D_{2n,i}C_{2n,i} + C_{2n-2,i} = 0 \tag{2.25}$$

with

$$D_{2n,i} = \frac{a_i - (2n+u_i)^2}{q_i}. \tag{2.26}$$

The set of equations for all coefficients can be constructed into an infinite matrix:

$$\begin{pmatrix} 1 & D_{-2n,i} & 1 & & & & & & \\ & \ddots & & \ddots & & & & & \\ & & 1 & D_{-2,i} & 1 & & & & \\ & & & 1 & D_{0,i} & 1 & & & \\ & & & & 1 & D_{2,i} & 1 & & \\ & & & & & \ddots & & \ddots & \\ & & & & & & 1 & D_{2n,i} & 1 \end{pmatrix} \begin{pmatrix} C_{-2n+2,i} \\ \vdots \\ C_{-2,i} \\ C_{0,i} \\ C_{0,i} \\ \vdots \\ C_{2n+2,i} \end{pmatrix}. \tag{2.27}$$

A non-trivial solution for u_i requires the determinant be zero, from which values of a_i and q_i can be found such that the solution to Equation 2.14 is bounded [Gho95] (stable motion). This requires $u_i \equiv \alpha_i + i\beta_i$ to be purely imaginary ($\alpha_i = 0$). Figure 2.4 shows the lowest stability region with $0 \leq \beta \leq 1$, and the central region of overlap is where a and q are stable in both dimensions. Appendix B includes Python code [pyt] to generate the stability region in two and three dimensions following the work of [Jon08]. To determine the relationship between β_i, a_i and q_i, we first look at the case where $n = 0$:

$$\beta_i^2 = a_i + q_i\left(\frac{C_{2,i} + C_{-2,i}}{C_0}\right). \tag{2.28}$$

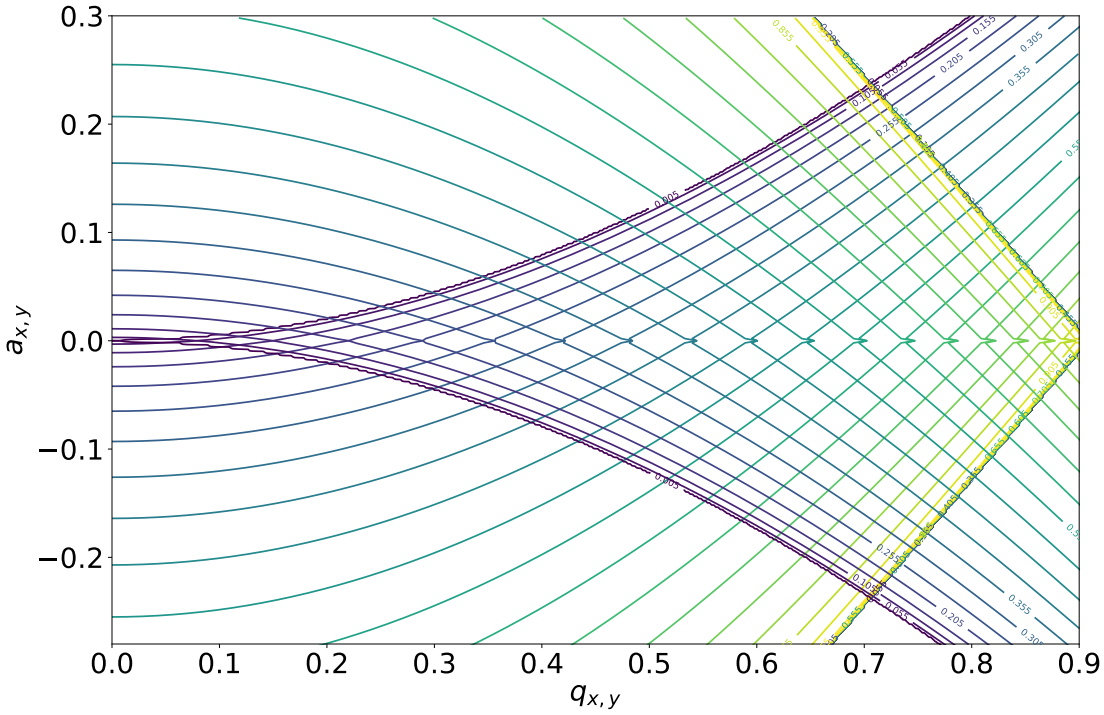

Figure 2.4: Stability diagram for 2D Paul trap.

In addition, algebraic manipulation of equation 2.25 yields the following two expressions (dropping the subscript i for now):

$$\frac{C_{2n}}{C_{2n+2}} = \frac{-1}{D_{2n} + \frac{C_{2n-2}}{C_{2n}}} \tag{2.29}$$

$$\frac{C_{2n}}{C_{2n-2}} = \frac{-1}{D_{2n} + \frac{C_{2n+2}}{C_{2n}}}. \tag{2.30}$$

These equations can be combined to generate a recursion relation for calculating β to any order in a and q. Under the assumption that $|a_i|, q_i^2 \ll 1$ and $C_{\pm 4} = 0$, the lowest order solution for β is:

$$\beta_i \approx \sqrt{a_i + \frac{q_i}{2}}. \tag{2.31}$$

If $A_x = B_x$ and we assume $a_x = 0$, then our lowest order solution becomes:

$$x(t) = 2AC_0 cos\left(\beta_x \frac{\omega_{rf} t}{2}\right)\left[1 - q_x cos(\omega_{rf} t)\right]. \tag{2.32}$$

This is the same solution we found using the pseudopotential approximation (Eq. 2.9).

2.3 Excess Micromotion

In the previously derived solution, we assumed that the only fields present were those that were intentionally applied. In practice, stray electric fields are present for a variety of reasons and often result from charging of nearby insulators during ion production.

Considering only the x-direction, the equation of motion in the presence of a uniform stray electric field becomes:

$$\ddot{x} - \left(\frac{2eU_{\mathrm{EC}}}{mz_0^2} - \frac{V_0 \cos(\omega_{\mathrm{rf}} t) + U_0}{mr_0^2} \right) x = \frac{eE_x}{m}. \tag{2.33}$$

The lowest order solution to the equation is given by [WMI98]:

$$x(t) = \left(\frac{eE_x}{m\omega_s^2} + A \cos\left(\beta_x \frac{\omega_{\mathrm{rf}} t}{2} \right) \right) \left[1 - q_x \cos(\omega_{\mathrm{rf}} t) \right]. \tag{2.34}$$

The term $\frac{eE_x}{m\omega_s^2}$ produces a constant offset to the ion's equilibrium position as well as an additional component of motion at the RF drive frequency, often referred to as "excess micromotion."[2] This causes phase modulation of any electromagnetic radiation applied to the ion and can reduce the scattering rate of the intended transition. For a recent demonstration of this in $^{40}Ca^{+}$ see Ref. [Pru14]. In addition, excess micromotion can lead to steady state temperatures orders of magnitude above the Doppler limit [BMB98]. Various techniques are used to reduced excess micromotion including photon correlation measurements, measuring carrier depletion due to phase modulation, and modulation of the pseudopotential at frequency $\Omega < \omega_{\mathrm{rf}}$ [BMB98, NDM11]. In this experiment, both the photon correlation measurement as well as measured modulation depth were attempted, but the slow duty cycle due to hardware limitations made their use impractical. Instead, a more coarse method was used where the ion's position was monitored on a camera as the pseudopotential was raised and lowered [Tam96]. DC compensation voltages are adjusted until no more displacement is detectable after raising or lowering the trap depth (V_{rf}).

[2] A phase mismatch between RF rods can also cause excess micromotion.

2.4 Mass Filtering

The general technique for loading ions in this experiment uses a Nd:YAG pulsed laser ($t_{pulse} \approx$ 5 ns) doubled to 532 nm incident on a $BaCl_2$ target, and is described in more detail in Chapter 5. The method directly produces ions and we observe all naturally occurring Ba^+ isotopes, as well as $BaCl^+$ in the ion trap after ablating. The formation of $BaOH^+$ is also observed after loading Ba^+, with the rate dependent on the partial pressure of H_2O. Typical trapped-ion quantum information experiments use only a single isotope of the chosen species, and other co-trapped charged species can cause unwanted effects such as heating or unwanted site hopping.

We use a combination of mass filtering [Pau90] and laser heating to isolate a barium isotope of particular interest. For a 2D Paul, trap mass filtering is accomplished by choosing the a and q parameter such that only a particular charge to mass ratio has a stable trajectory. Since the ratio of $a/q = 2U_0/V_0$ and does not depend on the mass, for fixed r_0, ω_{rf}, U_0, and V_0 all masses fall on a straight line ("operating line") in a-q stability plane. As shown in Figure 2.5, the top corner of the stability diagram can be used to make only a single e/m stable. The stability diagram shown in figure 2.5 assumes infinitely long electrodes with inner surfaces shaped as hyperbolas. Radial optical access requires modification of the surface and adds non-harmonic terms to the trapping potential. Experimentally we are not able to isolate a single barium isotope by adjusting the a and q parameters of our trap (Fig. 2.2). However, we are able successfully filter $BaOH^+$ and $BaCl^+$ while retaining Ba^+ (some loss of Ba^+ is observed when filtering $BaOH^+$). Unwanted barium isotopes can be removed via Doppler heating described in more detail in Chapter 4.

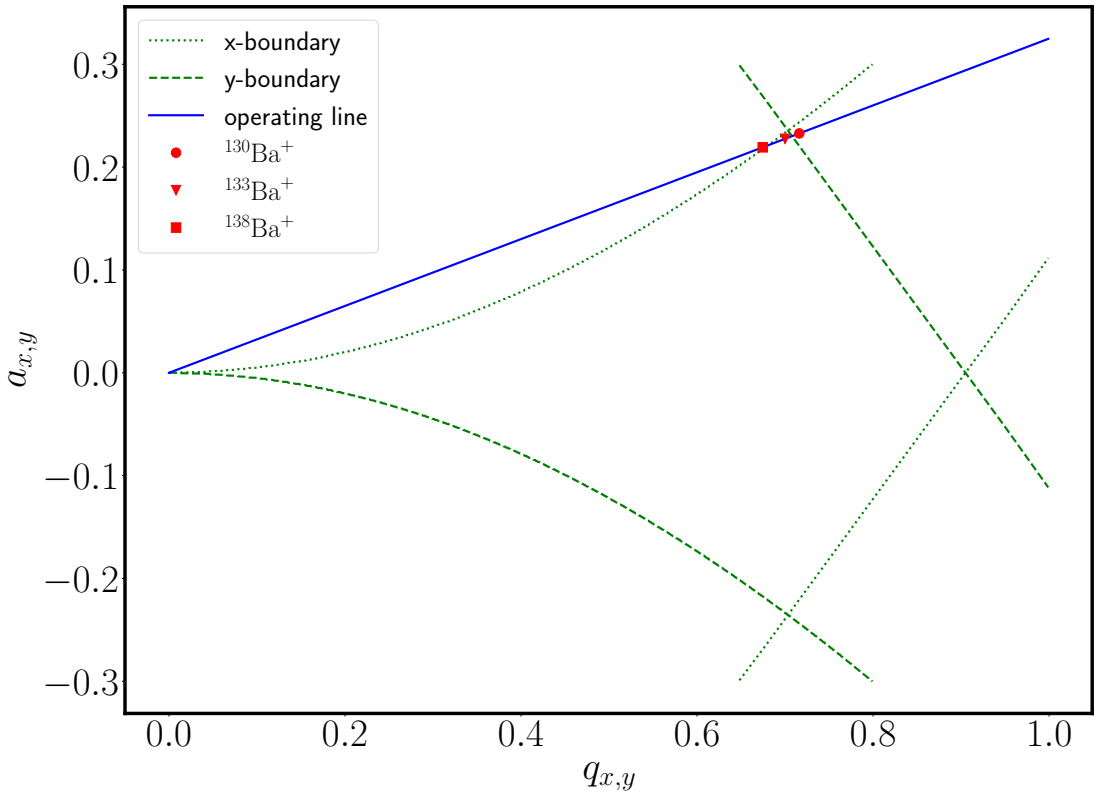

Figure 2.5: Boundary of the 2D stability region in the a_i and q_i plane assuming infinitely long rods. Dotted lines are the x-stability boundaries, dashed lines are the y-stability boundaries. Fourth order polynomial fits give $X = -0.0001 - 0.0007x + 0.5x^2 - 0.01x^3 - 0.036x^4$ for the upper line of the x boundary, and $X = -0.981 + 0.961x + 0.159x^2 - 0.0291x^3 + 0.00248x^4$ for the lower line in x boundary. Equations for y-boundaries are reflected about the q-axis. All masses fall on a straight line ("operating line") in the a_i-q_i plane with slope given by $m = 2U_0/V_0$. Mass filtering can be achieved by adjusting the operating line such that only a single charge to mass ratio has a stable trajectory.

CHAPTER 3

Atom-Laser Interactions

"Ahhh... sweet photons. I don't know if you're waves or particles, but you go down smooth."
-Bender Bending Rodriguez

3.1 Two-Level Dynamics

Fundamentally, a qubit can be defined on any two-level quantum system. Operation of a quantum computer will require a universal gate set which includes both single- and two-qubit gates. Many of the two qubit entangling gates, most notably the CNOT, require single qubit gates on each of the pair of qubits to be entangled. Because of the importance of single qubit rotations, the time evolution due to an applied electromagnetic field is derived in detail.

We begin with the Hamiltonian of our system which contains two contributions:

$$\mathcal{H} = \mathcal{H}_0 + \mathcal{H}'. \tag{3.1}$$

$\mathcal{H}_0$ is the free atomic Hamiltonian, and $\mathcal{H}'$ is due to an applied electromagnetic field with frequency ω_{L} and phase ϕ, e.g[1]:

$$E = E_0 e^{i(\vec{k}\cdot\vec{r}-\omega_L t+\phi)}. \tag{3.2}$$

If the average spatial extent of the electron $\langle r \rangle$ is much less than the wavelength of incident radiation, the spatial term can be approximated as $e^{i\vec{k}\cdot\vec{r}} \approx 1$. This is known as the dipole

[1]Here we assume an electric field is coupling our two qubit states, but a magnetic field of the same form could also have been used representing a magnetic dipole transition.

approximation. We can now write our Hamiltonian in matrix form ($\hbar = 1$):

$$\mathcal{H} = \begin{pmatrix} 0 & \frac{\Omega}{2}e^{-i(\omega_L t+\phi)} \\ \frac{\Omega^*}{2}e^{i(\omega_L t+\phi)} & \omega_0 \end{pmatrix} \tag{3.3}$$

where Ω is the Rabi frequency:

$$\Omega \equiv eE_0X_{12} \tag{3.4}$$

with $X_{12} \equiv \langle 1|r|2\rangle$ the matrix element between states 1 and 2.

The general state of our two-level system is given as:

$$|\psi\rangle = C_0(t)|0\rangle + C_1(t)e^{i\omega_0 t}|1\rangle \tag{3.5}$$

where we have explicitly written the time dependence to separate that due to the free atomic energy $e^{i\omega_0 t}$, and that due to the perturbation, $C(t)$. Ultimately, our goal is to determine the functional dependence of the coefficients C_0 and C_1 on time, since the square of these determine the atomic populations. The time evolution of a quantum state is given by applying the time evolution operator, and when the Hamiltonian has no explicit time dependence, it is given as:

$$\mathcal{U}(t) = e^{-i\mathcal{H}t}. \tag{3.6}$$

To eliminate the time dependence from the Hamiltonian, we make the following unitary transformation:

$$U = \begin{pmatrix} 1 & 0 \\ 0 & e^{-i\omega_L t} \end{pmatrix}. \tag{3.7}$$

Our transformed Hamiltonian becomes:

$$\mathcal{H} = U^\dagger \mathcal{H} U. \tag{3.8}$$

This unitary transformation modifies the time-dependent Schrodinger equation giving the effective Hamiltonian [BKD10]:

$$\widetilde{\mathcal{H}} = U^\dagger \mathcal{H} U - iU^\dagger \frac{\partial U}{\partial t} \tag{3.9}$$

which for our Hamiltonian and transformation give:

$$\widetilde{\mathcal{H}} = \begin{pmatrix} 0 & \frac{\Omega}{2}e^{-i\phi} \\ \frac{\Omega^*}{2}e^{i\phi} & \Delta \end{pmatrix} \tag{3.10}$$

with $\Delta = \omega_0 - \omega_L$. Our general quantum state becomes:

$$U|\psi\rangle = C_0(t)|0\rangle + C_1(t)e^{i\Delta t}|1\rangle\,. \tag{3.11}$$

This is equivalent to moving into a frame rotating at the laser frequency ω_L. With the explicit time dependence now eliminated from the Hamiltonian, we can simply exponentiate $\mathcal{H}$ to get the time evolution operator. In order to determine the matrix form, we first rewrite our effective Hamiltonian in terms of the Pauli spin operators:

$$\mathcal{H} = \frac{\Delta}{2}(\mathbb{1} - \sigma_z) + \frac{\Omega}{2}[\cos(\phi)\sigma_x + \sin(\phi)\sigma_y] \tag{3.12}$$

which we can rewrite as:

$$\mathcal{H} = \frac{\Delta}{2}\mathbb{1} + \vec{\sigma}\cdot\vec{a} \tag{3.13}$$

with $\vec{a}$ given as:

$$\vec{a} = \frac{\Omega}{2}\cos(\phi)\hat{x} + \frac{\Omega}{2}\sin(\phi)\hat{y} - \frac{\Delta}{2}\hat{z}. \tag{3.14}$$

Our time evolution operator becomes:

$$\mathcal{U}(t) = e^{-i\mathbb{1}\frac{\Delta}{2}t}e^{-i(\vec{\sigma}\cdot\vec{a})t}. \tag{3.15}$$

The first factor can simply be rewritten as:

$$\mathbb{1}e^{-i\frac{\Delta}{2}t}. \tag{3.16}$$

For the second factor, we will use the identity:

$$(\vec{\sigma}\cdot\vec{a})^2 = |\vec{a}|^2 = \frac{\Omega^2 + \Delta^2}{4} \equiv \frac{\Omega_g^2}{4} \tag{3.17}$$

where we define Ω_g as the generalized Rabi frequency. We then Taylor expand the complex exponential:

$$e^{-i(\vec{\sigma}\cdot\vec{a})t} = \Big[1 - \frac{(\vec{\sigma}\cdot\vec{a})^2}{2!}t^2 + \frac{(\vec{\sigma}\cdot\vec{a})^4}{4!}t^4 + ...\Big] - i\Big[\frac{(\vec{\sigma}\cdot\vec{a})}{1!}t + \frac{(\vec{\sigma}\cdot\vec{a})^3}{3!}t^3 + ...\Big]. \tag{3.18}$$

Using the identity above we can rewrite each term as:

$$e^{-i(\vec{\sigma}\cdot\vec{a})t} = \Big[1 - \frac{(at)^2}{2!} + \frac{(at)^4}{4!} + ...\Big] - i\frac{(\vec{\sigma}\cdot\vec{a})}{a}\Big[\frac{(at)}{1!} + \frac{(at)^3}{3!} + ...\Big]. \tag{3.19}$$

The terms in the square brackets are just the Taylor expansions for sine and cosine:

$$e^{-i(\vec{\sigma}\cdot\vec{a})t} = \mathbb{1}\cos\left(\frac{\Omega_g t}{2}\right) + -i\frac{(\vec{\sigma}\cdot\vec{a})}{a}\sin\left(\frac{\Omega_g t}{2}\right). \tag{3.20}$$

Converting to matrix form this becomes:

$$e^{i(\vec{\sigma}\cdot\vec{a})t} = \begin{pmatrix} \Big[\cos(\frac{\Omega_g t}{2}) + i\frac{\Delta}{\Omega_g}\sin(\frac{\Omega_g t}{2})\Big] & -i\frac{\Omega}{\Omega_g}e^{-i\phi}\sin(\frac{\Omega_g t}{2}) \\ -i\frac{\Omega}{\Omega_g}e^{i\phi}\sin(\frac{\Omega_g t}{2}) & \Big[\cos(\frac{\Omega_g t}{2}) - i\frac{\Delta}{\Omega_g}\sin(\frac{\Omega_g t}{2})\Big] \end{pmatrix} \tag{3.21}$$

so finally we have:

$$\mathcal{U}(t) = e^{-i\frac{\Delta}{2}t}\begin{pmatrix} \Big[\cos(\frac{\Omega_g t}{2}) + i\frac{\Delta}{\Omega_g}\sin(\frac{\Omega_g t}{2})\Big] & i\frac{\Omega}{\Omega_g}e^{-i\phi}\sin(\frac{\Omega_g t}{2}) \\ -i\frac{\Omega}{\Omega_g}e^{i\phi}\sin(\frac{\Omega_g t}{2}) & \Big[\cos(\frac{\Omega_g t}{2}) - i\frac{\Delta}{\Omega_g}\sin(\frac{\Omega_g t}{2})\Big] \end{pmatrix}. \tag{3.22}$$

Our original goal was to determine the time dependence of our coefficients:

$$\begin{pmatrix} C_0(t+t_0) \\ C_1(t+t_0) \end{pmatrix} = \begin{pmatrix} \Big[\cos(\frac{\Omega_g t}{2}) + i\frac{\Delta}{\Omega_g}\sin(\frac{\Omega_g t}{2})\Big] & i\frac{\Omega}{\Omega_g}e^{-i\phi}\sin(\frac{\Omega_g t}{2}) \\ -i\frac{\Omega}{\Omega_g}e^{i\phi}\sin(\frac{\Omega_g t}{2}) & \Big[\cos(\frac{\Omega_g t}{2}) - i\frac{\Delta}{\Omega_g}\sin(\frac{\Omega_g t}{2})\Big] \end{pmatrix} \begin{pmatrix} C_0(t_0) \\ C_1(t_0)e^{i\frac{\Delta t_0}{2}} \end{pmatrix} \tag{3.23}$$

which now allows us to calculate the time evolution of any arbitrary input state given the parameters of the perturbing field. The matrix $\mathcal{U}(t) = R(\Omega t, \phi)$ can also be viewed as a rotation on the Bloch sphere. The rotation is given by the angle $\theta = \Omega t$ around an axis in the x-y plane defined by $\cos\phi\hat{x} + \sin\phi\hat{y}$. To perform an arbitrary single qubit gate we must be able to rotate by any angle around any axis. Rotations around the x or y axis are obviously given by choosing the laser phase of $\phi = 0$ or $\phi = \pi/2$. For rotations around the z-axis, a composite sequence given by $R(\theta) = R(\pi/2, 0)R(\theta, \pi/2)R(-\pi/2, 0)$ can be used. This demonstrates that given control of the phase and duration of the applied radiation, any single qubit rotation can be achieved.

3.1.1 Two-Level System with Damping

In the previous discussion it was assumed that the excited state had an infinitely long lifetime. In real systems, coupling to the vacuum modes causes spontaneous emission (relaxation). Spontaneous emission is a necessary component of Doppler cooling and the emitted photons are an atomic physicists primary signal for detecting the atomic state. To include the effects of relaxation, a damping term can be added to the perturbation Hamiltonian:

$$\mathcal{H}' = \begin{pmatrix} 0 & \frac{\Omega}{2}e^{-i(\omega_L t+\phi)} \\ \frac{\Omega^*}{2}e^{i(\omega_L t+\phi)} & \omega_0 - i\Gamma/2 \end{pmatrix} \tag{3.24}$$

where Γ is the excited state linewidth. At this point, it is common to move to the density matrix formalism which naturally includes relaxation effects and allows for mixed states. The density matrix is defined as:

$$\rho \equiv |\psi\rangle \langle\psi| \tag{3.25}$$

where in matrix notation we have:

$$\rho = \begin{pmatrix} |C_0|^2 & C_0 C_1^* \\ C_1 C_0^* & |C_1|^2 \end{pmatrix} = \begin{pmatrix} \rho_{11} & \rho_{12} \\ \rho_{21} & \rho_{22} \end{pmatrix}. \tag{3.26}$$

The density matrix is an operator where the diagonal components represent the populations and the off-diagonal elements are the coherences. The time evolution of the density operator is given by the Liouville equation [BKD10]:

$$\frac{d\rho}{dt} = \frac{1}{i\hbar}[\mathcal{H}, \rho] - \frac{1}{2}\{\Gamma, \rho\} \tag{3.27}$$

where Γ in the anti-commutator is multiplied by the identity matrix. Solving for the steady-state excited state population as a function of detuning $\Delta = \omega_L - \omega_0$ and laser intensity [Foo12] allows us to calculate the rate of spontaneously emitted photons:

$$\mathcal{R} = 2\pi\Gamma\rho_{22} = 2\pi\Gamma\left(\frac{s/2}{1 + s + 4(\Delta/\Gamma)^2}\right) \tag{3.28}$$

with the excited state linewidth given in Hz. The saturation parameter s is a measure of the Rabi frequency compared to the spontaneous emission rate, and is defined as:

$$s = \frac{2\Omega^2}{\Gamma^2} = \frac{I}{I_{\text{sat}}}. \tag{3.29}$$

The saturation parameter I_{sat} is a property of the atomic system and allows one to define s in terms of the laser intensity. For a two level system on resonance it is given by:

$$I_{sat} = \frac{\pi}{3}\frac{hc\Gamma}{\lambda^3}. \tag{3.30}$$

For a system with more than two levels, the saturation intensity transforms to:

$$I_{sat} = \frac{\pi}{3}\frac{hc\Gamma^2}{\lambda^3\Gamma_{\text{p}}} \tag{3.31}$$

where now Γ is the total excited state linewidth and Γ_p is the partial linewidth of the two levels of interest. This can be calculated from equation 3.29 by re-expressing the Rabi frequency in terms of the partial linewidth and laser intensity.

3.2 Laser Cooling

Suggested in the 1970s [WD75, WS75] and first demonstrated by Chu in 1985 [CHB85], Doppler cooling has played a tremendous role in the progression of atomic physics. Removing Doppler shifts and localizing atoms for repeated interrogation has opened up an entirely new toolbox for accessing new quantum regimes and precision measurement experiments. In trapped-ion quantum information experiments, Doppler cooling results in the formation of Coulomb crystals allowing for repeated manipulation of multiple ions over the course of a quantum simulation or algorithm. In addition, the spontaneously emitted photons act as the primary source for detecting ions in the trap as well as reading out the quantum state.

For trapped-ions bound in a harmonic potential, incident radiation becomes phase modulated in the rest frame of the atom. There are generally two regimes of interest when considering cooling:

- $\omega_{sec} \ll \Gamma$: When the secular frequency is much less than the excited state linewidth, the time it takes to absorb and emit a photon is much less than one period of the secular motion. As the atom's velocity changes, the transition frequency is Doppler shifted into resonance and absorption and emission occurs effectively at an instant of

time. Phase modulation effects can be neglected since each scattering event resets the atomic phase. This is the same as Doppler cooling of a free atom.

- $\Gamma \ll \omega_{sec}$: In the opposite case when the time it takes to scatter a photon is much less than the period of motion, the atom undergoes many oscillations before a scattering event. In this case the electric field becomes phase modulated in the rest frame of the atom producing frequency modulated spectra (sidebands). When the laser frequency is tuned to one of the sidebands, kinetic energy can be removed (red sideband) or added (blue sideband).

It is often the case that multiple transitions are used in a given atomic species which allows access to both regimes. These limits also apply to the case of excess micromotion.

We next present a simple model for cooling in the case where the secular frequency is much less than the excited state linewidth, and refer the reader elsewhere for a discussion of the second regime and the technique of sideband cooling [NHT78, DBI89, MCB94]. We start with a one dimensional model for simplicity, and imagine two counter-propagating laser beams with the same frequency, detuned below the atomic resonance. We assume a simple two level system where the scattering rate now includes a term for the Doppler shift:

$$\mathcal{S}_{\pm} = \frac{\Gamma}{2}\left(\frac{s}{1+s+4(\frac{\Delta \pm kv}{\Gamma})^2}\right) \tag{3.32}$$

and the sign of the Doppler shift is opposite for the two beams. Absorption of a photon results in the atom receiving a momentum kick of $\hbar k$. For an atom moving in the positive direction, the counter-propagating beam is shifted into resonance and the atom absorbs and emits a photon. For the beam co-propagating with the atom, the laser is shifted away from resonance and absorption and emission are much less likely. In this way, the atom is preferentially absorbing photons that reduce its momentum. Spontaneous emission is isotropic, emitting photons equally in the positive and negative direction, adding zero momentum on average. In this way the atom can be cooled, and is naturally extended to three dimensions by adding counter-propagating beams in the other dimensions (optical molasses). To show this mathematically, we begin in 1D assuming low intensities ($s \ll 1$) where stimulated emission

can be ignored. The average force on an atom is given by the average number of photons absorbed in a given period of time:

$$F = \hbar k \mathcal{S} = \hbar k \frac{\Gamma}{2}\left(\frac{s}{1+4(\frac{\Delta - kv}{\Gamma})^2}\right). \tag{3.33}$$

For small velocities we can Taylor expand the force with respect to the velocity:

$$F \approx \hbar k \frac{\Gamma}{2}\left(\frac{s}{1+4(\frac{\Delta}{\Gamma})^2}\right) + \frac{4\hbar k^2 s}{\Gamma[1+4(\frac{\Delta}{\Gamma})^2]^2}\Delta v. \tag{3.34}$$

The net force on the atom is the sum of the forces from each beam:

$$F = F_+ - F_- \approx \frac{8\hbar k^2 s}{\Gamma[1+4(\frac{\Delta}{\Gamma})^2]^2}\Delta v. \tag{3.35}$$

For a negative detuning we then have a velocity dependent damping force:

$$F \approx -\beta v. \tag{3.36}$$

A positive detuning results in laser heating and is also a tool that can be leveraged to remove unwanted species from an ion trap. In addition to cooling for negative detunings, heating terms arise due to the random nature of spontaneous emission and stimulated absorption. These can be modeled as random walks in velocity space where the mean square velocity is non-zero [Foo12]:

$$\langle v_r \rangle^2_{\text{spon}} = \eta v_r^2 \mathcal{S} t \tag{3.37}$$

$$\langle v_r \rangle^2_{\text{abs}} = v_r^2 \mathcal{S} t \tag{3.38}$$

η accounts for the angular dependence on spontaneous emission and $v_r = \hbar k/M$ is the recoil velocity. By equating the time derivative of heating and cooling terms, the steady state minimum Doppler temperature can be calculated:

$$T_D = \frac{\hbar \Gamma}{2k_{\text{B}}}. \tag{3.39}$$

3.3 Three-Level System

Understanding two-level dynamics is important for single qubit rotations, however, a basic understanding of the three-level dynamics will be useful as well. A common configuration

encountered is the lambda system, where an excited state (which can be relatively short-lived) is connected to two lower ground states, or a lower ground state and metastable state (Fig. 3.1). If this represents the gross structure of a closed cycling transition it can be used for Doppler cooling given an appreciable excited state linewidth. Stimulated Raman transitions also make use of the lambda system, where the excited state can be adiabatically eliminated to form an effective two-level system. For our purposes below, we are interested understanding any coherent effects that arise when Doppler cooling in this type of system.

We begin by considering the case of our three-level lambda system shown in Figure 3.1, where fields connect states $|1\rangle$ and $|3\rangle$ as well as $|2\rangle$ and $|3\rangle$ with frequencies ω_B and ω_R. For now, we assume there is no spontaneous emission and that states $|1\rangle$ and $|2\rangle$ are separated enough in energy (ω_{21}) that we can ignore off-resonant effects. As before, we have already made the dipole and rotating wave approximations, and can write our free atom plus perturbation Hamiltonian as:

$$\mathcal{H} = \begin{pmatrix} 0 & 0 & \frac{\Omega_B}{2} e^{i\omega_B t} \\ 0 & \omega_{21} & \frac{\Omega_R}{2} e^{i\omega_R t} \\ \frac{\Omega_B^*}{2} e^{-i\omega_B t} & \frac{\Omega_R^*}{2} e^{-i\omega_R t} & \omega_{31} \end{pmatrix} \tag{3.40}$$

with $\omega_{21} = \omega_2 - \omega_1$ and $\omega_{31} = \omega_3 - \omega_1$. We've dropped the laser phases for convenience, and have labeled the laser and Rabi frequencies in a suggestive way. To eliminate the time-dependence from the Hamiltonian we apply the following unitary transformation:

$$U = \begin{pmatrix} e^{i\omega_B t} & 0 & 0 \\ 0 & e^{i\omega_R t} & 0 \\ 0 & 0 & 1 \end{pmatrix} \tag{3.41}$$

remembering that the effective Hamiltonian (Eq. 3.9) includes an extra term, analogous to what one sees in classical physics for a non-inertial frame.

$$\widetilde{\mathcal{H}} = \begin{pmatrix} \omega_B & 0 & \frac{\Omega_B}{2} \\ 0 & (\omega_{21} + \omega_R) & \frac{\Omega_R}{2} \\ \frac{\Omega_B^*}{2} & \frac{\Omega_R^*}{2} & \omega_{31} \end{pmatrix}. \tag{3.42}$$

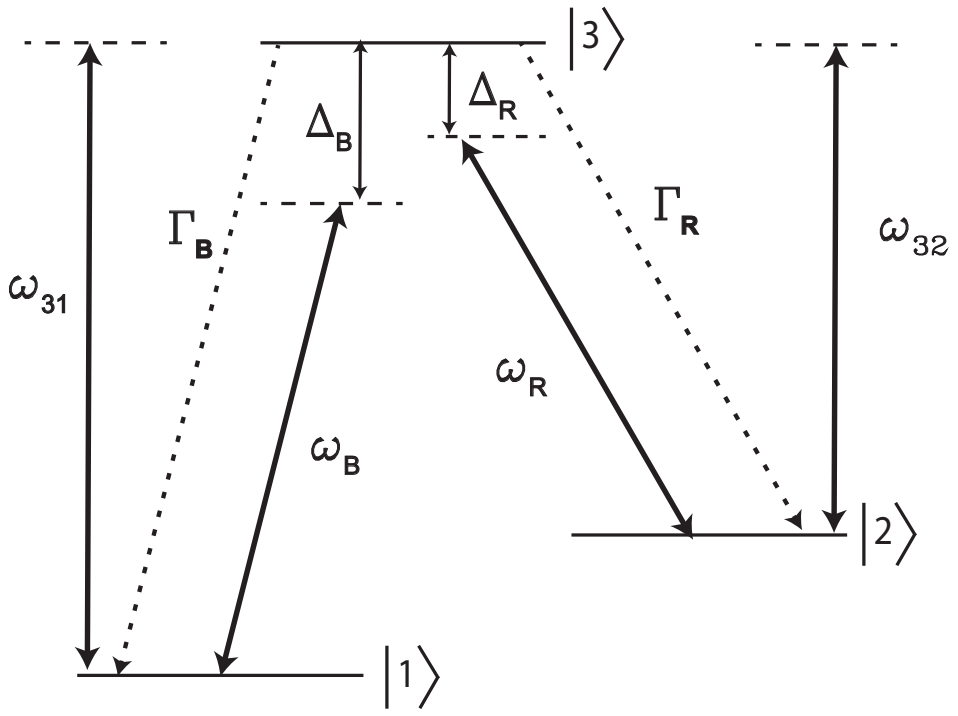

Figure 3.1: Diagram for 3-level lambda system. Two lasers connect states 1 and 3 as well as 2 and 3, with laser frequencies Ω_B and Ω_R respectively. Energy level differences are labeled ω_{31}, ω_{32}, and ω_{21} ($\hbar = 1$). Lasers are detuned from the excited state by the detunings Δ_B and Δ_R, and $|3\rangle$ decays to states $|1\rangle$ and $|2\rangle$ with linedwidth Γ_B and Γ_R. The lifetime of $|2\rangle$ is assumed to be long-lived with spontaneous emission ignored.

To bring this Hamiltonian into the standard three-level form, we note that we can always add an offset ($\mathcal{H}_0' = \mathcal{H}_0 - \mathbb{1}\omega_B$) to our free atomic Hamiltonian:

$$\widetilde{\mathcal{H}} = \begin{pmatrix} 0 & 0 & \frac{\Omega_B}{2} \\ 0 & \Delta_B - \Delta_R & \frac{\Omega_R}{2} \\ \frac{\Omega_B^*}{2} & \frac{\Omega_R^*}{2} & \Delta_B \end{pmatrix} \tag{3.43}$$

where we have defined the quantities $\Delta_B \equiv (\omega_3 - \omega_1) - \omega_B$ and $\Delta_R \equiv (\omega_3 - \omega_2) - \omega_R$.

3.3.1 Coherent Population Trapping

To gain to gain some intuition about the three-level system, we'd like to solve for the new eigenvalues and eigenstates. We make the assumption that $\Delta_B = \Delta_R \equiv \Delta$ and obtain:

$$\lambda_0 = 0 \tag{3.44}$$

$$\lambda_+ = \frac{1}{2}\left(\Delta + \sqrt{\Omega_R^2 + \Omega_B^2 - \Delta^2}\right) \tag{3.45}$$

$$\lambda_- = \frac{1}{2}\left(\Delta - \sqrt{\Omega_R^2 + \Omega_B^2 - \Delta^2}\right). \tag{3.46}$$

Solving for the eigenvectors and writing them in terms of our original basis:

$$|0\rangle \ = \frac{-\Omega_R|1\rangle \ + \Omega_B|2\rangle}{\sqrt{\Omega_B^2 + \Omega_R^2}} \tag{3.47}$$

$$|-\rangle = \frac{\Omega_B|1\rangle \ + \Omega_R|2\rangle \ + 2\lambda_-|3\rangle}{\sqrt{\Omega_B^2 + \Omega_R^2 + (2\lambda_-)^2}} \tag{3.48}$$

$$|+\rangle = \frac{\Omega_B|1\rangle \ + \Omega_R|2\rangle \ + 2\lambda_+|3\rangle}{\sqrt{\Omega_B^2 + \Omega_R^2 + (2\lambda_+)^2}}. \tag{3.49}$$

We can see that the $|0\rangle$ state does contain a component of the original excited state ($|3\rangle$), so an atom in this "dark state" state will not spontaneously emit any photons. Given an equal superposition of our two ground states and equal detunings $\Delta_B = \Delta_R$, the amplitudes of the two transitions interfere destructively resulting in zero population population transfer to the excited state. Dark states are often problematic, prohibiting or reducing the ability to Doppler cool. A solution to this problem is found by adding another term to the Hamiltonian [BB02], causing the dark state to evolve into one of the bright states over time. This is similar to a spin-1/2 system with a magnetic moment processing in an applied magnetic field. In this experiment, the extra term in the Hamiltonian is provided by a magnetic field, which also serves the purpose of defining a quantization axis.

Due to the atomic structure of Ba^+ described in Chapter 4, we'd like to understand the effect of dark states during Doppler cooling. To include relaxation effects we move to the

density matrix formalism:

$$\rho = \begin{pmatrix} |C_1|^2 & C_1C_2^* & C_1C_3^* \\ C_2C_1^* & |C_2|^2 & C_2C_3^* \\ C_3C_1^* & C_3C_2^* & |C_3|^2 \end{pmatrix} = \begin{pmatrix} \rho_{11} & \rho_{12} & \rho_{13} \\ \rho_{21} & \rho_{22} & \rho_{23} \\ \rho_{31} & \rho_{32} & \rho_{33} \end{pmatrix}. \tag{3.50}$$

To more formally describe the effects of spontaneous emission, or any decoherence mechanism for that matter, we use the Linblad Master equation [Lin76, GKS76]:

$$\frac{d\rho}{dt} = -i[H, \rho] + L_D(\rho) \tag{3.51}$$

where the Lindblad superoperator $L_D(\rho)$ is given as:

$$L_D(\rho) = \sum_i -\frac{1}{2}\left(L_i^\dagger L_i \rho + \rho L_i^\dagger L_i\right) + L_i \rho L_i^\dagger. \tag{3.52}$$

The anti-commutator describes the decay of the coherences and populations while the second term is often referred to as the repopulation term or repopulation matrix. The sum is over all possible modes of relaxation. For spontaneous emission of our lambda system, we get the following operators:

$$L_{31} = \sqrt{\Gamma_B}\ |3\rangle\langle 1| \tag{3.53}$$

$$L_{32} = \sqrt{\Gamma_R}\ |3\rangle\langle 2|. \tag{3.54}$$

For the first term of the superoperator we get:

$$\begin{pmatrix} 0 & 0 & -\frac{(\Gamma_B+\Gamma_R)}{2}\rho_{13} \\ 0 & 0 & -\frac{(\Gamma_B+\Gamma_R)}{2}\rho_{23} \\ -\frac{(\Gamma_B+\Gamma_R)}{2}\rho_{31} & -\frac{(\Gamma_B+\Gamma_R)}{2}\rho_{32} & -2(\Gamma_B+\Gamma_R)\rho_{33} \end{pmatrix} \tag{3.55}$$

and for the second:

$$\begin{pmatrix} \rho_{33}(\Gamma_B+\Gamma_R) & 0 & 0 \\ 0 & \rho_{33}(\Gamma_B+\Gamma_R) & 0 \\ 0 & 0 & 0 \end{pmatrix}. \tag{3.56}$$

We can now write down the Optical Bloch Equations (OBE), and no longer assume our laser detunings are equal:

$$
\begin{aligned}
\dot{\rho}_{11} &= -i\frac{1}{2}\Omega_B(\rho_{31}-\rho_{32}) + \Gamma_B\rho_{33} \\
\dot{\rho}_{12} &= -i[(\Delta_R-\Delta_B)\rho_{12} + \frac{1}{2}(\Omega_B\rho_{32}-\Omega_R\rho_{13})] \\
\dot{\rho}_{13} &= i[\Delta_B\rho_{13} + \frac{1}{2}\Omega_B(\rho_{11}-\rho_{33}) + \frac{1}{2}\Omega_R\rho_{12})] - \frac{\Gamma}{2}\rho_{13} \\
\dot{\rho}_{22} &= -i[\frac{1}{2}\Omega_R(\rho_{32}-\rho_{23})] + \Gamma_R\rho_{33} \\
\dot{\rho}_{23} &= i[\Delta_R\rho_{23} + \frac{1}{2}\Omega_R(\rho_{22}-\rho_{33}) + \frac{1}{2}\Omega_B\rho_{21}] - \frac{\Gamma}{2}\rho_{23} \\
\dot{\rho}_{33} &= -i[\frac{1}{2}\Omega_B(\rho_{13}-\rho_{31}) + \frac{1}{2}\Omega_R(\rho_{23}-\rho_{32})] - \Gamma_B\rho_{33} \\
\dot{\rho}_{21} &= (\dot{\rho}_{12})^* \\
\dot{\rho}_{31} &= (\dot{\rho}_{13})^* \\
\dot{\rho}_{32} &= (\dot{\rho}_{23})^*
\end{aligned}
\tag{3.57}
$$

where $\Gamma = \Gamma_B + \Gamma_R$. Note there are only five independent equations given the requirement that $\rho_{11} + \rho_{22} + \rho_{33} = 1$. To find the steady state solution we set time derivatives to zero. Equations for the populations can solved algebraically or with the assistance of computer programs. In the case of our three-level system, the solution for the population of the excited state has already been calculated [JND85]:

$$
\rho_{33} = \frac{4(\Delta_B-\Delta_R)^2\Omega_B^2\Omega_R^2\Gamma}{Z} \tag{3.58}
$$

with Z given by:

$$
\begin{aligned}
Z &= 8(\Delta_B-\Delta_R)^2\Omega_B^2\Omega_R^2\Gamma \\
&+ 4(\Delta_B-\Delta_R)^2\Gamma^2(\Omega_B^2\Gamma_R + \Omega_R^2\Gamma_B) \\
&+ 16(\Delta_B-\Delta_R)^2[\Delta_B^2\Omega_R^2\Gamma_B + \Delta_R^2\Omega_B^2\Gamma_R] \\
&- 8\Delta_B(\Delta_B-\Delta_R)\Omega_R^4\Gamma_B + 8\Delta_R(\Delta_B-\Delta_R)\Omega_B^4\Gamma_R \\
&+ (\Omega_B^2+\Omega_R^2)(\Omega_B^2\Gamma_R + \Omega_R^2\Gamma_B).
\end{aligned}
\tag{3.59}
$$

To understand the effect of CPT, we plot equation 3.58 for various laser detunings and intensities. It will be useful to use the saturation parameter (Eq. 3.29) in place of the Rabi frequency since this number is more useful in the lab. Figure 3.2 plots Δ_B versus excited state

population for various values of the saturation parameters and Δ_R detunings. The effect of CPT is clearly seen in all four panels. Panel (a) most closely represents the parameters used in this experiment when laser cooling. Panels (a), (b), and (c) represent a Fano resonance (asymmetric line-shape). CPT is often renamed electromagnetically induced transparency (EIT) when the intensity of one field is much larger than the other (panel (c)), and can be used to cool below the Doppler limit [MEK00, LMH16].

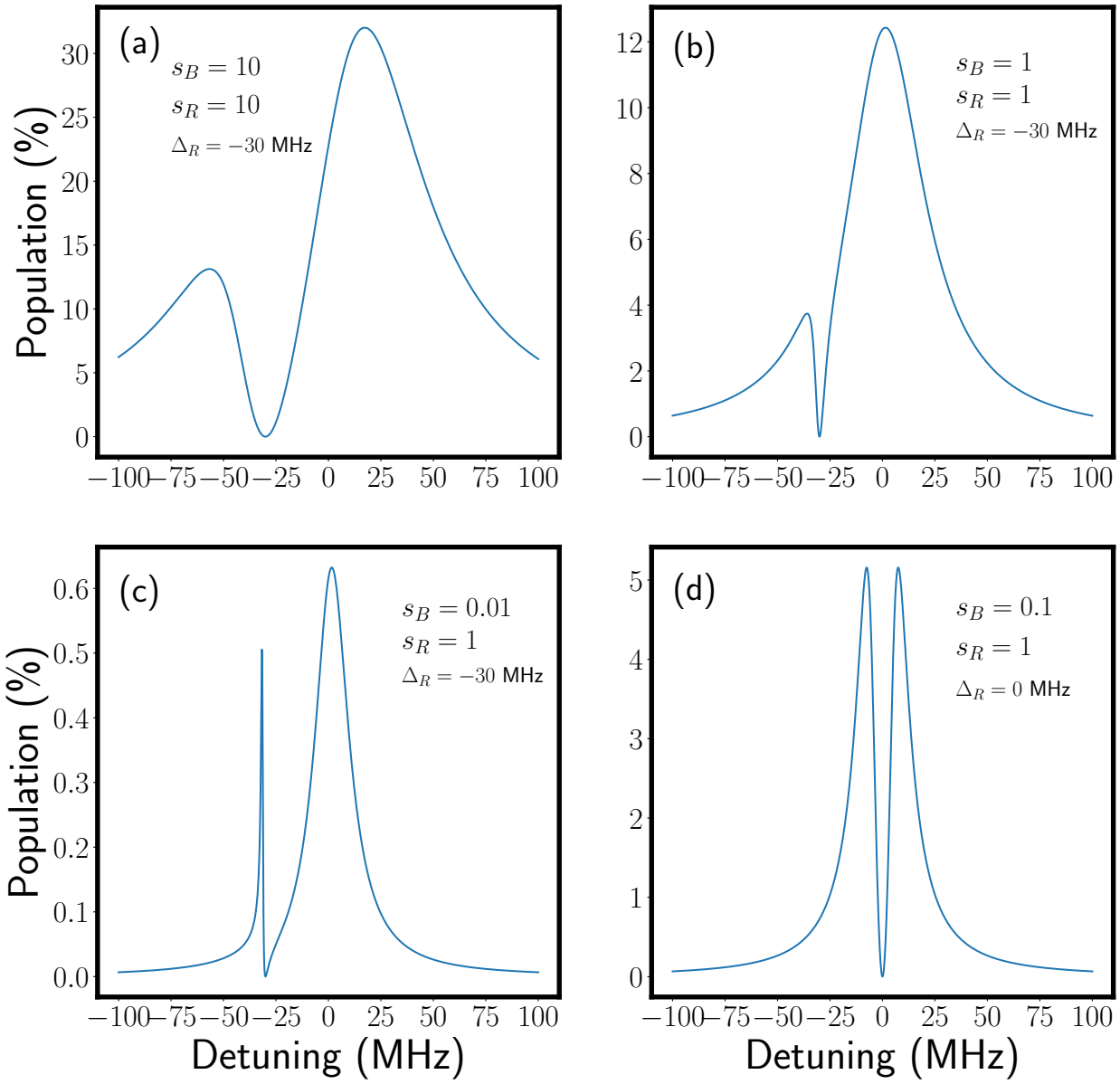

Figure 3.2: Plot of excited state population ρ_{33} versus detuning of the laser connecting states 1 and 3 (Δ_B) for a fixed detuning of the laser connecting states 2 and 3 (Δ_R). The excited state linewidths are defined using the barium linewidths (Chapter 4), $\Gamma_B = 2\pi \times 15.2$ MHz and $\Gamma_R = 2\pi \times 4.9$ MHz. Panels (a), (b), (c), and (d) show various saturation parameters and detunings. Panel (a) most closely represents the typical Doppler cooling parameters used in this experiment.

CHAPTER 4

The Barium Ion

"If we hit that bullseye, the rest of the dominoes will fall like a house of cards. Checkmate."
- Zapp Brannigan

Barium was recognized early on as a promising candidate for trapped-ion work. The first observation of quantum jumps, demonstration of sideband cooling, and image of a single ion were all performed with Ba^+ [NSD86, NHT78, NHT80]. Seven stable isotopes, many short lived radioactive species, and numerous visible wavelength electronic transitions offer advantages over other trapped-ion species. Of the seven, five are relatively abundant with two offering non-zero nuclear spin. Table 4.1 lists the isotopic abundances and basic nuclear properties of all isotopes with half-lives longer than a few days [ABB04, DBD03, MHP01, Sto05].

The gross electronic structure of Ba^+ is shown in Figure 4.1. The $^2D_{3/2}$ lifetime of $\approx$ 80 s [YND97, GBB07] and $^2D_{5/2}$ lifetime $\approx$ 30 s [ANH14, MS90, GBB07, RGL07] are the longest of all singly ionized alkali-earth and alkali-earth like elements. These provide narrow transitions near 2051 nm and 1762 nm which can be utilized for atomic clocks or as optical qubits [KHS12, DKN10]. In particular, the $^2D_{5/2}$ state is ideal for electron shelving [Deh75] and high-fidelity qubit readout [HAB14] since it is removed from the $^2S_{1/2} \leftrightarrow ^2P_{1/2} \leftrightarrow ^2D_{3/2}$ closed cycling transitions.

The $^2S_{1/2} \leftrightarrow ^2P_{1/2} \leftrightarrow ^2D_{3/2}$ lambda system is the typical choice for laser cooling, requiring only two visible wavelength lasers near 493 nm and 650 nm where high power single-mode

A	I	g_I	Abundance	Half-life
130	0		0.1%	$\sim 10^{21}$ yr
132	0		0.1%	Stable
133	1/2	-1.538(6)	0.0	$\sim$ 10.5 yr
134	0		2.4%	Stable
135	3/2	0.555836(1)	6.5%	Stable
136	0		7.8%	Stable
137	3/2	0.62491(1)	11.2%	Stable
138	0		71.6%	Stable

Table 4.1: Abundances and nuclear properties of barium isotopes with half-lives longer than a few days. The nuclear g-factor (g_I) is given in units of the nuclear magneton (μ_N).

diodes and photonic technologies are readily available[1] [2]. Coherent population trapping (CPT) enhanced by the strong $^2P_{1/2}$ branching ratio of $\approx 3:1$ results in a dark state [BB02] when the lasers are equally detuned from the $^2P_{1/2}$ state, and can be destabilized with an applied magnetic field of a few Gauss[3]. Lasers at the remaining visible and infrared (IR) wavelengths required for electron shelving and optical qubit manipulations are also readily obtainable. High power 455 nm and 1762 nm single-mode direct diodes, along with 1228 nm and 1170 nm gain chips with high efficiency second harmonic generation (SHG) waveguides are commercially available.

Before we begin describing the details and features of the various isotopes further, it will be helpful to review the atomic theory relevant for this work.

[1] For non-zero nuclear spin isotopes, additional rempumping sidebands are required for laser cooling, easily achieved using electro optical modulators (EOMs).

[2] A second set of closed cycling transitions exist between the $^2S_{1/2}$, $^2P_{3/2}$, $^2D_{3/2}$, and $^2D_{5/2}$ states.

[3] Modulating the laser polarization will also destabilize dark states.

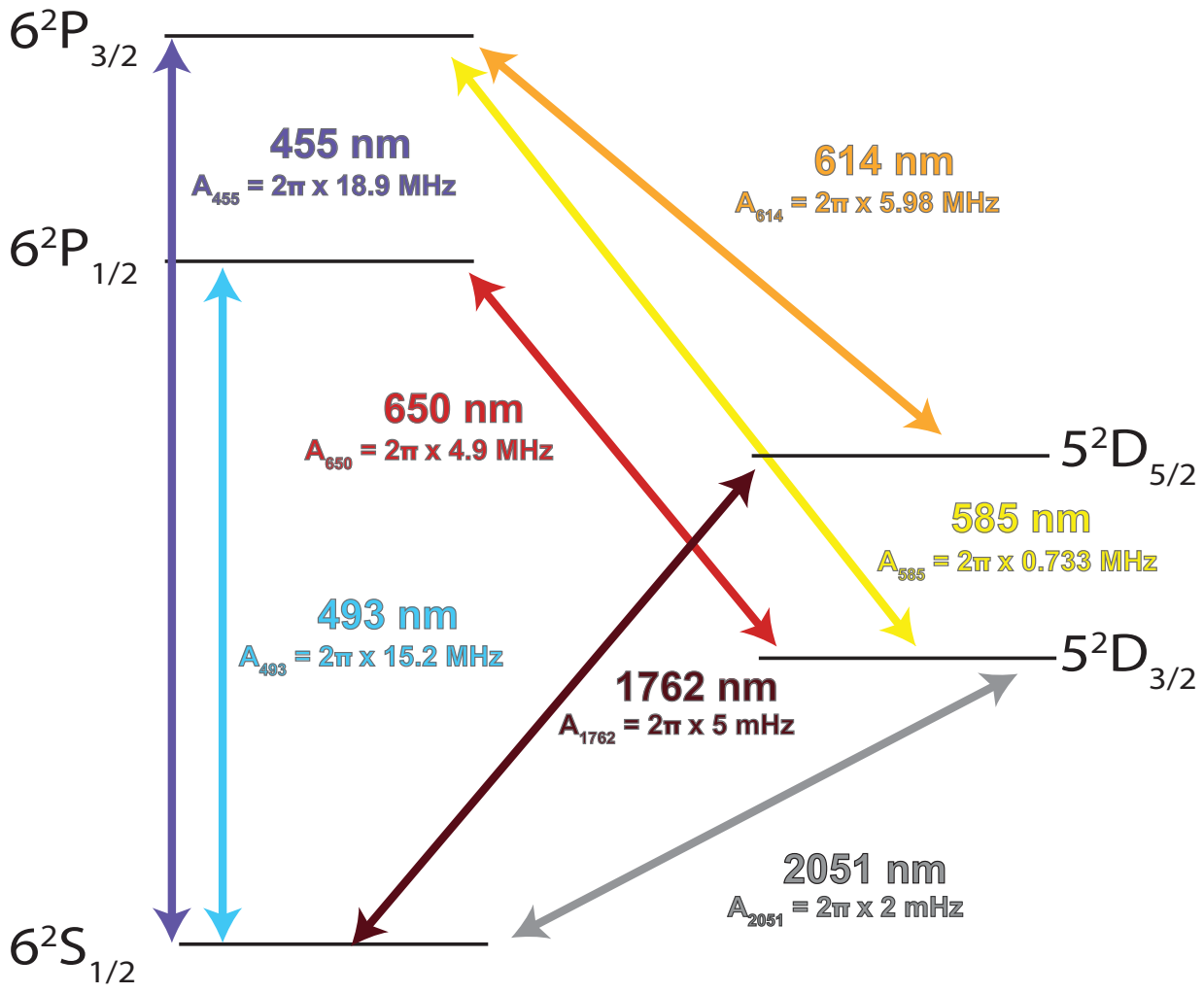

Figure 4.1: Gross Ba^+ energy level diagram with transition wavelengths and Einstein A coefficients [DDY16, DSV92]. Visible wavelength electronic transitions requiring lasers near 493 nm and 650 nm, or lasers near 455 nn, 585 nm, and 614 nm can be used for Doppler cooling. In addition, the long-lived D states can be used for electron shelving or a narrow clock transition in the infrared (IR).

4.1 Atomic Structure

4.1.1 Hyperfine Structure

For isotopes with non-zero nuclear spin, the energy associated with the interaction of the nuclear and electron spin magnetic dipole moments causes an additional splitting of the electronic levels. This is known as the hyperfine interaction, and depending on the electronic state, varies from hundreds of megahertz to tens of gigahertz for species used in this work. The magnetic moment of the nucleus is defined as:

$$\boldsymbol{\mu_I} = g_I \mu_N \boldsymbol{I} \tag{4.1}$$

where g_I is the nuclear g-factor, μ_N the nuclear magneton:

$$\mu_N = \mu_B \frac{m_e}{m_p} \tag{4.2}$$

m_e and m_p the electron and proton masses, and $\boldsymbol{I}$ the nuclear spin. The Hamiltonian is given by:

$$\mathcal{H}_{HF} = -\boldsymbol{\mu_I} \cdot \boldsymbol{B}_e \tag{4.3}$$

where $\boldsymbol{B}_e$ is the magnetic field at the nucleus due to the electron. The magnetic field consists of contributions from the orbital motion and intrinsic spin angular momentum of the electron [Woo18]. The field due to the orbital motion is given by:

$$\boldsymbol{B}_l = \frac{\mu_0}{4\pi} \frac{(-e\boldsymbol{v}) \times (-\boldsymbol{r})}{r^3} = -2\frac{\mu_0 \mu_B}{4\pi r^3} \boldsymbol{L} \tag{4.4}$$

with $(-\boldsymbol{r})$ the co-ordinate of the nucleus with respect to the electron, $\boldsymbol{L}$ the orbital angular momentum, and $-e\boldsymbol{r} \times \boldsymbol{v} = -2\mu_B \boldsymbol{L}$. The magnetic field due to the electron spin magnetic dipole moment is given by:

$$\boldsymbol{B}_s = -\frac{\mu_0}{4\pi} \frac{1}{r^3} \left[\boldsymbol{\mu}_s - \frac{3(\boldsymbol{\mu}_s \cdot \boldsymbol{r})\boldsymbol{r}}{r^2} \right] + \frac{2\mu_0}{3} \boldsymbol{\mu}_s \delta^3(\boldsymbol{r}) \tag{4.5}$$

with spin dipole moment $\boldsymbol{\mu}_s = -2\mu_B \boldsymbol{S}(g_s = 2)$, and electron spin $\boldsymbol{S}$. The Hamiltonian then is given by:

$$\begin{aligned} \mathcal{H} = &\frac{\mu_0 \mu_B \mu_N g_I}{2\pi r^3} \left((\boldsymbol{I} \cdot \boldsymbol{L}) + \left[\frac{3(\boldsymbol{S} \cdot \boldsymbol{r})(\boldsymbol{I} \cdot \boldsymbol{r})}{r^2} + (\boldsymbol{I} \cdot \boldsymbol{S}) \right] \right) + \\ &\frac{4\mu_0 \mu_B \mu_N g_I}{3} (\boldsymbol{I} \cdot \boldsymbol{S}) \delta^3(\boldsymbol{r}). \end{aligned} \tag{4.6}$$

The first term in large parenthesis has two components: the energy associated with the electron orbital angular momentum and the nuclear magnetic dipole moment, and the "finite distance" dipole-dipole interaction between the nuclear and electron spin dipole moments (square brackets). The term with the Dirac delta function is known as the "Fermi contact," and accounts for the dipole-dipole interaction when there is non-zero overlap of the electron wavefunction at the nucleus. The term is only present for unpaired electrons in s-orbitals.

The first order energy shift of the given electronic state is given by the expectation value of $\mathcal{H}$. We begin by considering the the case for $l \neq 0$[4]. The term with the delta function in the Hamiltonian vanishes since the probability density of the electronic wavefuntion at the nucleus is zero. In this case, it can be shown that [Woo18]:

$$\mathcal{H}_{l\neq 0} = \mathcal{A}_{l\neq 0}(\boldsymbol{I}\cdot\boldsymbol{J}) \tag{4.7}$$

with $\boldsymbol{J} = \boldsymbol{L} + \boldsymbol{S}$, and $\mathcal{A}$ the "hyperfine A constant":

$$\mathcal{A}_{l\neq 0} = \frac{\mu_0\mu_b\mu_N g_I}{2\pi}\left\langle\frac{1}{r^3}\right\rangle\frac{l(l+1)}{j(J+1)}. \tag{4.8}$$

For the case of $l = 0$, only the last term in Equation 4.6 survives, and is given by:

$$\mathcal{H}_{l=0} = \mathcal{A}_{l=0}(\boldsymbol{I}\cdot\boldsymbol{J}) \tag{4.9}$$

with:

$$\mathcal{A}_{l=0} = \frac{2}{3}\mu_0\mu_b\mu_N g_I|\psi(0)|^2. \tag{4.10}$$

In general we will write the Hamiltonian as:

$$\mathcal{H} = \mathcal{A}(\boldsymbol{I}\cdot\boldsymbol{J}) \tag{4.11}$$

using the appropriate $\mathcal{A}$ constant for the electronic state of interest. In either case, the Hamiltonian no longer commutes with the operators $\boldsymbol{I}$ and $\boldsymbol{J}$. We define the new operator $\boldsymbol{F} = \boldsymbol{I} + \boldsymbol{J}$, and write the energy as:

$$E_{HF} = \frac{\mathcal{A}}{2}[F(F+1) - I(I+1) - J(J+1)] \tag{4.12}$$

[4] $L^2|l, m_l\rangle = l(l+1)|l, m_l\rangle$

with F and m_F the new good quantum numbers. Conveniently, the energy difference between levels is given by:

$$E_{HF}(F) - E_{HF}(F-1) = \mathcal{A}F. \tag{4.13}$$

In addition to the interaction of the magnetic moments, if the nucleus is not spherically symmetric, the nuclear charge distribution can have an electric quadrupole moment that interacts with the gradient of the electric field of the electron. This contribution to the energy can be the same order of magnitude as the magnetic dipole interaction. More generally, nuclei with spin I can have higher moments, with the magnetic octupole moment ($\boldsymbol{\Omega}$) coming after the the electric quadrupole moment ($\boldsymbol{Q}$). The contributions from the higher moments are written in terms of addtional hyperfine constants:

$$\mathcal{H}_{HF} = \mathcal{A}(\boldsymbol{I}\cdot\boldsymbol{J}) + \mathcal{B}f_Q(\boldsymbol{I},\boldsymbol{J}) + \mathcal{C}f_\Omega(\boldsymbol{I},\boldsymbol{J}) + \ldots \tag{4.14}$$

with the first few functions f_Q and f_Ω given by [Arm71]:

$$f_Q = \frac{3(\boldsymbol{I}\cdot\boldsymbol{J})^2 + \frac{3}{2}(\boldsymbol{I}\cdot\boldsymbol{J}) - I(I+1)J(J+1)}{2I(2I-1)J(2J-1)} \tag{4.15}$$

$$\begin{aligned} f_\Omega = \Big[&10(\boldsymbol{I}\cdot\boldsymbol{J})^3 + 20(\boldsymbol{I}\cdot\boldsymbol{J})^2 \\ &+ 2(\boldsymbol{I}\cdot\boldsymbol{J})[-3I(I+1)J(J+1) + I(I+1) + J(J+1) + 3] \\ &- 5I(I+1)J(J+1)\Big] \Big/ \Big[I(I-1)(2I-1)J(J-1)(2J-1)\Big]. \end{aligned} \tag{4.16}$$

By looking at the denominators, it can be seen that contributions from these higher moments only occur if both I and J are greater than one-half for the electric quadrupole moment, and greater than one for the magnetic octupole moment. This means only the $J \geq 3/2$ states in $^{137}Ba^+$ and $^{135}Ba^+$ have higher order contributions to the hyperfine splittings.

4.1.2 Hyperfine Structure and Zeeman Splitting

In barium, a magnetic field of a few Gauss is typically applied to destabilize dark states as well as define a quantization axis. This leads to an additional interaction in the form of:

$$\mathcal{H}_Z = \boldsymbol{\mu}\cdot\boldsymbol{B} \tag{4.17}$$

termed Zeeman interaction, where $\boldsymbol{\mu}$ is the total magnetic moment and $\boldsymbol{B}$ the applied magnetic field. In the low magnetic field limit $\mathcal{H}_Z \ll \mathcal{H}_{HF}$, this interaction can be treated as a perturbation on the hyperfine states. The total magnetic moment is given by:

$$\boldsymbol{\mu} = g_J \mu_B \boldsymbol{J} + g_I \mu_N \boldsymbol{I} \tag{4.18}$$

where g_J is the Landé g-factor. Since the nuclear magneton is much smaller than the Bohr magneton, we drop the second term and get:

$$E_Z = g_J \mu_B \langle \boldsymbol{J} \cdot \boldsymbol{B} \rangle. \tag{4.19}$$

By taking the average projection of $\boldsymbol{J}$ along $\boldsymbol{B} = B_0 \hat{z}$ we get:

$$E_Z = g_F \mu_B B_0 m_F \tag{4.20}$$

with g_F given by:

$$g_F = \frac{F(F+1) + J(J+1) - I(I+1)}{2F(F+1)} g_J \tag{4.21}$$

and g_J given by:

$$g_J = \frac{3}{2} + \frac{S(S+1) + J(J+1) - I(I+1)}{2F(F+1)} \tag{4.22}$$

assuming $g_s \approx 2$ and $g_L = -1$. This calculation is typically sufficient for most needs, and knowing the Bohr magneton is $\mu_B = 1.4$ MHz/G in frequency units simplifies estimating Zeeman shifts.

When the Zeeman shifts become the same order as the hyperfine splitting (large B-field) perturbation theory no longer holds. In this case, the two Hamiltonians ($\mathcal{H}_{HF}$ and $\mathcal{H}_Z$) must be treated on equal footing and considered a perturbation of the fine structure Hamiltonian. For an introductory example see [Gri05]. Even for the case of low magnetic field, treating both perturbations on equal footing will give us a more precise estimate of the energy level shifts. Using the hyperfine states $|F; m_F\rangle$ as a basis, the new perturbation Hamiltonian can be formed which will include both diagonal and off-diagonal elements[5]. The new energy

[5]Instead the basis $|M_I M_J\rangle$ could be used in which case $\mathcal{H}_Z$ would give diagonal terms and $\mathcal{H}_{HF}$ would give off-diagonal terms. Either way, the eigenvalues are the same. However, it turns out that $|m_F\rangle$ is a good quantum number so one can immediately calculate which matrix elements are zero when using the hyperfine states as a basis.

eigenvalues are found by diagonalizing the perturbation Hamiltonian, and in the case where one of the angular momenta $I, J = 1/2$, an analytic solution can be calculated. This is given by the well known Breit-Rabi formula [BR31]:

$$\begin{aligned} E_{F=J\pm1/2} &= -\frac{\Delta E_{HF}}{2(2J+1)} + g_J \mu_B m_F B \\ &\pm \frac{\Delta E}{2}\sqrt{1 + \frac{4(g_J\mu_B - g_I\mu_N)m_F B}{(2J+1)\Delta E_{HF}} + \left[\frac{(g_J\mu_B - g_I\mu_N)B}{\Delta E_{HF}}\right]^2}. \end{aligned} \tag{4.23}$$

ΔE_{HF} is the hyperfine splitting with no magnetic field present, and is positive if the hyperfine A constant is positive, and negative if the hyperfine A constant is negative. This formula shows that even for $m_F = 0$ states, there is still a non-zero energy shift, where in our earlier approximation the shift was zero.

4.1.3 Isotope Shifts

Finally, we turn to the last bit of atomic structure relevant to this work. The frequency of a given electronic transition changes between isotopes and the difference similar in magnitude to the hyperfine splitting. The shift is made up of two parts, the first called the mass shift, and given by the following equation [HS74]:

$$\delta\nu^{i\ mass}_{A,A'} = (M^i_{NMS} + M^i_{SMS})\frac{A - A'}{AA'} \tag{4.24}$$

$\delta\nu^{i\ mass}_{A,A'}$ is defined as the frequency shift of the i-th electronic transition between two masses A and A'. The term M^i_{NMS} is called the normal mass shift (NMS), and is just the replacement of the electron mass with the reduced mass. The term M^i_{SMS} is called the specific mass shift (SMS), and arises when more then one electron is present. The SMS originates from correlations in the momenta of various electrons, and can be thought of as arising from the formation of multi-electron "quasiparticles" [Kin84]. In general, the SMS is difficult to calculate and is usually a measured quantity.

The second contribution to the isotope shift is called the field shift (FS), or sometimes the volume shift, given by:

$$\delta\nu^{i\ field}_{A,A'} = F^i \lambda_{A,A'}. \tag{4.25}$$

The factor F^i only depends on the i-th electronic transition, and is essentially a measure of the wavefunction overlap at the nucleus, largest for s-orbital electrons. The second factor is given by:

$$\lambda_{A,A'} = \delta\langle r^2\rangle_{A,A'} + C_1\delta\langle r^4\rangle_{A,A'} + C_2\delta\langle r^6\rangle_{A,A'} + ... \tag{4.26}$$

and describes the nuclear charge parameters. In general, contributions from higher charge moments can be neglected, leaving only the difference in the mean square nuclear charge radii [HS74]:

$$\lambda_{A,A'} = \delta\langle r^2\rangle_{A,A'}. \tag{4.27}$$

For the total isotope shift of the i-th electronic transition we have:

$$\delta\nu^i_{A,A'} = F^i\delta\langle r^2\rangle_{A,A'} + M^i\frac{A-A'}{AA'} \tag{4.28}$$

with $M^i = M^i_{NMS} + N^i_{SMS}$.

We now consider two electronic transitions in a given atomic species ($i \in \{\mathrm{r}, \mathrm{b}\}$) for a given pair of isotopes (A, A'). Solving for the difference in the mean square nuclear charge radii of the r-electronic transition we get:

$$\delta\langle r^2\rangle_{A,A'} = \frac{1}{F^{\mathrm{r}}}\left[\delta\nu^{\mathrm{r}}_{A,A'} - M^{\mathrm{r}}(\frac{A-A'}{AA'})\right]. \tag{4.29}$$

Plugging this into the formula for the isotope shift of our second transition $\delta\nu^{\mathrm{b}}_{A,A'}$ and rearranging we get:

$$\left(\frac{AA'}{A-A'}\delta\nu^{\mathrm{b}}_{A,A'}\right) = \frac{F^{\mathrm{b}}}{F^{\mathrm{r}}}\left(\frac{AA'}{A-A'}\delta\nu^{\mathrm{r}}_{A,A'}\right) - \left(\frac{F^{\mathrm{b}}}{F^{\mathrm{r}}}M^{\mathrm{r}} + M^{\mathrm{b}}\right). \tag{4.30}$$

This is a surprising result. When the isotope shifts of two electronic transitions are plotted against each other, normalized by the factor $\frac{AA'}{A-A'}$, the points all fall on a straight line. This is known as a King plot [Kin63] and can be utilized for estimating isotopes shifts or measuring nuclear deformation.

4.2 Stable Isotopes

4.2.1 Nuclear Spin Zero

The five nuclear spin-zero ($I = 0$) isotopes of barium (Table 4.1) share the same general electronic structure shown in Figure 4.2. Due to the relatively simple structure and favorable

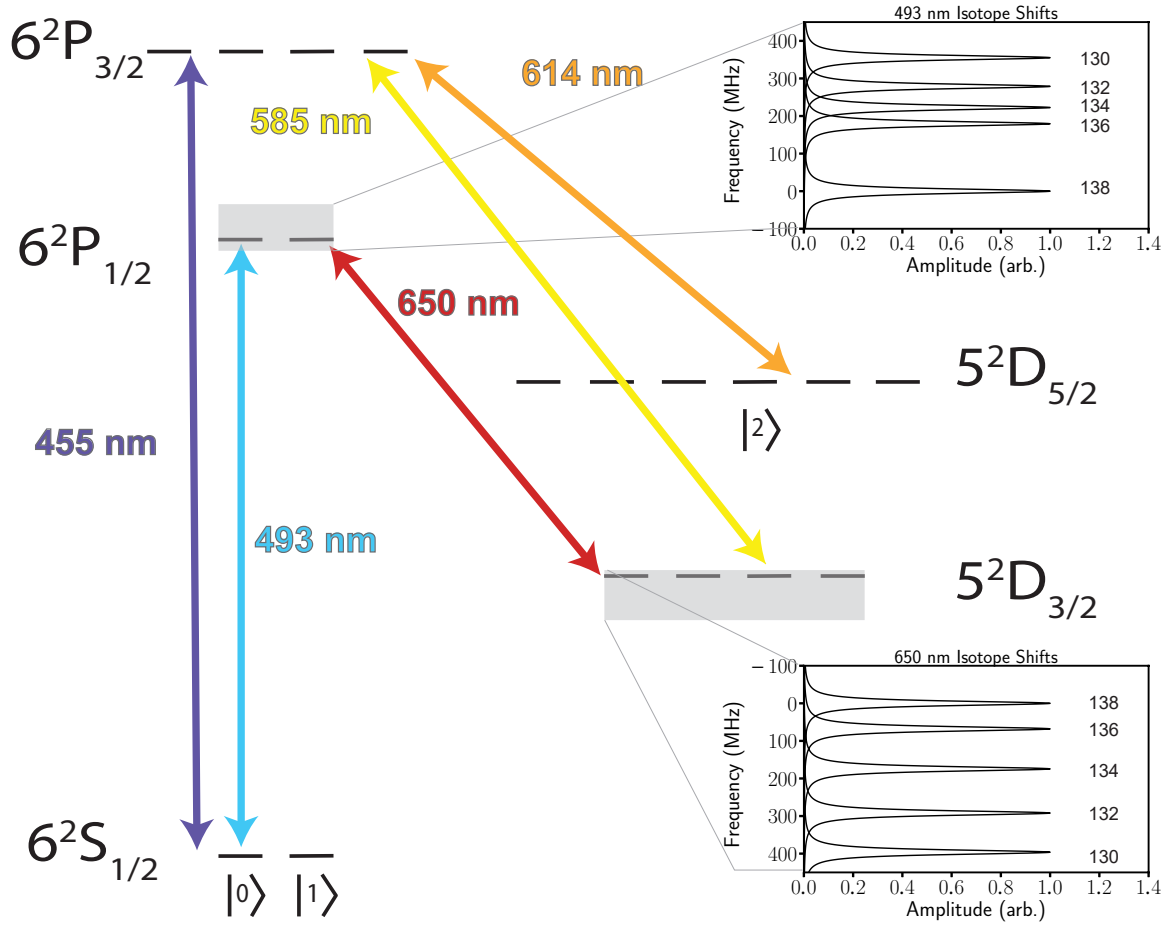

Figure 4.2: Level structure for even barium isotopes with zero nuclear spin ($I = 0$). Inset shows the isotope shifts of the $^2P_{1/2} \leftrightarrow ^2S_{1/2}$ and $^2P_{1/2} \leftrightarrow ^2D_{3/2}$ transitions. As described in the text, a decrease in atomic mass number leads to an increase in transition frequency.

wavelengths, even isotopes of barium are used in a variety of AMO experiments [DC13, SDC16, RSS13] including multi-species traps to sympathetically cool co-trapped atomic or molecular ions [SZB18, ROW05, SHL14, SKD16]. Zeeman qubits can be defined in the $^2S_{1/2}$

manifold, and optical qubits between the $^2D_{5/2} \leftrightarrow ^2S_{1/2}$ states. High-fidelity readout of the Zeeman qubit can be achieved by shelving on the $^2P_{3/2} \leftrightarrow ^2S_{1/2}$ stretched-state transition and pulsed repumping with 585 nm, alternating between σ^+-light and π-light to prevent mixing of the qubit levels.

The even isotope shifts of the $^2P_{1/2} \leftrightarrow ^2S_{1/2}$ (493 nm) and $^2P_{1/2} \leftrightarrow ^2D_{3/2}$ (650 nm) have the feature where linearly decreasing the mass leads to a monotonic increase in the transition frequency (Table 4.2). When laser cooling $^{138}Ba^+$, the laser frequencies are red-detuned of all the other isotopes, and it is possible to simultaneously cool and image multiple barium species. In this experiment, with the imaging system described in the next chapter, the three most abundant isotopes ($^{138}Ba^+$,$^{136}Ba^+$,$^{134}Ba^+$) can all be imaged simultaneously on an EMCCD camera.

This advantageous structure also makes removing heavier even isotopes straightforward by means of laser heating. Instead of a negative detuning in equation 3.35, the laser is blue-detuned leading to a decrease in the ion's phase space density. By simply changing the laser frequencies to cool one of the lighter even isotopes, the heavier ones are heated out from the trap.

4.2.1.1 650 nm Spectroscopy (Weak Probe Line scan)

While the isotope shifts of the $^2P_{1/2} \leftrightarrow ^2D_{3/2}$ electronic transition were reported in the literature for $^{138}Ba^+$, $^{136}Ba^+$, and $^{134}Ba^+$ [VAH93], the remaining two even isotopes were not. With a naturally abundant source and the ability to distill single $^{132}Ba^+$ and $^{130}Ba^+$ ions, spectroscopy measurements were possible.

Previous measurements of electronic transitions in other isotopes were made using a beam of ions, where interrogation times are short but a continual source of new ions is always available. These measurements needed to account for Doppler shifts due to the angle of the laser with respect to the atomic beam, as well as the resulting temperature of the

ions when produced from a thermal oven.[6]. Heating effects from the laser-ion interaction can be ignored since the time the ions see the laser is short. However, trapped ions suffer from Doppler heating and loss of signal when trying to measure and electronic transition blue-detuned of atomic resonance. Typical measurement of an electronic transition is made by setting all required cycling lasers red-detuned approximately half an atomic linewidth, and scanning the required laser over the transition to be measured. As the laser approaches resonance, the population in the excited state increases leading to increased spontaneous emission and an increase in the detected number of photons. However, once blue-detuned of the transition, Doppler heating quickly heats the ion. Even if the ion does not leave the trapping region, the increase in energy causes an increase in the amplitude of the motion which either takes the ion out of the laser beams or Doppler shifts the ion out of resonance. An immediate loss of signal occurs as there is no longer appreciable population in the excited state. A typical scan of this type of measurement is shown in Figure 4.3.

To avoid this unwanted heating during measurement, application of the required laser frequency (probe beam) can be rapidly alternated with a Doppler cooling beam [WBG08, Pru14]. The probe beam saturation parameter of $s \ll 1$ is applied for a short duration and prevents significant heating when blue-detuned of atomic resonance. For measurements of the $^2P_{1/2} \leftrightarrow ^2D_{3/2}$ isotope shifts near 650 nm, the cooling beam is a first-order sideband generated by modulating a fiber electro optic modulator (EOM), and is detuned approximately half an atomic linewidth with a saturation parameter of $s_{\text{cool}} \approx 10$. The probe beam, a first-order sideband generated from the same laser and EOM, has a saturation parameter that is much smaller than the cooling beam, experimentally reduced until no further reduction in linedwidth is measured ($s_{\text{probe}} \approx 0.1$). The EOM is modulated with two separate RF sources, combined with a power splitter, with each individually turned on and off with separate RF switches. The carrier of the 650 nm laser is detuned by 4 GHz where off-resonant effects are negligible. Figure 4.4 shows the experimental sequence for the 650 nm line scan for $^{132}Ba^+$ and $^{130}Ba^+$. In previously reported experiments, the repumping laser was extinguished

[6]Atoms produced from a thermal oven can have temperatures of ~ 500 °C or more.

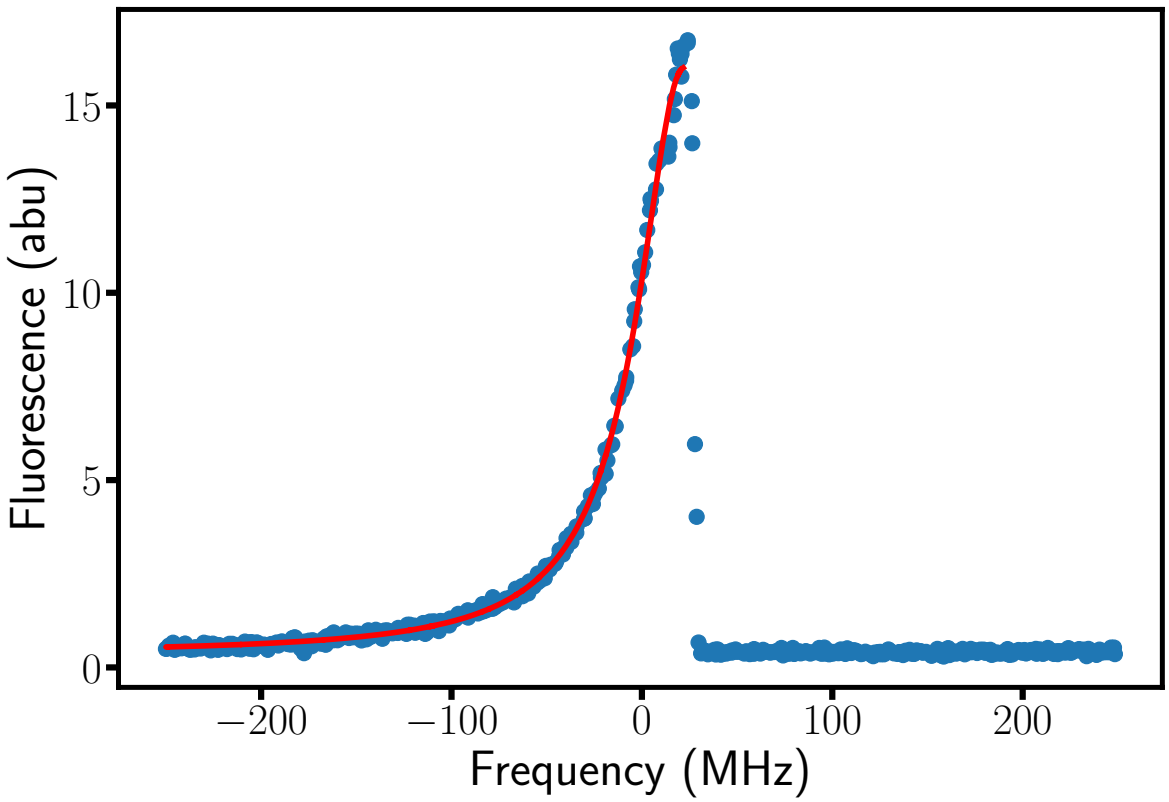

Figure 4.3: Standard line scan of the $^2P_{1/2} \leftrightarrow ^2S_{1/2}$ transition (Fig. 4.2). The 493 nm and 650 nm laser are initially detuned half an atomic linewdith from resonance. The 493 nm laser is then scanned approximately 250 MHz on either side of the resonant frequency. As soon as the laser frequency is larger then the transition frequency, Doppler heating causes an immediate loss of fluorescence. Red line fits half the data to a Lorentzian profile.

during the probe portion of the experiment. Here, the 493 nm laser (repumper) is always applied and detuned for optimal cooling. Cooling is applied for 150 μs, after which the probe laser is applied for 25 μs. The cycle is repeated 40,000 times per probe frequency, and the frequency of the probe is scanned approximately 300 MHz on either side of atomic resonance. At each probe frequency, fluorescence is collected only during the probe portion of the experimental cycle. A scan of the 650 nm transition in $^{132}Ba^+$ and $^{130}Ba^+$ is plotted in Figure 4.5. Using these data, we find $\delta\nu^{650}_{132,138} = 292(1)_{\text{stat}}$ MHz and $\delta\nu^{650}_{130,138} = 394(1)_{\text{stat}}$ MHz. Scans have $\pm$ 20 MHz systematic uncertainty primarily due to wavemeter drift [Hig14].

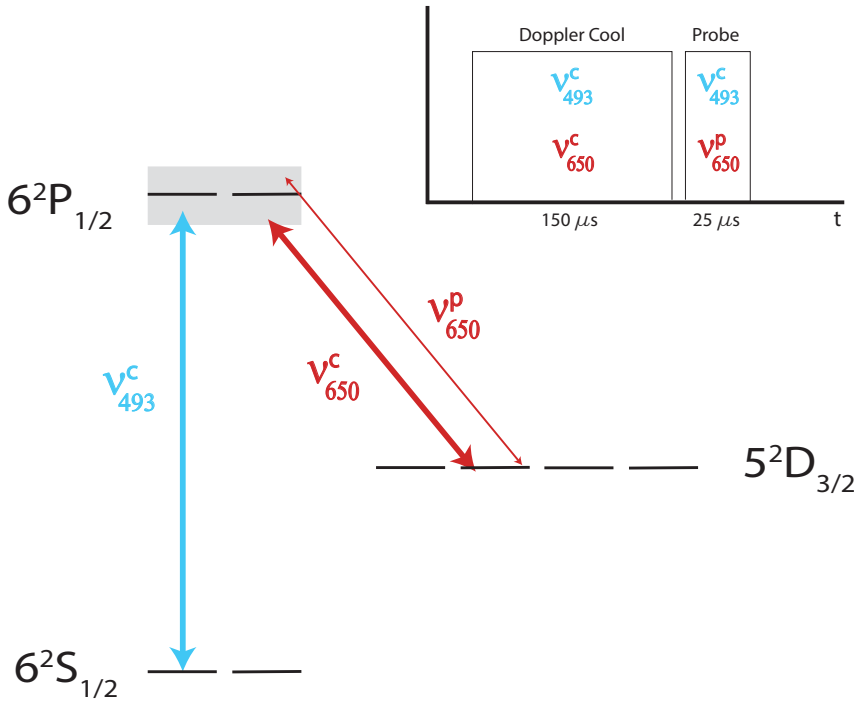

Figure 4.4: Level diagram and sequence for weak probe line scan.

4.2.2 Nuclear Spin-3/2

Two of the stable isotopes ($^{137}Ba^+$,$^{135}Ba^+$) have nuclear spin $I = 3/2$. The level structure now includes the hyperfine interaction as shown in Figure 4.6. The additional rich structure can be used to define hyperfine qubits or qudits[7][LWC19], and both ground-state hyperfine qubits and optical qubits defined between the $^2D_{5/2} \leftrightarrow ^2S_{1/2}$ states have been previously investigated [DKN10]. The isotope shifts also have the same feature where a linear decrease in mass leads to a monotonic increase in both the 493 nm and 650 nm transition frequencies (Table 4.3). Isotopes shifts between electronic transitions with hyperfine structure are defined from the hyperfine centroids[8]. For states with $J \geq 3/2$, the electric quadrupole of the nucleus provides an additional contribution to the hyperfine splitting and is written in terms of the hyperfine $\mathcal{B}$ constant (Eq. 4.14). The hyperfine $\mathcal{A}$ and $\mathcal{B}$ constants are given in Table 4.3.

[7]Qubit is a 2-level quantum bit while a qudit is the general term for an N-level quantum bit.

[8]The hyperfine centroid is the value of the energy level in the absence of the hyperfine interaction. The centroid can be calculated using equation 4.14.

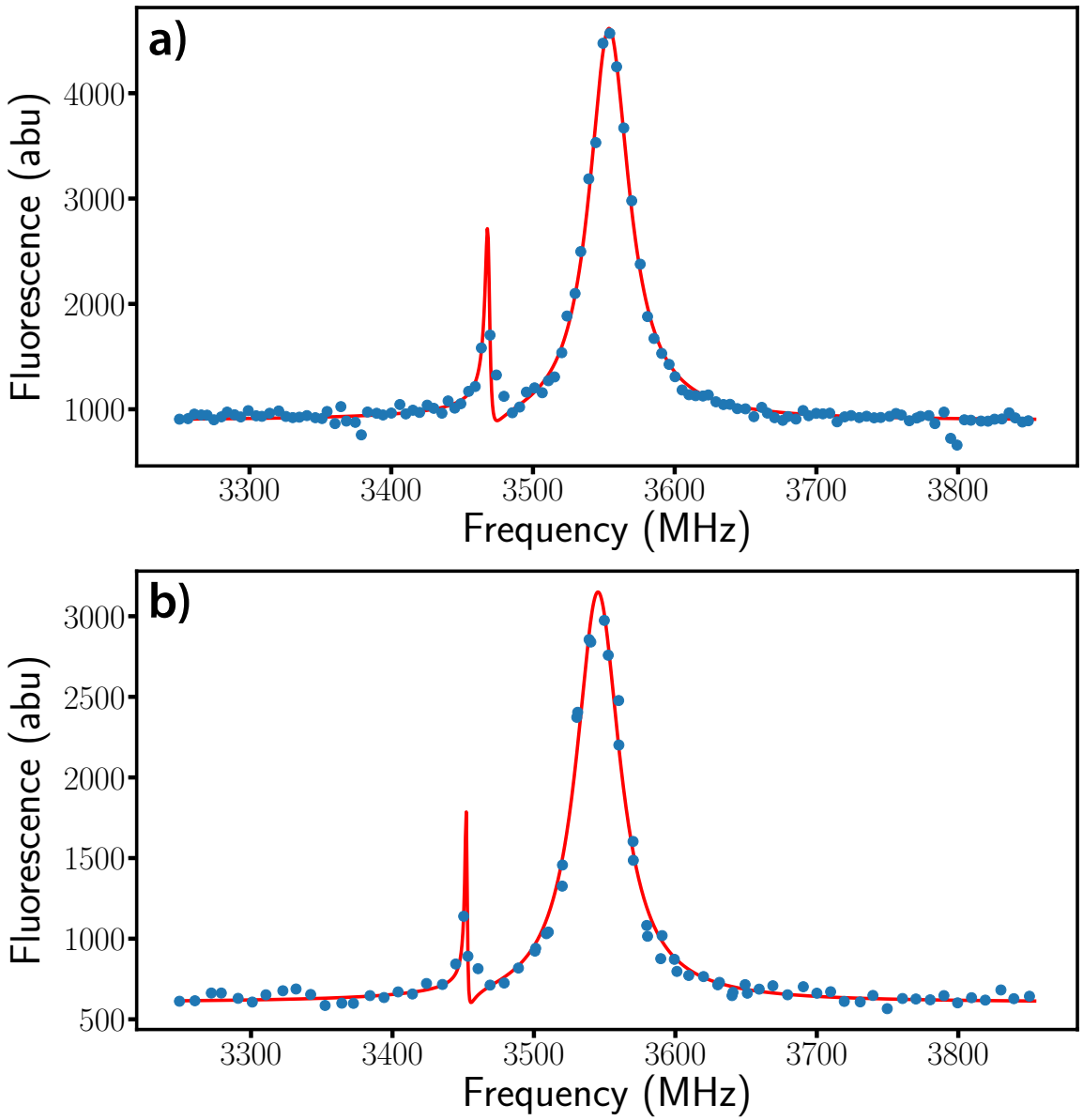

Figure 4.5: Scan of the $^2P_{1/2} \leftrightarrow {}^2D_{3/2}$ transition in (a) $^{132}Ba^+$ and (b) $^{130}Ba^+$ using a weak probe beam to interrogate the ion. Alternating between Doppler cooling and low laser intensity probing allows for the scan of the transition without significant heating to the ion and loss of fluorescence for detection. Blue points are collected data, solid red curve is a fit to equation 3.58 with the addition of an overall scale factor and a constant offset to account for background light scatter. Using these data, we find $\delta\nu^{650}_{132,138} = 292(20)$ MHz and $\delta\nu^{650}_{130,138} = 394(20)$. Scans have ± 20 MHz systematic uncertainty primarily due to wavemeter drift.

A	$\delta\nu^{493}$	$\delta\nu^{650}$	$\delta\nu^{455}$	$\delta\nu^{585}$	$\delta\nu^{614}$
130	355.3(4.4)	$\mathbf{394(1)}_{\text{stat}}$	372.3(4.9)	413.2(3)	426.0(3)
132	278.9(4)	$\mathbf{292(1)}_{\text{stat}}$	294.9(4.2)	301.7(3)	311.4(3)
134	222.6(3)	174.5(8)	233.9(3.7)	188.2(3)	194.7(3)
136	179.4(1.8)	68.0(5)	186.9(2.1)	76.1(3)	80.3(3)
138	$\equiv 0$	$\equiv 0$	$\equiv 0$	$\equiv 0$	$\equiv 0$

Table 4.2: Isotope shifts of the visible electronic transitions shown in Figure 4.2 for isotopes with nuclear spin zero. All values are in MHz. The isotope shift of the i-th electronic transition is defined relative to $^{138}Ba^{+}$ and is given by $\delta\nu^{i} \equiv \nu^{i}_{A} - \nu^{i}_{138}$. The bolded values are spectroscopic measurements from this work and have a systematic uncertainty of ± 20 MHz. All other isotope shifts are reported from references [VBB85, WAB84, VAH93, SBD80, HBB82].

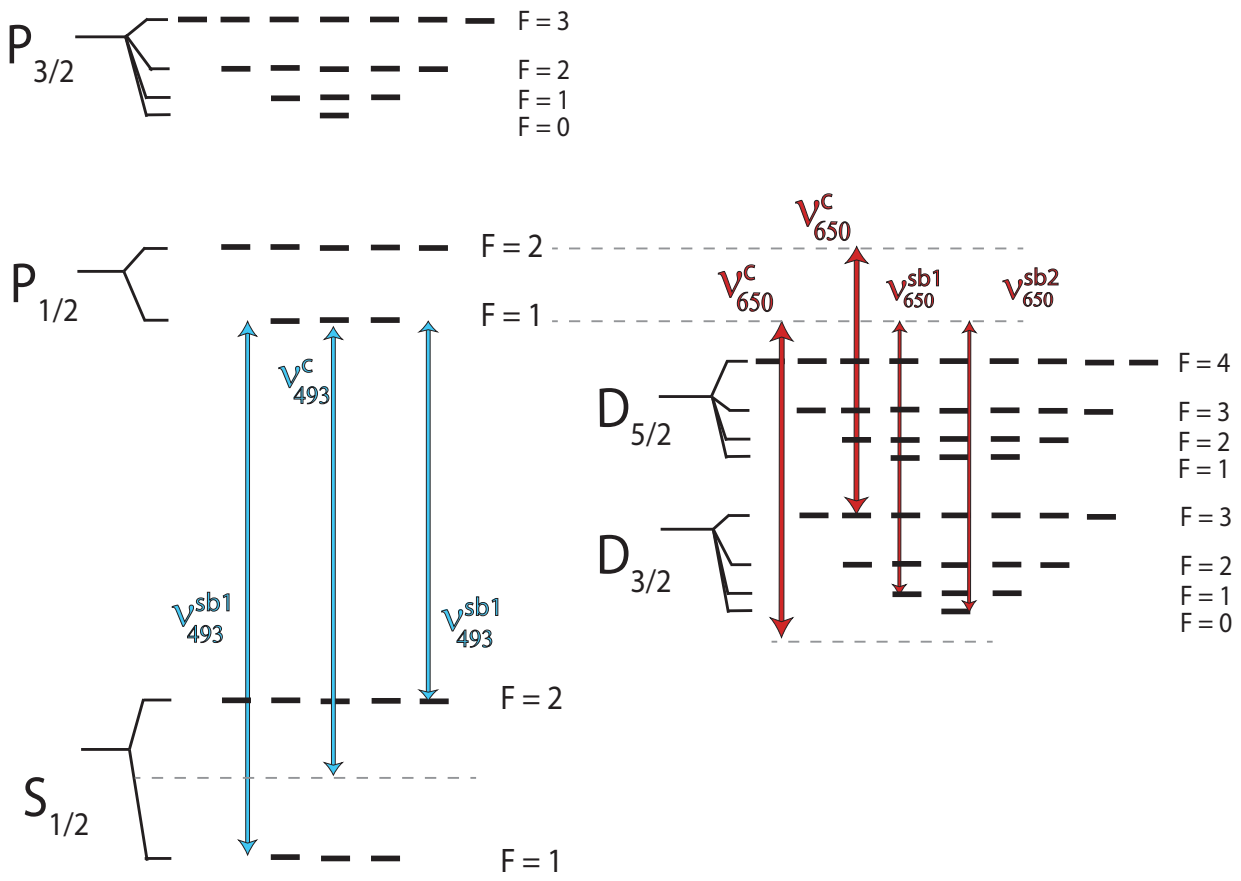

Figure 4.6: Level structure for the isotopes $^{137}Ba^{+}$ and $^{135}Ba^{+}$ with nuclear spin $I = 3/2$. Cooling is achieved by tuning the 493 nm laser carrier between center of the $^{2}S_{1/2}$ hyperfine splitting and the $|^{2}P_{1/2};F = 1\rangle$ manifold, with first order sidebands resonant with the $|^{2}P_{1/2};F = 1\rangle \leftrightarrow |^{2}S_{1/2};F = 1\rangle$ and $|^{2}P_{1/2};F = 1\rangle \leftrightarrow |^{2}S_{1/2};F = 2\rangle$ transitions.

A	I	$\mathcal{A}_{S_{1/2}}$	$\mathcal{A}_{P_{1/2}}$	$\mathcal{A}_{P_{3/2}}$	$\mathcal{A}_{D_{3/2}}$	$\mathcal{A}_{D_{5/2}}$	$\mathcal{B}_{P_{3/2}}$	$\mathcal{B}_{D_{3/2}}$	$\mathcal{B}_{D_{5/2}}$
135	3/2	3591.67011718(24)	664.6(3)	113.0(1)	169.5892(9)	-8.3(10)	59.0(1)	28.9536(25)	45.2(10)
137	3/2	4018.87083385(18)	743.7(3)	127.2(2)	189.7288(6)	-7.4(10)	92.5(2)	44.5417(16)	80.7(10)
A	I	$\delta\nu^{493}$	$\delta\nu^{650}$	$\delta\nu^{455}$	$\delta\nu^{585}$	$\delta\nu^{614}$			
135	3/2	348.6(2.1)	82.7(6)	360.7(2.2)	96.9(3)	103.8(3)			
137	3/2	271.1(1.7)	-13.0(4)	279.0(2.6)	-7.4(3)	-3.2(3)			
138	0	$\equiv 0$	$\equiv 0$	$\equiv 0$	$\equiv 0$	$\equiv 0$			

Table 4.3: Isotope shifts of the visible wavelength electronic transitions (Fig. 4.6) and hyperfine $\mathcal{A}$ and $\mathcal{B}$ constants for $^{137}Ba^{+}$ and $^{135}Ba^{+}$. The isotope shift of the i-th electronic transition is defined relative to $^{138}Ba^{+}$ and given by $\delta\nu^{i} \equiv \nu_A^i - \nu_{138}^i$, where ν_A^i is the centroid frequency. All isotope shifts and hyperfine constants are reported from references [VBB85, WAB84, VAH93, SBD80, HBB82] with values given in MHz.

While there are multiple ways to Doppler cool these two isotopes, we use a scheme similar to the one described in [DK02]. The 493 nm laser carrier (ν^c_{493}) is tuned between the middle of the $^2S_{1/2}$ hyperfine splitting and the $|^2P_{1/2};F = 1\rangle$ manifold (Fig. 4.6). A fiber EOM phase modulates the laser producing first order sidebands resonant with the two $^2S_{1/2}$ hyperfine manifolds and the $|^2P_{1/2};F = 1\rangle$ manifold. Decays are only allowed to the $F = 2, 1, 0$ manifolds of the $^2D_{3/2}$ via dipole selection rules, however, off-resonant scatter to the $|^2P_{1/2};F=2\rangle$ can lead to population in $|^2D_{3/2};F=3\rangle$. The rumpuming scheme of the $^2D_{3/2}$ manifolds was dictated by the existing oscillators and amplifiers in our lab intended for use with $^{133}Ba^+$. To repump all four manifolds, we place the 650 nm laser carrier (ν^c_{650}) resonant with the $|^2P_{1/2};F=2\rangle \leftrightarrow |^2D_{3/2};F=3\rangle$ transition. The carrier is also $\approx$ 500 MHz blue-detuned of the $|^2P_{1/2};F=1\rangle \leftrightarrow |^2D_{3/2};F=0\rangle$ transition. A fiber EOM is used to add two frequency sidebands resonant with the $|^2P_{1/2};F=1\rangle \leftrightarrow |^2D_{3/2};F=0\rangle$ and $|^2P_{1/2};F=1\rangle \leftrightarrow |^2D_{3/2};F=1\rangle$ transitions (ν^{sb1}_{650} and ν^{sb2}_{650}). The resulting second-order sidebands have enough power and are close enough in frequency to repump the $|^2D_{3/2};F=2\rangle$.

This cooling scheme is ideal for heating out barium isotopes with nuclear spin $I = 0$, leaving only $^{137}Ba^+$ or $^{135}Ba^+$ ions. The 493 nm laser carrier (ν^c_{493}) is blue-detuned from all even isotopes, ranging from a few MHz to $\approx$ 400 MHz. This detuning is ideal for Doppler heating since larger frequency separations would lead to insignificant scattering and no average increase in kinetic energy. In addition, off-resonant carrier scattering on the $|^2P_{1/2};F=1\rangle \leftrightarrow |^2S_{1/2};F=1,2\rangle$ transitions when cooling $^{137}Ba^+$ and $^{135}Ba^+$ is negligible due to the large detunings. Using the scheme described, a pure chain of thirty $^{135}Ba^+$ ions was distilled from a naturally abundant source and is shown in Figure 4.7. The probability of loading a pure chain based on natural abundance is $(0.065)^{30} \approx 10^{-36}$. Isolating $^{135}Ba^+$ ions from a naturally abundant source is easiest to achieve since $^{137}Ba^+$ ions will also be Doppler heated when the lasers are at the $^{135}Ba^+$ cooling frequencies.

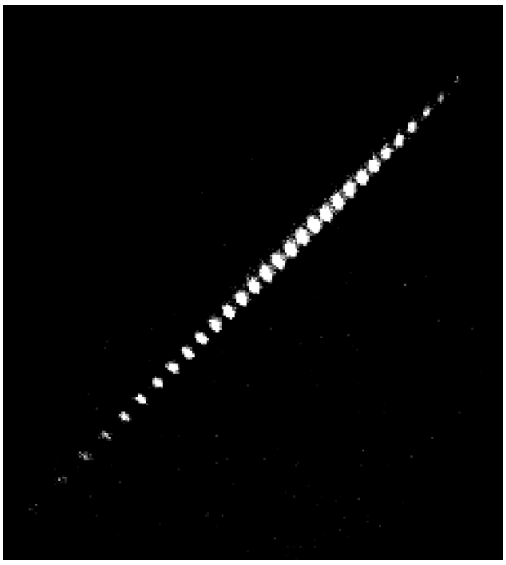

Figure 4.7: Pure chain of thirty $^{135}Ba^{+}$ ions distilled from a naturally abundance source using the frequencies shown in Figure 4.6. Probability of loading $(0.065)^{30} \approx 10^{-36}$.

4.3 $^{133}Ba^{+}$

$^{133}Ba^{+}$ is an attractive candidate for trapped-ion quantum computing due to its visible wavelength electronic transitions, spin-1/2 nucleus, and long-lived D states. While others [Die09] in the community had previously considered $^{133}Ba^{+}$ as a qubit host, the 10.5 year half-life seems to have discouraged anyone from seriously attempting its use. The initial goals of this work were (1) demonstrate efficient loading of $^{133}Ba^{+}$ with low source activities and moderate radiation shielding, (2) measurement of the unknown spectroscopy required for laser cooling and basic qubit manipulations. Details on the available qubit levels, demonstration of qubit manipulations, and high-fidelity state preparation and measurement (SPAM) are described in detail in Chapter 6. Further details regarding the radioactive nature of $^{133}Ba^{+}$, its availability, and information potentially useful for future experiments can be found in Appendix A.

4.3.1 Estimating Unknown State Energies

The general level structure of $^{133}Ba^{+}$ is shown in Figure 6.2. Previous work measured the

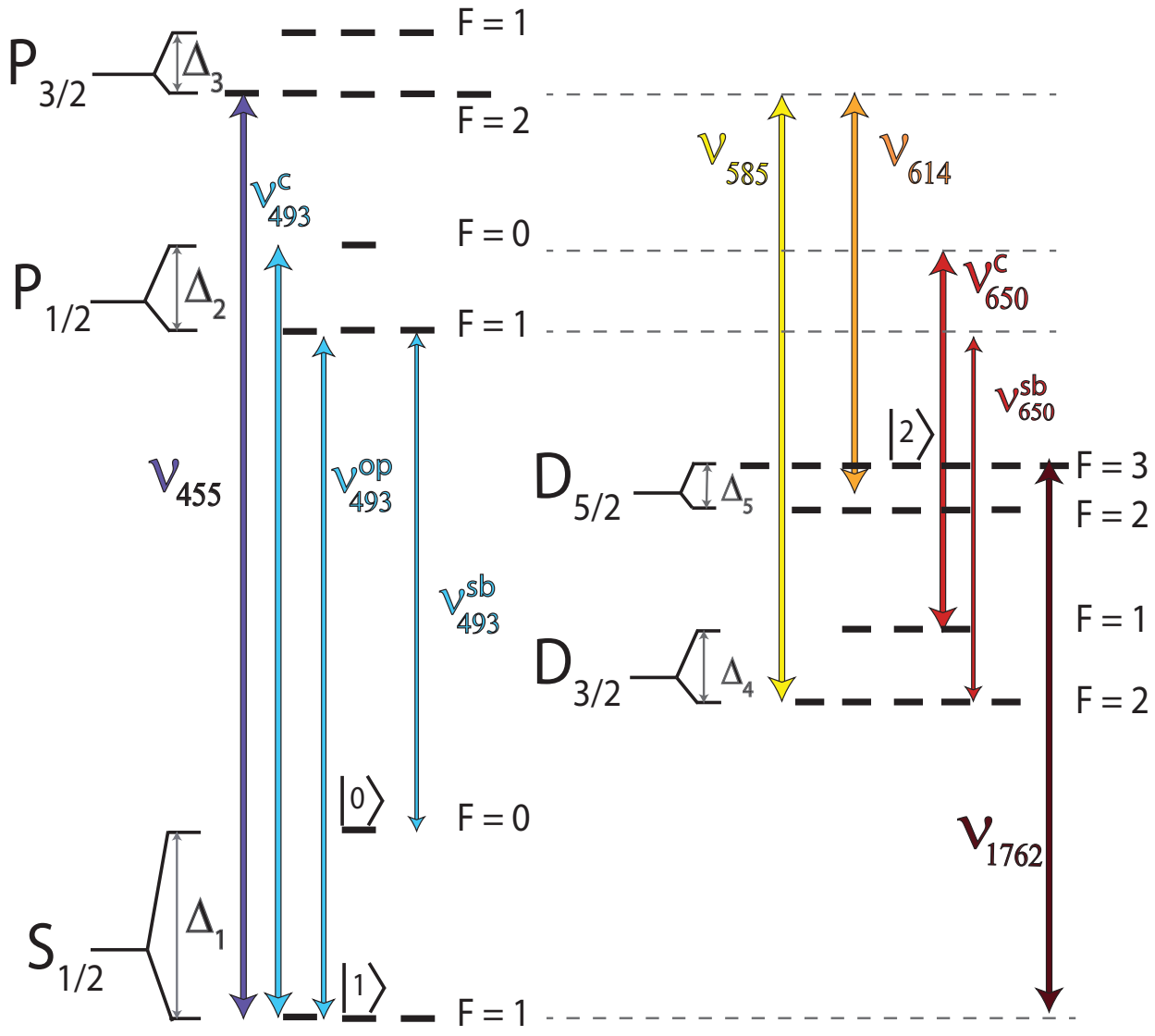

Figure 4.8: Energy level diagram of $^{133}Ba^{+}$ and frequencies used for laser cooling qubit manipulations.

$^2S_{1/2}$ hyperfine splitting to an impressive precision, Δ_1 =9925453554.49(10) Hz [KSW87]. In that experiment, ions were loaded via thermionic emission into an RF Paul trap, but used an H_2 buffer gas as opposed to Doppler cooling to reduce the temperature of the ions. The isotope shift of the $^2P_{1/2} \leftrightarrow ^2S_{1/2}$ electronic transition and $^2P_{1/2}$ hyperfine splitting were also measured using a hollow cathode tube lamp cooled with liquid nitrogen [HHM76]. In order to laser cool, the $^2P_{1/2} \leftrightarrow ^2D_{3/2}$ isotope shift and $^2D_{3/2}$ hyperfine splitting needed be

known, as $\approx 25\%$ of decays from the $^2P_{1/2}$ are to the $^2D_{3/2}$ states (Fig 4.1). To estimate the unknown hyperfine splittings, we refer back to Equations 4.10 and 4.8 for the hyperfine $\mathcal{A}$ constant. We also note that since $I = 1/2$ in $^{133}Ba^+$, there are no higher order contributions to the hyperfine splitting (Eq. 4.14). Taking the ratio of $\mathcal{A}$ constants of different isotopes for the same electronic state gives:

$$\frac{\mathcal{A}_{l\neq 0}}{\mathcal{A}'_{l\neq 0}} = \frac{g_I^A \left\langle \frac{1}{r^3} \right\rangle^A}{g_I^{A'} \left\langle \frac{1}{r^3} \right\rangle^{A'}} \tag{4.31}$$

for states with $l \neq 0$, and

$$\frac{\mathcal{A}_{l=0}}{\mathcal{A}'_{l=0}} = \frac{g_I^A \left|\psi(0)\right|_A^2}{g_I^{A'} \left|\psi(0)\right|_{A'}^2} \tag{4.32}$$

for states with $l = 0$. In either case, we can assuming the electronic radial wavefunctions are approximately equal between isotopes, resulting the ratio of $\mathcal{A}$ constants becoming the ratio of g-factors. Since there are no electric quadrupole or magnetic octupole contributions in $^{133}Ba^+$, the measured nuclear g-factors and hyperfine constants in tables 4.1 and 4.3 can be used to estimate all hyperfine splittings. The validity of the approximation can be tested by comparing the measured ground state hyperfine splitting in $^{133}Ba^+$ with the predicted values from $^{137}Ba^+$ and $^{135}Ba^+$. The estimated values are $\mathcal{A}_{S_{1/2}} \approx 9939$ MHz using $^{135}Ba^+$, and $\mathcal{A}_{S_{1/2}} \approx 9888$ MHz using $^{137}Ba^+$. Using the interval rule for the energy difference between two hyperfine levels:

$$\Delta E_{HF} = E_F - E_{F-1} = \mathcal{A}F \tag{4.33}$$

the hyperfine splittings are estimated as $\Delta_1 = 9939$ MHz and $\Delta_1 = 9888$ MHz. These are only different from the measured value by 0.2% and 0.3% respectively. Table 4.4 lists the estimated values for all hyperfine splittings in $^{133}Ba^+$ using both $^{135}Ba^+$ and $^{137}Ba^+$.

With the hyperfine splittings calculated, estimates of the unknown isotope shifts remain for laser cooling. Using the previously measured isotope shifts (Table 4.2) of the $^2P_{1/2} \leftrightarrow ^2S_{1/2}$ and $^2P_{1/2} \leftrightarrow ^2D_{3/2}$ electronic transitions, a King plot (Eq. 4.30) is made and shown in figure 4.9. The fitted slope of -0.26 is close to the theoretical value of -0.288 [ORF88] and the fitted intercept is -59.5 MHz/amu. Using the fit parameters and the previously reported isotope shift $\delta\nu^{493}_{133,138} = 355$ MHz, the isotope shift of the $^2P_{1/2} \leftrightarrow ^2D_{3/2}$ transition in $^{133}Ba^+$ was

	$S_{1/2}$	$P_{1/2}$	$P_{3/2}$	$D_{3/2}$	$D_{5/2}$
135	9937	1828	625	938	69
137	9888	1828	625	930	56

Table 4.4: Estimated hyperfine splittings in $^{133}Ba^{+}$ using measured $^{137}Ba^{+}$ and $^{135}Ba^{+}$ hyperfine $\mathcal{A}$ constants (Table 4.3) as well as measured nuclear g-factors (Table 4.1). All values given in MHz.

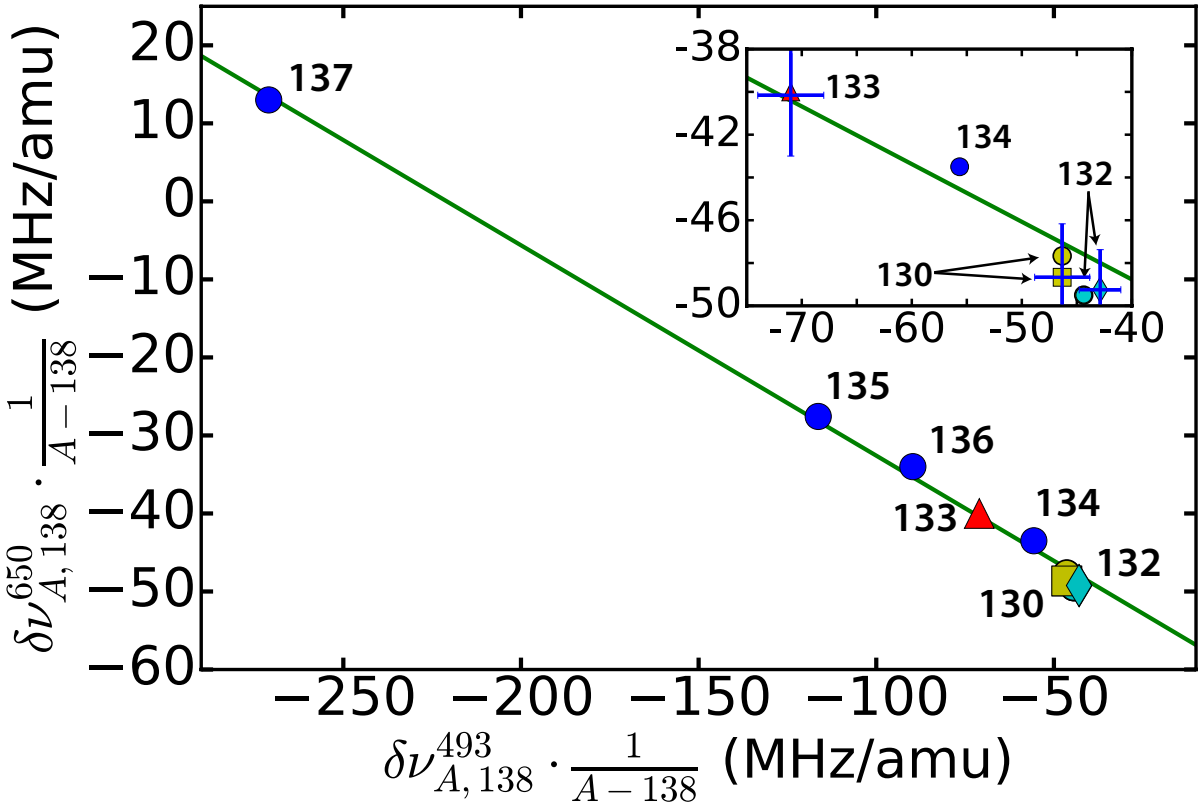

Figure 4.9: King plot [Kin63] of the $^2P_{1/2} \leftrightarrow ^2D_{3/2}$ transition *vs.* the $^2P_{1/2} \leftrightarrow ^2S_{1/2}$ transition. Each point represents the pair of masses (A, 138). Isotope shifts are normalized by the mass difference of each pair. Circles are previously reported [VBB85, WAB84, VAH93, SBD80, HBB82] where the triangle, square and diamond include measurements from this work.

estimated to be $\delta\nu^{650}_{133,138} = 198$ MHz. King plots of the 493 nm transition versus the 455 nm (614 nm) transition were also made giving estimated isotope shifts of $\delta\nu^{455}_{133,138} = 389$ MHz ($\delta\nu^{614}_{133,138} = 217$ MHz).

With the energy levels estimated, the goal of demonstrating the first laser cooled $^{133}Ba^{+}$ ion was achieved and described in what follows.

4.3.2 Laser Cooling

A laser near 493 nm is slightly red-detuned (≈ 30 MHz) from the $|^2P_{1/2};F{=}0\rangle \leftrightarrow |^2S_{1/2};F{=}1\rangle$ transition, denoted ν^c_{493} in Fig. 6.2. Transitions between the $|^2P_{1/2};F{=}0\rangle \leftrightarrow |^2S_{1/2};F{=}0\rangle$ are forbidden, but eventually off-resonant scattering via the $|^2P_{1/2};F{=}1\rangle$ states will trap the population in the $|^2S_{1/2};F{=}0\rangle$ state. To return the atom to the cooling cycle, an additional frequency is applied resonant with the $|^2P_{1/2};F{=}1\rangle \leftrightarrow |^2S_{1/2};F{=}0\rangle$ transition (ν^{sb}_{493}). In this experiment, ν^{sb}_{493} is generated with a fiber EOM (denoted 493 nm EOM) driven at $f = (\Delta_1 + \Delta_2)/2 = 5.872$ GHz (second-order sideband) with saturation parameter less than one. A re-pumping laser near 650 nm is slightly red-detuned of the $|^2P_{1/2};F{=}0\rangle \leftrightarrow |^2D_{3/2};F{=}1\rangle$ transition, denoted ν^c_{650} (Fig. 6.2). Dipole selection rules prevent decay of the $|^2P_{1/2};F{=}0\rangle$ state to the $|^2D_{3/2};F{=}2\rangle$ states, however, the $|^2P_{1/2};F{=}1\rangle \leftrightarrow |^2D_{3/2};F{=}2\rangle$ transition is allowed. The off-resonant scatter rate out of the $|^2D_{3/2};F{=}2\rangle$ states from the applied laser frequency ν^c_{650} is greater than the decay rate into the state due to off-resonant scatter from the application of laser frequency ν^c_{493}. Therefore, only the three frequencies ν^c_{493}, ν^{sb}_{493}, and ν^c_{650} are required to cool and crystallize $^{133}Ba^{+}$. To improve cooling, ν^c_{650} passes through a fiber EOM (denoted 650 nm EOM) driven at 904 MHz resulting in a first order sideband (ν^{sb}_{650}) red-detuned from the $|^2P_{1/2};F{=}1\rangle \leftrightarrow |^2D_{3/2};F{=}2\rangle$ transition, shown in Figure 6.2.

4.3.3 Loading & Distillation

A source of ^{133}Ba atoms is produced by drying a commercially available [EZ] solution of neutron activated $BaCl_2$ dissolved in 0.1 M HCl on a platinum ribbon substrate (see Appendix D). The calibration certificate reports that approximately 2% of the total barium atoms are ^{133}Ba. According to manufacturer, before production of ^{133}Ba begins an enriched source of ^{132}Ba is produced to improve the activation efficiency. This isotope dominates the remaining 98% of barium atoms, confirmed by laser cooling as well as a laser-cooling-assisted mass

spectrometry (LAMS) (see chapter 5). ^{134}Ba abundance is estimated at $\sim 1\%$, and no other isotopes are loaded from the radioactive source[9].

With the trap rf switched off, atomic barium ions are produced by laser-ablating the $BaCl_2$ on the platinum ribbon substrate using a 532 nm, 0.2-0.4 mJ, 5-7 ns laser pulse focused down to a 40 μm waist (80 μm beam diameter). After a delay period of 20 μs, optimized for maximum capture efficiency, the trap rf voltage turns on confining ions. Since typical kinetic energies produced by laser ablation range from 5-50 eV [WH00], a 20 μs delay indicates loading of the low energy portion (≈ 0.1 eV) of the ion kinetic energy distribution. Typically, adjusting the ablation energy allows changing the number of ions loaded from approximately 10 to 100. However, a discrete jump is often observed, with the minimum possible change in ablation laser energy ($\Delta E \sim 50$ μJ) resulting hundreds in of ions loaded from zero. Theoretical models indicate each laser pulse at our stated fluence produces $\sim 10^{11}$ Ba atoms [PTH88], resulting in a loading efficiency of order 10^{-9}-10^{-10}, comparable to loading using an oven and photo-ionization [SM89, DAB06, SGS06]. The large abundance of $^{132}Ba^+$ allows us to confirm loading from the radioactive source by ablating the target with the cooling lasers red-detuned of all even isotope transitions. The laser is then swept blue across the resonances of the even isotopes (Fig. 4.2), and fluorescence is monitored to determine which masses are present. Figure 4.10b shows an image of typical cloud of $^{132}Ba^+$ ions loaded from the radioactive source.

Empirical results show loading with the laser carriers near 493 nm and 650 nm red-detuned of the $^{132}Ba^+$ resonant cooling frequencies with no other tones, followed by a sweep to the $^{133}Ba^+$ frequencies (Fig. 4.10a) produced the most consistent loading of $^{133}Ba^+$. Both 493 nm and 650 nm lasers are stabilized via a software lock with the transition between frequencies taking approximately 3 seconds. Initially after the sweep, ν^h_{493} is red-detuned of all even isotope transitions to provide sympathetic cooling of $^{133}Ba^+$ via laser cooling of $^{132}Ba^+$ or $^{134}Ba^+$. ν^h_{493} is a first-order sideband generated simultaneously with ν^{sb}_{493} using

[9] In some of the first loading attempts $^{138}Ba^+$ ions were observed. We believe this was from a reflected high energy laser pulse. After optimization much lower pulse energies were used and only $^{132}Ba^+$, $^{133}Ba^+$, and $^{134}Ba^+$ were observed.

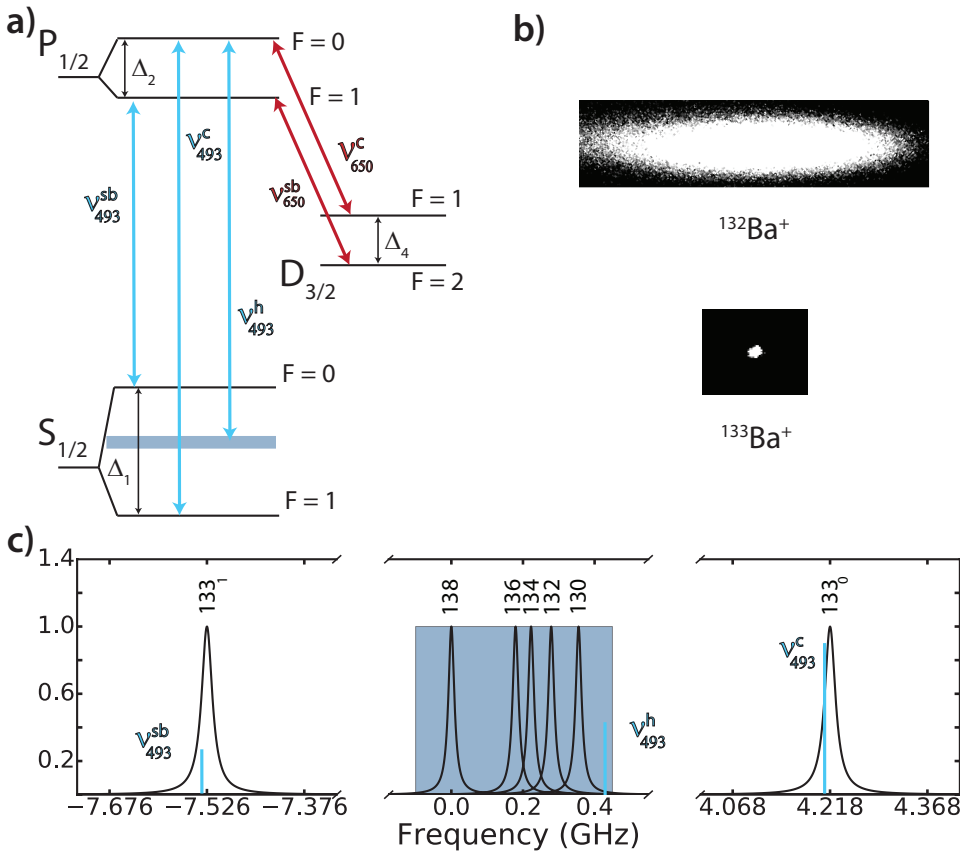

Figure 4.10: (a) Laser cooling transitions for the $A = 133$ isotope of barium II with hyperfine structure of the underlying states. (b) A single $^{133}Ba^+$ ion and an isotopically pure $^{132}Ba^+$ ion cloud loaded from an enriched microgram source of barium atoms. (c) Laser loading scheme of $^{133}Ba^+$ for the $6^2S_{1/2} \leftrightarrow 6^2P_{1/2}$ transition. To Doppler cool $^{133}Ba^+$, the laser carrier ν^c_{493} is stabilized 4.218(10) GHz above the $^{138}Ba^+$ resonance. The frequency ν^{sb}_{493}, resulting from a second-order sideband at $\nu^c_{493} - 11.744$ GHz, depopulates the $^2S_{1/2}$, $F = 0$ state. The frequency ν^h_{493}, resulting from a first-order sideband at $\nu^c_{493} - 4.300$ GHz, Doppler cools any co-trapped barium II even isotopes and sympathetically cools $^{133}Ba^+$. This first-order sideband is scanned across the blue shaded region (to $\nu^c_{493} - 3.800$ GHz) using a high bandwidth fiber EOM to Doppler heat any other barium II isotopes out of the ion trap

the 493 nm EOM. By loading with the 493 nm and 650 nm laser frequencies optimized for $^{132}Ba^+$ laser cooling, we believe improved sympathetic cooling by the large $^{132}Ba^+$ cloud improves $^{133}Ba^+$ capture. After reaching the cooling frequencies for $^{133}Ba^+$, the trap rf is

decreased to reduced the trap depth and ν^h_{493} swept to ν^c_{493} - 3.700 GHz (Fig. 4.10c). This tone is then removed and the trap depth restored. This sufficiently Doppler heats any co-trapped even isotopes, leaving $^{133}Ba^+$ or non-barium "dark" ions. To optimize the ν^h_{493} sweep bandwidth, strength, and trap depth reduction, the laser frequencies are returned to the $^{132}Ba^+$ cooling frequencies to confirm even isotope removal. Often there are enough remaining dark ions to prevent the crystallization and detection of $^{133}Ba^+$. It is still an open question as to what these species are, but we believe it is likely to be $^{133}Cs^+$. To remove these unwanted species, all four cooling frequencies are red-detuned ≈100 - 200 MHz, and a DC voltage applied to a pair of diagonally opposing trap rods for 1.0 s. Application of DC voltage is controlled in software and there is ∼ 10 ms delay between the application of voltage on each rod. The laser frequencies are then returned to the $^{133}Ba^+$ cooling values and fluorescence monitored for $^{133}Ba^+$ detection. This cycle is repeated, increasing the DC values by 50.0 mV at each step, from 2.0 V to 4.0 V. If no ions are detected, the lasers are reset to the $^{132}Ba^+$ cooling frequencies and the trap reloaded.

If $^{133}Ba^+$ ions are detected with co-trapped dark ions, the same procedure of DC voltage application is repeated until all unwanted species have been ejected from the trap. Empirically, red-detuning the cooling frequencies ≈ 100 MHz has the highest efficiency of dark ion distillation after initial $^{133}Ba^+$ fluorescence is observed. Often, $^{133}Ba^+$ ion are lost in the distillation process. If a pure chain of more than one $^{133}Ba^+$ is present, distillation to a single ion is accomplished by red-detuning the cooling frequencies so the photon count rate is reduced by half, and applying the same DC cycle previously described. Loading and distilling of a single $^{133}Ba^+$ ion typically takes 10-45 minutes, and trap lifetimes in excess of 24 hours usually require one loading attempt per day.

4.3.4 Spectroscopy

With the successful laser cooling and distillation of a single $^{133}Ba^+$ ion, the $^2S_{1/2}$, $^2P_{1/2}$, and $^2D_{3/2}$ hyperfine splittings were measured during the same day using the same atomic ion. These spectra were obtained by using the same technique described in section 4.2.1.1, where

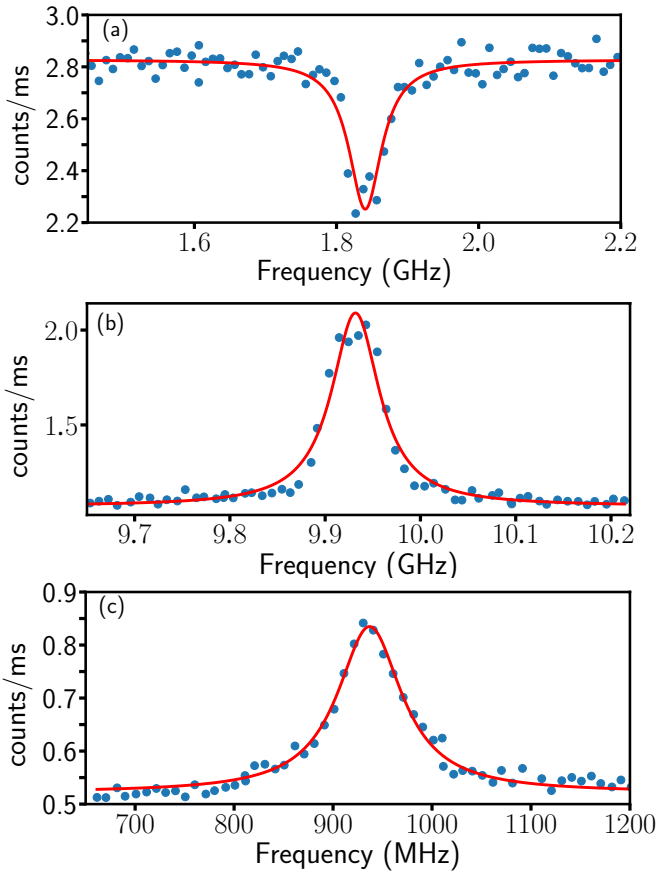

Figure 4.11: Measured hyperfine splittings of the $^2S_{1/2}$, $^2P_{1/2}$, and $^2D_{3/2}$ states in $^{133}Ba^+$. Solid red lines are fitted Lorentzian profiles. **(a)** Fluorescence as a function of applied modulation frequency to a laser tuned slightly red of the $|^2S_{1/2}; F = 1\rangle \leftrightarrow |^2P_{1/2}; F = 1\rangle$ transition. When the applied modulation frequency is near Δ_2, the ion can spontaneously decay to the $F = 2$ states in the $^2D_{3/2}$ manifold. The resulting decrease in fluorescence gives a $^2P_{1/2}$ hyperfine splitting of $\Delta_2 = 1840(2)_{\text{stat}}$ MHz. **(b)** Fluorescence from a single $^{133}Ba^+$ atomic ion with the application of laser frequencies ν^c_{493}, ν^c_{650} and ν^{sb}_{650} while scanning laser frequency ν^{sb}_{493}. The peak of the fluorescence spectrum yields the $^2S_{1/2}$ hyperfine qubit splitting $\Delta_1 = 9931(2)_{\text{stat}}$ MHz. **(c)** After applying laser frequencies ν^c_{493}, ν^{sb}_{493}, $\nu^c_{493} - \Delta_1$, and ν^c_{650}, an applied frequency near ν^{sb}_{650} is scanned to repump $^{133}Ba^+$ out of the $F = 2$ states in the $^2D_{3/2}$ manifold. The resulting increase in fluorescence rate yields a $^2D_{3/2}$ hyperfine splitting of $\Delta_2 = 937(3)_{\text{stat}}$ MHz. These measurements all have a ± 20 MHz systematic uncertainty primarily due to drift of the wavemeter used to stabilize the lasers.

rapidly alternating between cooling and a low intensity probe beam eliminates unwanted lineshape distortions (Fig. 4.3). All measurements have a ±20 MHz systematic uncertainty primarily due to drift of the wavemeter [Hig14] used to stabilize the lasers. To measure the $6^2P_{1/2}$ hyperfine splitting (Fig. 4.11a), a sideband of the laser with frequency near the $|^2P_{1/2};F{=}1\rangle \leftrightarrow |^2S_{1/2};F = 1\rangle$ transition is scanned. When this frequency is near resonance, and without laser frequency ν^{sb}_{650}, the population of the $|^2D_{3/2};F{=}\,2\rangle$ states is increased. We utilize the resulting decrease in fluorescence to measure the $6^2P_{1/2}$ hyperfine splitting $\Delta_2 = 1840(2)_{\text{stat}}$ MHz (see Fig. 4.11b). To measure the $6^2S_{1/2}$ hyperfine qubit splitting, the laser sideband ν^{sb}_{493} near the $|^2P_{1/2};F = 1\rangle \leftrightarrow |^2S_{1/2};F = 0\rangle$ transition is scanned. The fluorescence is maximized when $\nu^{sb}_{493} = \nu^{c}_{493} - \Delta_1 - \Delta_2$ (see Fig. 4.10a). We measure the hyperfine qubit splitting $\Delta_1 = 9931(2)_{\text{stat}}$ MHz. In order to measure the $^2D_{3/2}$ hyperfine splitting, we increase the population of the $|^2D_{3/2};F{=}2\rangle$ manifold by applying a laser sideband at frequency $\nu^{c}_{493} - \Delta_2$. The fluorescence is maximized when the laser sideband $\nu^{sb}_{650} = \nu^{c}_{650} + \Delta_4 - \Delta_2$ (see Fig. 4.10c). We measure $\Delta_4 = 937(3)_{\text{stat}}$ MHz.

In addition to the hyperfine splittings, efficient laser cooling requires knowledge of the $^2P_{1/2} \leftrightarrow ^2S_{1/2}$ and $^2P_{1/2} \leftrightarrow ^2D_{3/2}$ isotope shifts ($\delta\nu^{493}_{133,138}$ and $\delta\nu^{650}_{133,138}$, Eq. 4.28). By scanning the frequencies ν^{c}_{493} and ν^{c}_{650} we obtain $\delta\nu^{493}_{133,138} = 355(4)_{\text{stat}}$ MHz and $\delta\nu^{650}_{133,138} = 198(4)_{\text{stat}}$ MHz.

With the lower lambda system spectroscopy known, we move to the spectroscopy needed for electron shelving. High fidelity shelving of the $|^2S_{1/2};F = 1,m_F = 0\rangle$ state can be achieved with optical pumping by application of the frequencies ν_{455}, ν_{585}, and ν^{c}_{650} (and ν_{614} for deshelving), see Figure 6.2. To determine these unknown frequencies, we measure the $^2P_{3/2} \leftrightarrow {}^2S_{1/2}$ and $^2P_{3/2} \leftrightarrow {}^2D_{5/2}$ isotope shifts relative to $^{138}Ba^+$ ($\delta\nu^{455}_{133,138}$ and $\delta\nu^{614}_{133,138}$) and hyperfine splittings Δ_3 and Δ_5.

To measure Δ_3 and $\delta\nu^{455}_{133,138}$, the atom is prepared in the $|^2S_{1/2};F = 1\rangle$ manifold by optical pumping with ν^{c}_{650} and ν^{sb}_{650} after Doppler cooling. A laser near 455 nm (ν_{455}) is applied for 50 μs with saturation parameter $s \approx 1 \times 10^{-3}$. When the frequency is near one of the two allowed transitions, excitation followed by spontaneous emission from the $^2P_{3/2}$

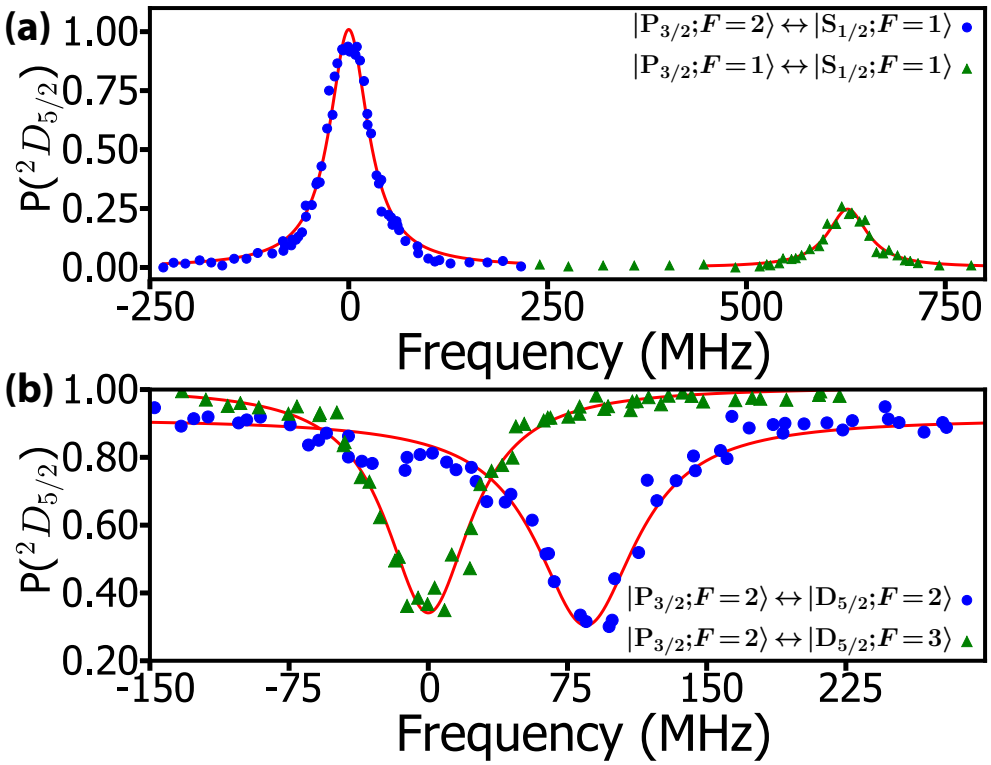

Figure 4.12: (a) Measurement of the $^2\mathrm{P}_{3/2}$ hyperfine splitting by tuning the 455 nm laser. The left (right) peak corresponds to $F = 2$ ($F = 1$) in $^2\mathrm{P}_{3/2}$. (b) Measurement of the $^2\mathrm{D}_{5/2}$ hyperfine splitting by tuning the 614 nm laser. Triangles are data for the $|^2\mathrm{P}_{3/2};F=2\rangle \leftrightarrow |^2\mathrm{D}_{5/2};F=3\rangle$ transition, circles are for the $|^2\mathrm{P}_{3/2};F=2\rangle \leftrightarrow |^2\mathrm{D}_{5/2};F=2\rangle$ transition. Solid lines are Lorentzian fits. Statistical error bars on individual data points are smaller than markers.

with branching ratios [DDY16] 0.74, 0.23, and 0.03 to the $^2\mathrm{S}_{1/2}$, $^2\mathrm{D}_{5/2}$, and $^2\mathrm{D}_{3/2}$ states, respectively, optically pumps the ion to the $^2\mathrm{D}_{5/2}$ state. The population remaining in the $^2\mathrm{S}_{1/2}$ and $^2\mathrm{D}_{3/2}$ states is then detected by collecting fluorescence while Doppler cooling and using threshold discrimination on the number of collected photons to decide if the atom was in the $^2\mathrm{D}_{5/2}$ state. This sequence (Fig. 4.13a) is repeated 200 times per laser frequency, and the average population is shown in Fig. 4.12(a) as a function of frequency. All lasers are linearly polarized $\approx 45°$ from the magnetic field direction. From these data, we find $\Delta_3 = 623(20)$ MHz, and $\delta\nu^{455}_{133,138} = +358(28)$ MHz relative to $^{138}\mathrm{Ba}^+$.

To measure Δ_5 and $\delta\nu^{614}_{133,138}$, the atom is Doppler cooled and shelved to the $^2\mathrm{D}_{5/2}$ state

via one of the $^2P_{3/2}$ hyperfine manifolds. The $|^2D_{5/2};F{=}2\rangle$ manifold is prepared via shelving on the $|^2P_{3/2};F=1\rangle \leftrightarrow |^2S_{1/2};F=1\rangle$ transition, as dipole selection rules forbid decay to the $|^2D_{5/2};F{=}3\rangle$ state. Similarly, the $|^2D_{5/2};F=3\rangle$ manifold is prepared by shelving on the $|^2P_{3/2};F=2\rangle \leftrightarrow |^2S_{1/2},F=1\rangle$ transition, where 0.93 of decays to the $^2D_{5/2}$ are to the $|^2D_{5/2};F{=}3\rangle$ manifold. Next, a tunable laser near 614 nm is applied for 100 μs with saturation parameter $s \approx 1$. When the frequency is near the $|^2P_{3/2};F{=}2\rangle \leftrightarrow |^2D_{5/2};F{=}3\rangle$ or $|^2P_{3/2};F{=}2\rangle \leftrightarrow |^2D_{5/2};F{=}2\rangle$ transition, spontaneous emission from the $^2P_{3/2}$ state quickly deshelves the ion to the $|^2S_{1/2};F{=}1\rangle$ and $^2D_{3/2}$ states. This deshelved population is then detected via Doppler cooling. All lasers are linearly polarized $\approx 45°$ from the magnetic field direction. This sequence (Fig. 4.13b) is repeated 200 times per laser frequency, and the average population is shown Fig. 4.12(b) as a function of frequency. From these data, we find the $^2D_{5/2}$ hyperfine splitting $\Delta_5 = 83(20)$ MHz, and isotope shift $\delta\nu^{614}_{133,138} = +216(28)$ MHz. Reported hyperfine measurements (Table 4.5) include a systematic uncertainty of 20 MHz due to unresolved Zeeman structure. For isotope shifts, the relevant $^{133}Ba^+$ centroid frequency is determined from the hyperfine splitting measurements and then compared to measurements of the corresponding $^{138}Ba^+$ transition. Reported isotope shifts include a 28 MHz systematic uncertainty due to wavemeter drift and unresolved Zeeman structure.

The $^{133}Ba^+$ spectroscopy measured in this work and elsewhere is summarized in Table 4.5.

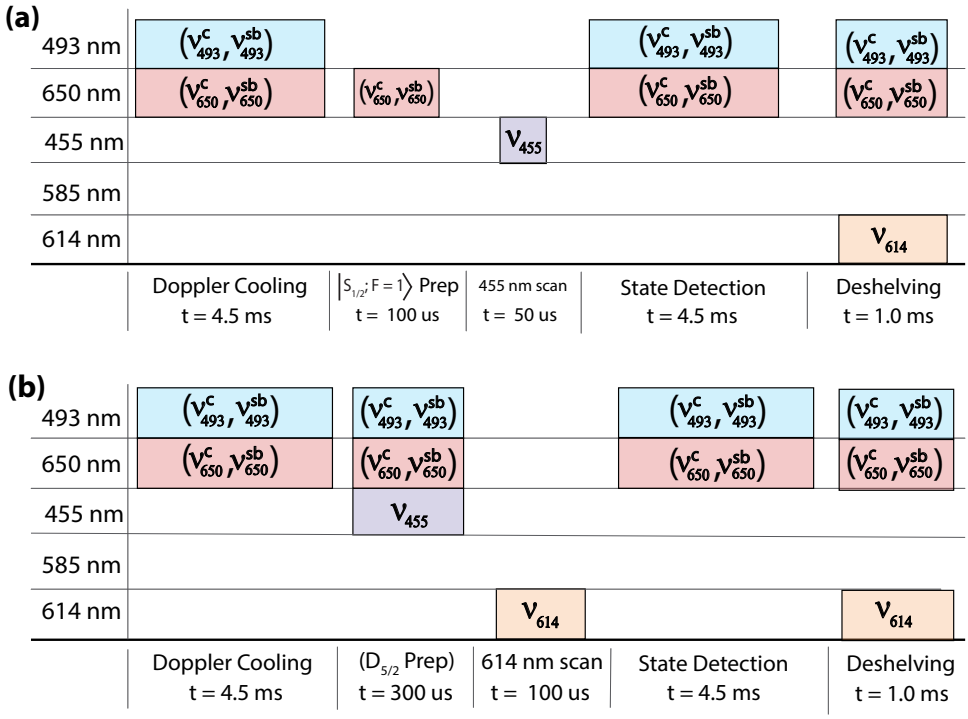

Figure 4.13: (a) Sequence for measuring $^2\mathrm{P}_{3/2}$ hyperfine splitting and $^2\mathrm{P}_{3/2} \leftrightarrow {}^2\mathrm{S}_{1/2}$ isotope shift. All lasers are linearly polarized $\approx 45°$ from the magnetic field direction, and ν_{455} has saturation parameter of $s \approx 1 \times 10^{-3}$. (b) Sequence for measuring $^2\mathrm{D}_{5/2}$ hyperfine splitting and $^2\mathrm{P}_{3/2} \leftrightarrow {}^2\mathrm{D}_{5/2}$ isotope shift. All lasers are linearly polarized $\approx 45°$ from the magnetic field direction, and ν_{614} has saturation parameter of $s \approx 1$.

Hyperfine Splitting	Frequency (MHz)
$^2S_{1/2}$	9925.45355459(10)
$^2P_{1/2}$	1810(11)
$^2P_{3/2}$	**623(20)**
$^2D_{3/2}$	**937(20)**
$^2D_{5/2}$	**83(20)**
Isotope Shift	**Frequency (MHz)**
$\delta\nu^{493}$	373(4)
$\delta\nu^{455}$	**358(28)**
$\delta\nu^{650}$	**198(20)**
$\delta\nu^{614}$	**216(28)**
$\delta\nu^{585}$	183(35)

Table 4.5: $^{133}Ba^+$ hyperfine splittings and isotope shifts relative to $^{138}Ba^+$. For reported isotope shifts of the i-th electronic transition, defined as $\delta\nu^i \equiv \nu^i_{133} - \nu^i_{138}$, centroid frequencies ($\nu^i_{133}$) are calculated from hyperfine measurements and compared to corresponding transitions in $^{138}Ba^+$. Bolded values are measurements from this work. $\delta\nu^{585}$ is calculated using previous measurements and results from this work. Hyperfine splittings include a 20 MHz systematic uncertainty due to unresolved Zeeman structure. Isotope shifts include a 28 MHz systematic uncertainty due to unresolved Zeeman structure and wavemeter drift.

CHAPTER 5

The Experiment

"*I can wire anything directly into anything! I'm the professor!*" - Professor Hubert J. Farnsworth

The initial goals of the $^{133}Ba^{+}$ experiment at UCLA were: (1) demonstrate efficient loading from a low activity source requiring minimal shielding and safety precautions, (2) measure the unknown spectroscopy required for laser cooling and basic qubit manipulations. The initial RF Paul trap design as well as accompanying hardware were chosen with those goals in mind, building on previous work with $^{133}Ba^{+}$ and existing hardware present in the Hudson and Campbell groups at UCLA.

The first spectroscopy of $^{133}Ba^{+}$ was accomplished by loading ions into an RF Paul trap via thermionic emission [KSW87]. When referring to ions, thermionic emission is the production of ions desorbing from the surface of a hot metal whose work function is higher than the neutral-state ionization energy. Effectively, it cost less energy to leave an atom's valence electron on the metal surface if the atom's ionization energy is less than the metal's work function. In the previous work, a platinum filament impregnated with $^{133}Ba^{+}$ was placed inside the RF trapping volume and heated to 1200°C for a few seconds, producing approximately 10^5 trapped $^{133}Ba^{+}$ ions. A major effort was undertaken during the first two years of the experiment to produce a viable thermionic source of $^{133}Ba^{+}$ and load an RF Paul trap in the same way. During that time, successful loading of an ion trap with $^{138}Ba^{+}$ was achieved by heating a platinum filament impregnated with naturally abundant barium, and ion production of many species used in trapped-ion quantum information (Mg^{+}, Ca^{+}, Sr^{+}, Ba^{+},

and Yb^+) was demonstrated. Although in the end this did not lead to our method for loading $^{133}Ba^+$, a great deal of information was learned about the practical uses of a thermionic source. In fact, as described below we currently produce ions via laser ablation of a platinum filament originally intended for thermionic emission loading. A detailed description of our efforts to produce a $^{133}Ba^+$ source utilizing the effect, and the equation describing thermionic emission is given in Appendix D.

5.1 Vacuum Chamber

The vacuum system is shown in Figure 5.1 with the major components labeled. A 34 L/s

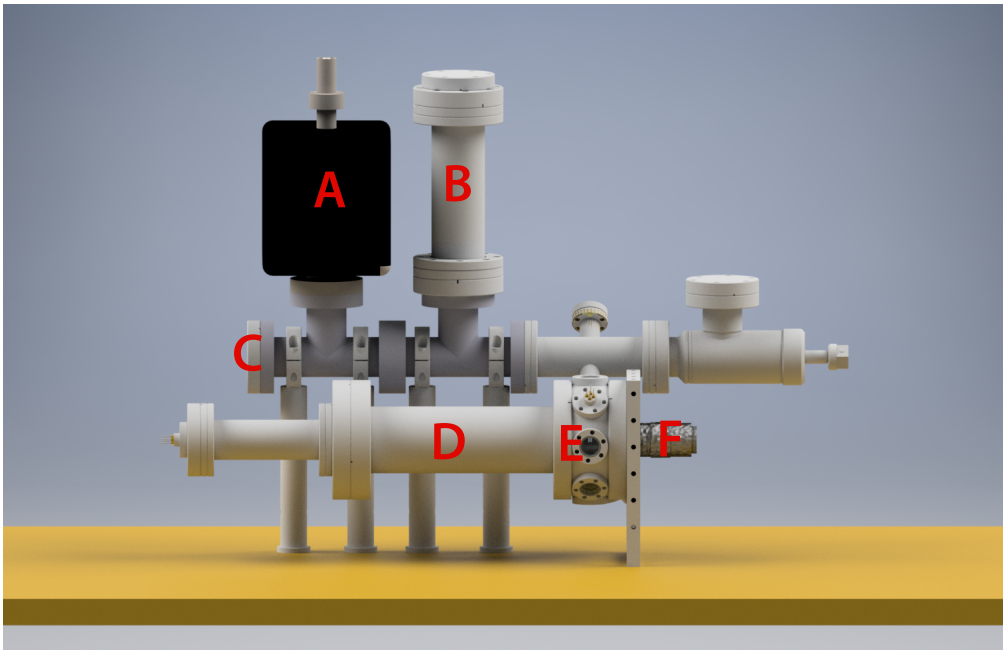

Figure 5.1: Vacuum system with major components labeled. (A) ion pump, (B) titanium sublimation pump, (C) ion gauge, (D), time of flight mass spectrometer (TOF), (E) 4.5" spherical octagon with RF Paul trap, (F) 0.28 NA Mitutoyu apochromatic objective.

ion pump (A), 3-filament titanium sublimation pump (B), and nude ion gauge (C) manage and monitor pressure inside the chamber. A 4.5" spherical octagon (E) houses an RF Paul trap and multiple atomic-ion sources. A time of flight mass spectrometer (TOF) is used to detect any trapped atomic or molecular-ion species (D), and a 0.28 numerical aperture (NA)

apochromatic objective (F) collects spontaneously emitted atomic fluorescence. Specific part descriptions and numbers can be found in Table 5.1, except for the TOF which is described in more detail below.

Description	Vendor	Part Number
Agilent 34 L/s ion pump	Ideal Vacuum	9191240
Agilent ion pump controller	Ideal Vacuum	9299010
Agilent ion pump cable	Ideal Vacuum	9290705
UHV nude ion gauge	Duniway	I-NUDE-F
XGS-600 ion gauge cable	Ideal Vacuum	P104127
3-Filament Ti-sub cartridge	Duniway	TSP-275-003
Ti-sub cable	Duniway	TSP-275-003
Ti-sub controller	Duniway	922-0043
4.5" spherical octagon	Kimball Physics	53-180000
2.69" fused silica viewport	MPFPI	A0650-4-CF
10X Mitutoyo Plan APO obj.	Edumunds Optics	46-144

Table 5.1: Main component parts used in the vacuum system in Figure 5.1.

In any trapped-ion quantum information experiment, isolating ions from the environment is necessary to reduce decoherence effects. Unwanted chemistry, heating, delocalization, and ejection from the trap can result from collisions between trapped atomic ions and background gas particles. Therefore, great care is taken to reduce the background gas pressure inside the vacuum chamber.

While a great deal of literature is available on the subject, we utilized group members previous experience for vacuum chamber cleaning and baking protocols. Any steel parts purchased from a commercial vacuum components company were cleaned in two stages. First, a minimally two hour ultrasonic cleaner bath in acetone, followed by a minimum one hour ultrasonic cleaner bath in methonal. For parts machined at UCLA, an initial ultrasonic

cleaning in both an Alconox and Citrinox were performed to remove any oils, followed by the acetone and methonal steps. All tools used for assembling components inside the chamber received the same cleaning treatment, and Latex gloves were worn at all times and changed regularly.

Despite the most rigorous cleaning protocols, exposure to atmosphere leads to deposition of contaminants on the inside of the vacuum chamber. In addition, hydrogen in the bulk of steel parts will diffuse out under vacuum adding to the gas load. Heating the chamber under vacuum can reduce pressures by orders of magnitude and is common practice, however, many glass to metal seals are only rated up to 200°C, limiting the minimum achievable pressures when heating an entire chamber. Improved vacuum can be achieved by pre-treating components that can tolerate higher temperatures. Baking parts up to 1000°C for two hours reduces hydrogen in bulk steel, and baking at $\sim$ 400°C in air can provide a surface oxide layer limiting hydrogen diffusion under vacuum [cer]. In this experiment neither option was available, and a standard 200°C bake of the whole vacuum system was performed. With only the turbo pump turned on, the chamber was raised from room temperature to $\approx$ 190°C at a rate of 1°C/2 min by wrapping then entire chamber in aluminum foil, followed by heater tape, followed by aluminum foil again. Thermocouples placed at various locations monitored the temperature and individual control of heater tapes prevented large thermal gradients. The pressure increased for approximately 3 days before leveling off, after which degassing of the ion gauge was performed. After degassing, the ion pump was activated and angle value closed (hand tightened) after no further decrease in observed pressure. The temperature was reduced at the same rate of 1°C/2 min, plotted in Figure 5.2 versus pressure, continually tightening the angle valve throughout. Finally, after reaching room temperature the titanium sublimation pump (Ti-sub) was activated by running 30 A of current through the filaments for two minutes. An increase in pressure by one order of magnitude was initially observed, decreasing after 24 hours below the initial value. The Ti-sub was fired once a day for approximately one week, with the ion gauge reporting a final pressure of 3×10^{-10} Torr. The chamber was opened various times after the initial bake to replace atomic-ion sources, and

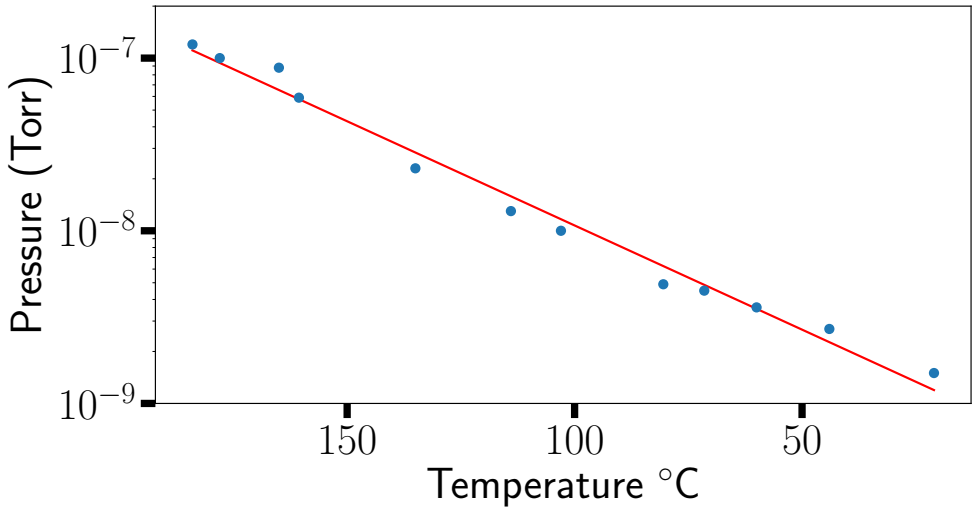

Figure 5.2: Temperature *vs.* pressure during a cool down after baking the vacuum chamber to 200°C. Red line is fit to straight line.

a nitrogen backfill was used to reduce contamination by atmosphere.

With the minimum pressure reached the rate at which a trapped ion collides with background gas particles can be estimated. The collision rate is often modeled using Langevin capture theory, which describes the ion induced-dipole coupling between a charged particle and polarizable neutral atom or molecule. The rate constant, which is the reaction rate divided by the background gas density is given by (derivation given in Appendix C):

$$\Gamma = \left(\frac{\pi\alpha e^2}{2\epsilon_0^2\mu}\right)^{1/2} \tag{5.1}$$

where α is the neutral polarizability, e the electron charge, ϵ_0 permitivity of free space, and μ the reduced mass of the ion-neutral pair. Using the ideal gas law to estimate the density inside the vacuum chamber, and assuming a background gas of H_2 ($\frac{\alpha}{4\pi\epsilon_0} \approx 1 \times 10^{-30}\text{m}^3$), a collision is expected approximately every minute. Experimental observations are closer to every ten minutes, and the majority do not seem to cause the ion to leave the trap. Average ion lifetimes are approximately one day with the longest observed 46 hours.

5.2 RF Trap

The 4-rod RF Paul trap used in this experiment is shown in Figure 2.2. In an attempt to increase the region where the trapping potential is purely harmonic, the inner surfaces of the trap rods were made semi-hyperbolic. The shortest distance between opposing trap rods is 6 mm ($r_0 = 3$ mm) with 15 mm between the cylindrical endcaps. Hollow endcaps were used to allow laser access along the axial direction of the trap. The rods were machined using a wire EDM, which cut all four inner surfaces from a single piece of steel before separating them electrically. Macor endcaps hold and keep the rods and endcaps electrically separated inside the trap (Fig. 5.3).

Two diagonally opposing rods are driven at an RF frequency of $\Omega_{\text{rf}} = 2\pi \times 1.0$ MHz, while the other two are held at RF ground. All four rods and two endcaps can be independently DC biased. Use of the TOF requires all four trap rods be quickly, and independently biased with large DC voltages to eject ions radially from the trap (Fig. 5.10). It is also necessary to immediately remove the RF voltage before ejection. In order to meet these requirements, custom electronics were designed by the Hudson group at UCLA [SSY16], in which all four trap rods could be individually driven with RF and DC voltages. Nearly identical resonant circuits are built to drive each trap rod, and initial setup requires hand tuning each circuit via a small capacitor to match resonant frequencies. A custom circuit board at the chamber feedthrough mates the the wires from a 2- or 4-pin feedthrough to the coaxial cables coming from the RF amplifier circuits. A small trace on the circuit board near the RF connectors acts as a capacitive pickoff and allows for direct monitoring of the RF trap voltages. Before closing the vacuum chamber, an applied voltage on each trap rod and corresponding pickoff were measured on an oscilloscope for calibration. Although the scope probe changes the trap-amplifier circuit resonance, the ratio of voltages is not significantly affected.

A consequence of near but not identical resonance frequencies, as well as a small coupling between resonant circuits housed in the same electronics box, is an offset in amplitude and phase between each RF rod. To account for this, pickoff voltages from each rod are measured on an oscilloscope and one RF-drive DDS adjusted until the two amplitudes and

phases are as close as possible. As noted in chapter 2, a difference in phase causes excess micromotion, increasing the average energy of the ions. The minimum programmable phase shift of 0.22 degrees, defined by the trap drive DDS, limits lowest achievable temperature in this configuration. Eventually, the TOF was no longer needed and the trap rods were shorted with a high-voltage capacitor at the feedthrough. A 20% increase in atomic fluorescence was observed indicating lower temperatures and narrower atomic linewidths.

5.3 Ion Sources & Ablation Loading

5.3.1 Naturally Abundant $BaCl_2$ Target

Before any work with $^{133}Ba^+$ was attempted, loading naturally abundant atomic barium ions was performed to calibrate all experimental parameters. The first source, hereafter referred to as the "natural target", was produced by compressing $BaCl_2$ powder into a small ceramic boat and firing at ~ 1000 °C for one hour to remove excess water. The boat was placed near the bottom of the spherical octagon and held in place by copper feedthrough wires not in use, labeled (C) in Figure 5.3. Line-of-sight access is available through the main viewport where atomic fluorescence is collected (Fig. 5.1). A Minilight [min] 1064 nm YAG laser doubled to 532 nm delivers 3-5 ns laser pulses with up to 12 mJ of energy at the natural target. Using a recently purchased gentec QE25LP-S-MB-D0 energy meter, an average measured ablation energy of ≈ 500 μJ ($w_0 \sim 250$ μm) loads ions from the natural source. Mechanical and thermal drifts cause significant variations in 1064 nm doubling efficiency, resulting in large shot to shot loading fluctuations. In addition, repeated ablation from the same location on the natural target (~ 100 shots) leads to an eventual decrease or cessation of loading. Similar observations are seen in other groups at UCLA, and small changes in the ablation spot alleviate the problem.

In our configuration, ablation produces barium ions outside of the trapping volume. In the approximation of a conservative harmonic trapping potential, any ion with enough energy to overcome the potential barrier into the trapping region cannot remain trapped

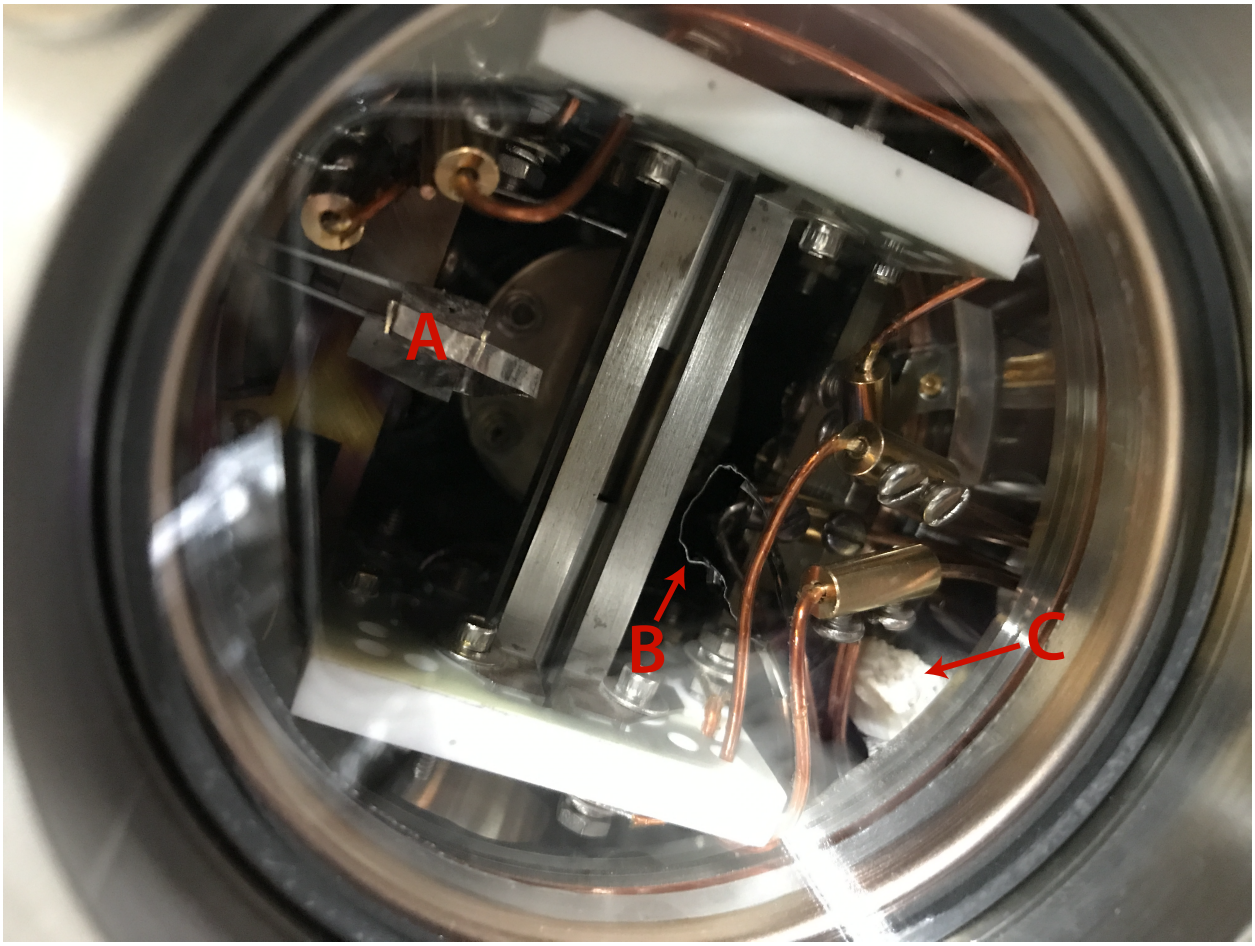

Figure 5.3: Image looking through the main viewport of the vacuum chamber. The four-rod ion trap at the center is held in place by two Macor endcaps. Behind the trap half of the TOF is visible. Atomic-ion sources are labeled as (A) radioactive filament, (B) naturally abundant platinum filament, (C) $BaCl_2$ with naturally abundant barium.

without dissipation. While laser cooling can provide a dissipative force, interaction times are typically too short to efficiently load ions. To overcome this, a "trap door" scheme is implemented by removing the trap RF voltage during the ablation pulse (see Figure 5.4). When the trap electronics microcontroller receives an ablation pulse request via software, the trap RF terminates and a TTL sent to the q-switch after an appropriate time, firing the laser. The trap RF is restored after a user specified amount of time, and the low energy tail of the ablated ions captured. We observe loading of ions restoring the trap RF between 50 μs and 120 μs after ablating the natural target, with a maximum efficiency at 70 μs.

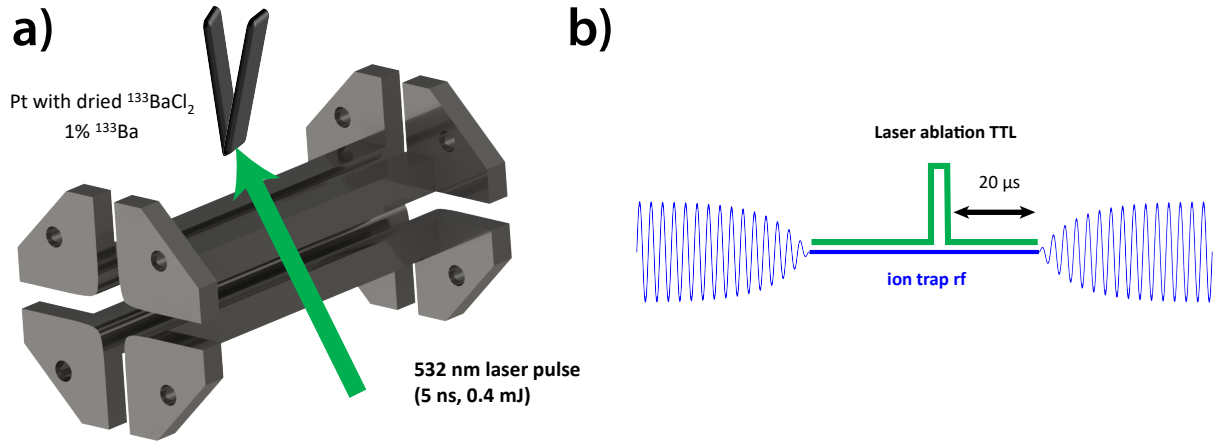

Figure 5.4: Trap door loading scheme used to load ions via laser ablation. Ions produced outside of the trapping volume encountering the conservative potential will either be rejected away from the trapping region or completely pass through. (a) Image of trap and radioactive filament. (b) By removing the RF voltage before ablation, the low energy tail of the ablated ion velocity distribution can be captured by reestablishing the RF voltage after an optimized time delay, 20 μs for the geometry of the radioactive filament.

5.3.2 Thermionic Sources

With the goal of producing $^{133}Ba^+$ via thermionic emission, a naturally abundant thermionic source was constructed to demonstrate the technique and optimize loading parameters. Details on the construction, barium impregnation, and ion production can be found in Appendix D. Briefly, a $BaCl_2$ salt is deposited on the surface of a platinum[1] filament with approximate dimensions 1 mm $\times$ 10 mm $\times$ 0.1 mm. A current of 12-20 amps heats the filament to $\sim$ 1000 K (orange-white in color) for approximately one minute resulting in the impregnation of barium ions, and after the surface lightly cleaned to removed any remaining bulk salt. The filament is then attached to copper wires of a vacuum feedthrough and placed near the radial opening of the ion trap, labeled (B) in Figure 5.3.

$^{138}Ba^+$ ions were successfully loaded with approximately half the current used for impreg-

[1]Platinum has a work function of $\approx$ 6 eV, while Ba has an ionization energy of 5.2 eV.

nation[2]. Without dropping or shuttering the trap RF, ions load immediately after heating. Although the loading mechanism is not fully understood, we believe ion-ion interactions inside the trapping volume lead to capture. Potassium, and to a lesser extent sodium, are present in bulk platinum and desorb as ions, becoming co-trapped with barium. Fortunately, these are easily removed by tuning the Mathieu a and q parameters (Eq. 2.16 and Fig. 2.5) such that only barium ions are stable. Due to the construction and placement of the filament, the largely uncollimated ion flux charges nearby insulators. An ion gun [EZ82] was constructed to move the filament farther from the trapping region while maintaining large ion fluxes at the trapping region. Although never implemented into the experiment, details about the design as well as initial results are provided in Appendix D.

Success with the natural filament led to the construction of a radioactive source with two significant alterations: (1) after deposition of $BaCl_2$ salt the filament was not heated, (2) no excess salt was removed from the surface before installation in the vacuum chamber. With a limited source quantity, and no measure of the barium impregnation into the bulk during heating, the decision was made to keep as much ^{133}Ba on the filament as possible. As a result, bulk salt was visible on the exterior of the filament after installation into the vacuum chamber. Thermionic emission relies on a relatively clean metal surface since contaminants can drastically alter work functions. We believed after enough heating, patches of platinum would be exposed and allow for thermionic emission to take place. An exhaustive effort was made to load $^{133}Ba^+$ ions by heating the radioactive platinum filament without success. Some data suggests a small amount of $^{132}Ba^+$ was loaded, but we were not able to confirm this. It is likely bulk salt on the surface prevented appreciable thermionic emission from occurring.

The decision was made to try and clean the filament surface in vacuo via ablation, while simultaneously trying to load ions using the trap door scheme. Loading large clouds of $^{132}Ba^+$ with virtually no other isotopes confirmed trapped ions produced from the radioactive

[2]Impregnation was performed in air where convection assists in removing heat.

filament[3], leading to the loading and laser cooling of $^{133}Ba^{+}$. Ablation loading from the radioactive filament is now the preferred loading technique, and no appreciable reduction in the source has been observed after $\sim 10,000$ loading attempts. We estimate that a 10 μCi source, an exempt quantity of radioactive material[4], should be sufficient for typical ion trapping experiments loading via laser ablation. As shown in Figure 5.5, only a small region of the radioactive filament is regularly ablated, and we estimate at least three times as much surface area without current laser access is available for loading.

5.4 Lasers

Both commercial and home built lasers provide the frequencies necessary for laser cooling and high fidelity qubit operations. Figure 5.6 shows the general optical setup for delivering light to the experiment. Approximately 100 μW of each laser is sent via telecom optical fiber to the Hudson lab in the adjoining building, where a High-Finesse WSU-2 wavemeter measures the each frequency with 2 MHz resolution [Hig14]. Each laser is stabilized via a software lock with feedback bandwidth much larger than the WSU-2's measurement time. Single mode fibers deliver the remaining light from an optical table housing all lasers to the experiment.

5.4.1 493 nm & 650 nm

Two external cavity diode lasers (ECDLs) (Toptica DL Pros) provide frequencies near 493 nm and 650 nm with 18 mW and 25 mW of power after the optical isolators. Before coupling into an optical fiber to be sent to the experiment, each laser is fiber coupled into a fiber-in fiber-out electro optic modulator (EOM) purchased from ADVR [adv]. These high bandwidth (6 GHz) phase modulators are used to supply the necessary tones for laser cooling,

[3]Barium-133 is manufactured by first producing and enriched source of barium-132, followed by neutron bombardment for activation.

[4]An exempt quantity requires no dosimetry or radiation shielding.

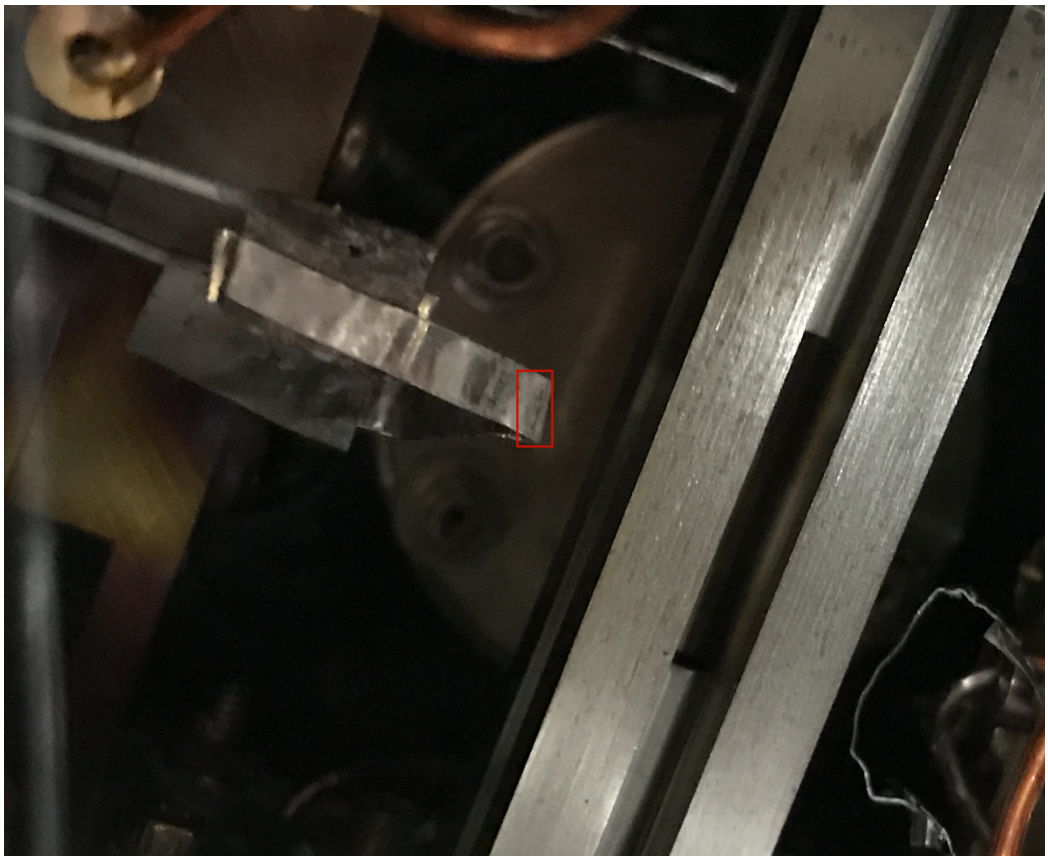

Figure 5.5: Zoomed in image of the ion trap and radioactive filament. Region enclosed by red box indicates the ablation area. No reduction in source material has been observed via loading of ions after $\sim 10,000$ ablation attempts.

isotope distilling, and qubit operations via generation of first- and second-order sidebands. After EOM and fiber-to-fiber coupling, ≈ 1 mW of power at 493 nm and ≈ 3 mW of power at 650 nm are delivered to the experiment. Each laser passes through an acusto optical modulator (AOM) where the first-order deflected beam allows for rapid shuttering of light at the ion. First-order AOM beams with approximately 20 μW of 493 nm light ($w_0 \approx 25$ μm) and 2 mW of 650 nm ($w_0 \approx 250$ μm) light cool the ion during normal operation.

For loading, the 493 nm zeroth-order beam ($w_0 \approx 250$ μm) and 650 nm first-order AOM beam are directed into the trap both radially and axially as shown in Figure 5.7. This is intended to fill the entire trapping region with cooling light and capture ions loaded far from

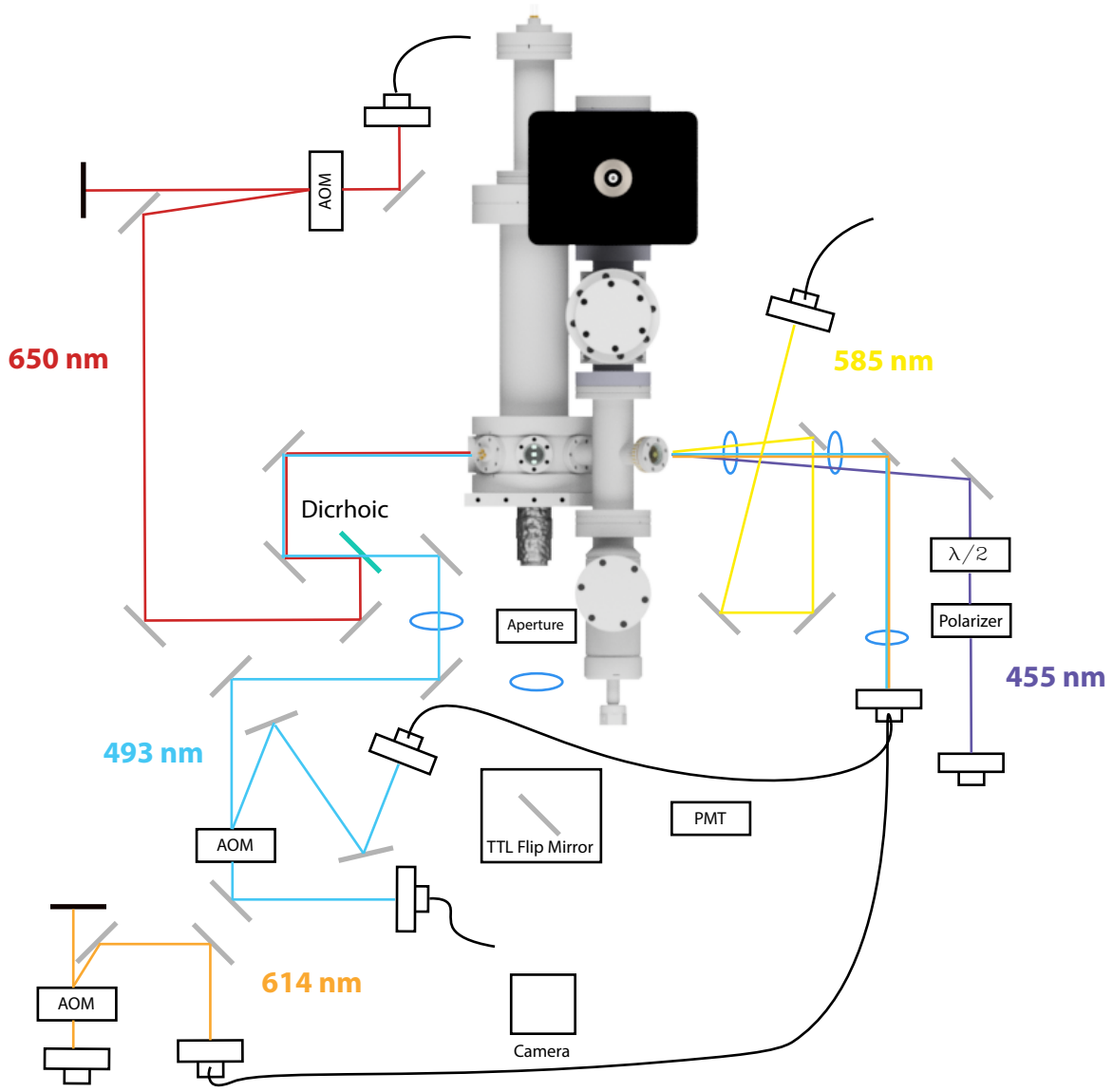

Figure 5.6: Optical layout of the experiment. The 493 nm zeroth order AOM beam and 650 nm first-order AOM beam are combined on a dichroic (green) and used for initial loading and cooling. After, the 493 nm first-order AOM beam is used to cool and run experiments. 455 nm passes through a Wallaston polarizer and half-wave plate to optimize π-light (B-field out of page) for high-fidelity shelving. A fiber combiner adds a 614 nm first-order AOM beam to the 493 nm first-order beam. 455 nm and 585 nm pass through AOMs before fiber-coupling to the experiment.

the trap center. After loading and distillation, the axial beam is removed via flip mirror, the 493 nm carrier frequency red-detuned 125 MHz, and the ion illuminated with the 493 nm first-order AOM beam. A computer controlled mechanical shutter then blocks the zeroth-

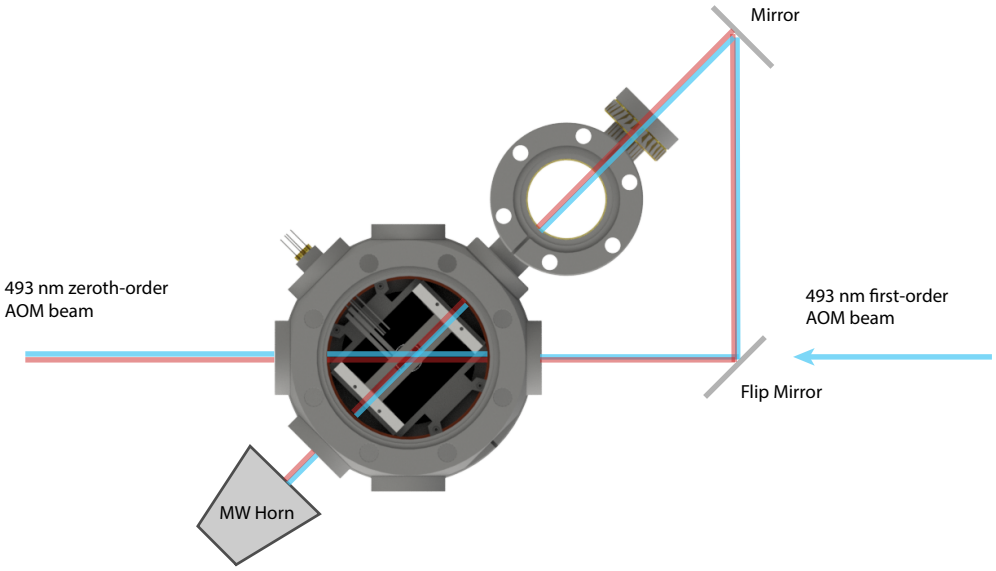

Figure 5.7: 493 nm and 650 nm beam path when loading ions. Initially, 493 nm zeroth-order AOM beam and 650 nm first-order AOM beam are directed both radially and axially through the trap via a flip mirror. After loading and distillation, the flip mirror is removed, 493 nm zeroth order beam blocked, and the 493 nm first-order AOM beam directed into the trap counter propogating to the 650 nm beam.

order beam until PMT counts below a user defined level during any point of the experiment causes it to open. This red-detuned "protection beam" has empirically shown a large success rate for recapturing ions.

5.4.2 455 nm, 585 nm, 614 nm

High fidelity electron shelving via optical pumping requires frequencies near 455 nm, 585 nm, and 614 nm (for deshelving). All three are ECDLs were built at UCLA and based on an in-house design shown in Figure 5.8[5].

A single-mode diode near 455 nm provides light to drive the $^2P_{3/2} \leftrightarrow ^2S_{1/2}$ transition (Fig. 6.2) for the required electron shelving. To prevent errors during high-fidelity experiments, 455 nm light must be extinguished to extremely low levels during the non-shelving portions

[5]CAD files can be obtained by contacting current group members.

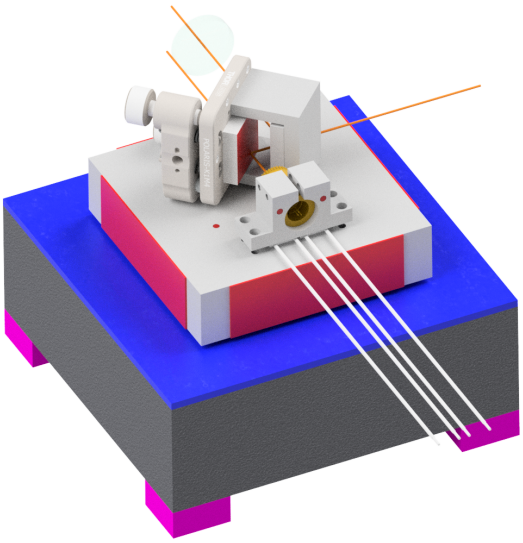

Figure 5.8: ECDL design for the 455 nm, 585 nm, and 614 nm lasers. White lines represent incoming wires for the diode and thermistor.

of the experiment. An RF switch at the input of the 455 nm AOM amplifier was required to extinguish RF pickup from nearby noise sources. In addition, light at the ion from AOM crystal scatter was reduced with an improved incident spatial mode (short fiber patch cable) at the AOM optical input with the minimum incident power required for high-fidelity shelving. Finally, the first-order AOM beam was spatially filtered with a 100 μm pinhole before coupling to the single-mode fiber carrying light to the experiment. With this setup, an ion would remain in the lower lambda system cooling cycle for approximately 20 minutes before a stray 455 nm photon would accidentally shelve it to the $^2D_{5/2}$ state.

To our knowledge, single-mode diodes at 585 nm are not available. While many solutions exist using frequency sum or difference generation, second harmonic generation (SHG) waveguides offer a relatively simple setup and minimal hardware to operate. ADVR Inc. manufactures periodically poled lithium niobate (PPLN) waveguides with fiber-in fiber-out coupling and efficiencies of $\approx 100\%/\text{W}$. Among other diode options, Innolume gain chips with 200 mW output powers and gain mediums covering 1171 nm were available as doubling sources. A gain chip is essentially a laser diode where the front facet has $\approx 100\%$ transmission. This effectively eliminates the internal cavity of the diode and allows for extremely

large tuning bandwidths (80 nm for our gain chip). Gain chips work in standard ECDL configurations and our in-house design was use to construct the laser. Finding the correct set of parameters for single-mode operation proved formidable after initial construction. An extremely oblate spatial mode exiting the gain chip resulted in clipping of the steering mirror used to cancel first order beam pointing changes with diffraction grating tuning. The resulting feedback prevented single-mode operation and a simple modification alleviated the problem. Maximizing the SHG requires temperature tuning the PPLN waveguide, optimized at 27.4 °C, producing ≈ 80 μW of 585 nm light. A first-order deflected beam from an AOM coupled into single-mode fiber delivers ≈ 20 μW of power to the experiment. A few microwatts and beam waist $w_0 \approx 50$ μm is used for typical shelving operations.

614 nm single-mode direct diodes are also not available as far as we know. With the success of the 585 nm laser, an identical system was built using a 1228 nm Innolume gain chip and PPLN waveguide optimized to double the longer wavelength. The $^2D_{5/2}$ state isotope shift and hyperfine splitting in $^{133}Ba^+$ (Fig. 6.2) is small enough to allow deshelving with the laser tuned the $^2D_{5/2} \leftrightarrow {}^2P_{3/2}$ resonant transition in $^{138}Ba^+$, allowing multiple experiments to use the same laser without carrier shifts or AOM double pass configurations. The detuning of ≈ 50 MHz from either $^{133}Ba^+$ hyperfine manifold requires ≈ 500 μs to fully deshelve the ion given the ≈ 2 μW ($w_0 \approx 50$ μm) of power delivered to the experiment.

5.4.3 RF & Microwaves

RF and microwaves are required to drive AOMs, add frequency sidebands to lasers, and directly manipulate the ground state hyperfine qubit. Decades of well established microwave and RF technology make finding cheap stable oscillators and amplifiers relatively easy, with used devices available on various internet sites. Utilizing these resources[6], Table 5.2 lists major devices used in the lab along with the frequency they generate.

Often, frequency sources output small amplitudes in the "off" state and cannot turn on

[6]Two great resources can be found at `http://westerntestsystems.com/` and `https://www.dudleylab.com/`

Description	Device	Manufacturer	Part Number	Frequency (MHz)
Qubit manipulations	Oscillator	Hewlitt Packard	HP8672A	9925
State preparation	Oscillator	Hewlitt Packard	HP8673B	1810
493 nm repumper	VCO	MiniCircuits	-	5872
650 nm repumper	Oscillator	Hewlitt Packard	HP8673B	904
TWT (20 Watt)	Amplifier	Varian	SN-6256	-
AOM RF Drive	Oscillator	RF-Consultant	TPI-1002-A	40-4000
Fast RF Switching	RF switch	MiniCircuits	ZASWA-2-50DRA+	DC-6000
Custom DDS board	DDS	UCLA	AD9915	60-1000

Table 5.2: Parts list and application for major RF and microwave equipment used in the experiment.

and off quickly. As a result, fast switching (20 ns) solid state devices with greater than 65 dB suppression are used on all RF and microwave frequency sources. Manipulating the ground state hyperfine qubit requires microwaves at $\approx$ 9.925 GHz generated with a quarter-wave antenna and focused with a microwave horn. The horn is directed along the axial direction of the trap (Fig. 5.7) and microwave output shuttered with a solid state pin diode switch purchased from eBay (no part number or manufacturer markings visible). Despite directional gain from the horn, long wavelength microwaves and large horn size (approximately 3" $\times$ 1" $\times$ opening and 4" length) make generating high amplitude fields at the trap center difficult. High power amplifiers can alleviate the problem, and new or used traveling wave tube (TWT) amplifiers have provided the necessary amplification to achieve $\approx$ 70 kHz hyperfine qubit Rabi frequencies.

5.5 Imaging

Atomic fluorescence is collected with a 0.28 NA 10X Mitutoyo Plan Apo Infinity Corrected objective purchased from Edmond optics. The objective is mounted to a 3-axis translation

stage with two axes in the plane of the main viewport and the other normal. A primary image with magnification of ≈ 1 forms ≈ 30 cm from the ion with the objective placed just outside the 34.0 mm working distance. In the case of an infinity corrected objective, rays exit parallel to the objective from a point source placed at the working distance[7]. A circular aperture at the primary image plane closes around a single ion to reduce background scatter. A secondary lens with a focal length of 150 mm forms a second image on the CCD of an Andor-iXon EMCCD with magnification ≈ 8. A TTL controlled flipper mirror intercepts the beam path sending the image to a photon counting PMT (Hamamatsu H10682-210) when necessary. An overall collection efficiency of $\approx 10^{-3}$ is dominated by the $\approx 1\%$ collection of the solid angle and $\approx 20\%$ QE of the PMT. A maximum count rate of 30 counts/ms for $^{138}Ba^{+}$ and 11 counts/ms for $^{133}Ba^{+}$ have been observed when Doppler cooling.

5.6 Experimental Control

Changing the amplitude, frequency, and phase of lasers or microwaves, shuttering lasers or microwaves, and collecting fluorescence all with precision timing are core requirements of the experiment. To accomplish these tasks, we use a custom set of electronics, referred to as the "pulser", originally designed at UC Berkeley by T. Pruttivaraisn [PK15][8]. The pulser consists of an Opal Kelly FPGA at its core, which communicates a programmed pulse sequence to up to 16 DDS boards and 32 TTL outputs, Figure 5.9. All RF switches have their TTL inputs connected to the pulser, and the 493 nm, 650 nm, and 614 nm AOMs receive RF from a pulser DDS. Most importantly, a mixer combines 9550 MHz from the HP8672A and ≈ 375 MHz from a pulser DDS to generate microwaves at the ground state hyperfine qubit frequency. Although a pulser DDS provides the HP8672A input clock allowing 1 Hz

[7]Because apo corrected objectives use a series of lenses to correct for chromatic aberrations, parallel rays exit the objective with a smaller diameter than the objective aperture. The Effective Focal Length (EFL) is defined as the focal length of a single lens producing a beam of parallel rays with the same exit diameter as the apo objective when placed an EFL away from the same point source.

[8]A wiki with more information can be found at `https://github.com/thetorque/pulse_sequencer/wiki`.

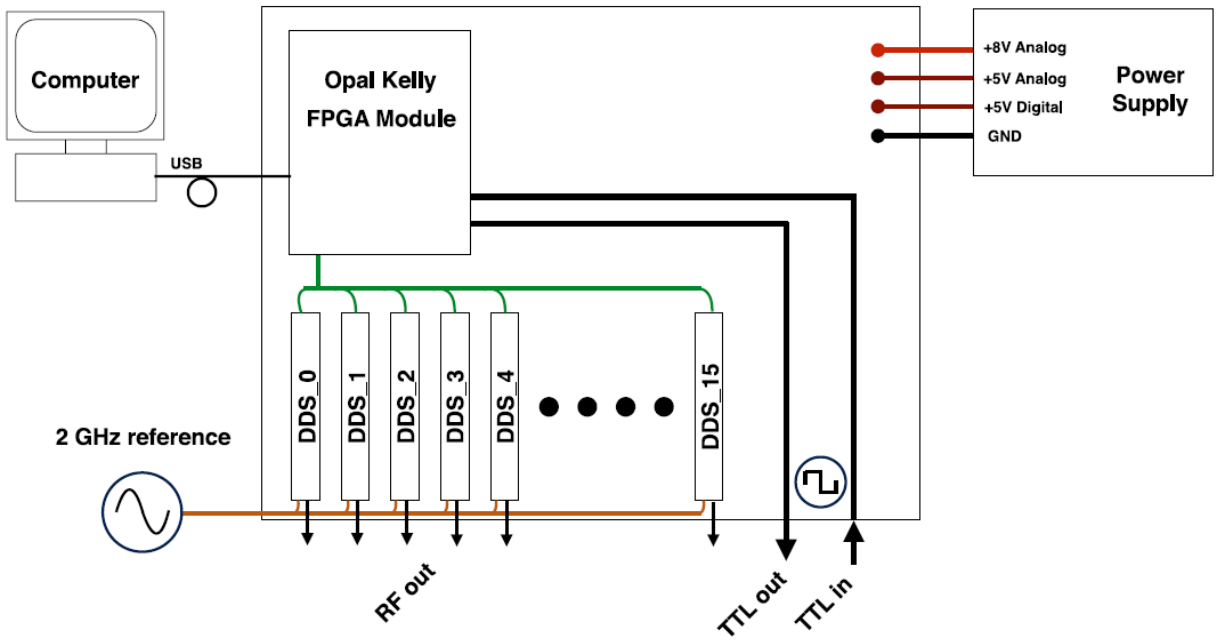

Figure 5.9: Block diagram of the electronics used to generate laser pulse sequences and count photons. Image taken from [PK15].

steps, switching times are severely limited by the internal phase locked loop (PLL). This setup allows fast switching of amplitude, phase, and frequency required for the composite pulse sequences described later.

LabRAD[9] provides the experimental control software offering a number of advantages over other platforms. These include a Python programming interface, asynchronous programming, wealth of preexisting code, and the ability communicate with hardware plugged in to any computer on the local area network (LAN). In addition, convenient software exists to manage data, experimental parameters, and pulse sequences. Fundamentally, LabRAD is based on the TCP/IP protocols originally developed for internet applications, and allows secure error checked communication between computers with internet access. The terminology used for LabRAD programs, perhaps confusing at times, generally consists of "servers", "clients", and "scripts" which originate from the TCP/IP background. Servers are just LabRAD wrappers, written in Python, allowing a LabRAD user to execute commands on

[9] `https://github.com/labrad/pylabrad/wiki`

hardware with user friendly functions. Clients are simply Python GUIs which provide a simple user interface to the servers communicating with hardware. Both servers and clients typically utilize asynchronous programming allowing parallel communication with multiple devices. Finally, scripts are typically experimental sequences which setup and program pulse sequences executed via the pulser. At the core is the LabRAD Manager[10], which manages all server and client connections. The manager typically runs on one computer (main experimental control computer) which can communicate with hardware and manage clients from any other computer. Perhaps the best example of LabRAD's utility is the server written to wrap the WSU-2 wavemeter. Setup in the Hudson lab, computers from all over the building run clients which connect to the manager running on that lab's computer. Effective real time measurements of up to 16 wavelength channels can be displayed via client or used in an experimental script on any computer that can access the UCLA network.

5.7 Time of Flight Mass Spectrometer

A time of flight mass spectrometer (TOF) was constructed and mounts to the vacuum chamber as shown in Figure 5.1. Previous versions of the TOF used in the Hudson group have demonstrated laser cooling assisted mass spectrometry (LAMS) with a resolution $\Delta m/m = 500$ [SSC14]. A rendering of the nearly identical Wiley-McLaren-type [WM55] TOF used in this experiment is shown in Figure 5.10. A TOF measurement begins via software request with trap RF termination and high voltage applied to all four rods. Ions accelerate radially from the trap passing through a grounded skimmer into a drift region. A pair of einzel lenses focus ions towards a grounded mesh followed by a negatively biased channel electron multiplier (CEM)[11]. Ions with smaller masses experience a larger acceleration $a = \frac{qE}{m}$ during extraction in the trapping region, and as a result reach the CEM first. Measurement of the $^{138}Ba^{+}$ arrival time allows calibration of all other masses[12]. Figure 5.11a shows a typical

[10] `https://github.com/labrad/scalabrad`

[11] Einzel lenses improve detection efficiency at the cost of mass resolution.

[12] Laser cooling and heating is used to purify a chain of $^{138}Ba^{+}$ for calibration.

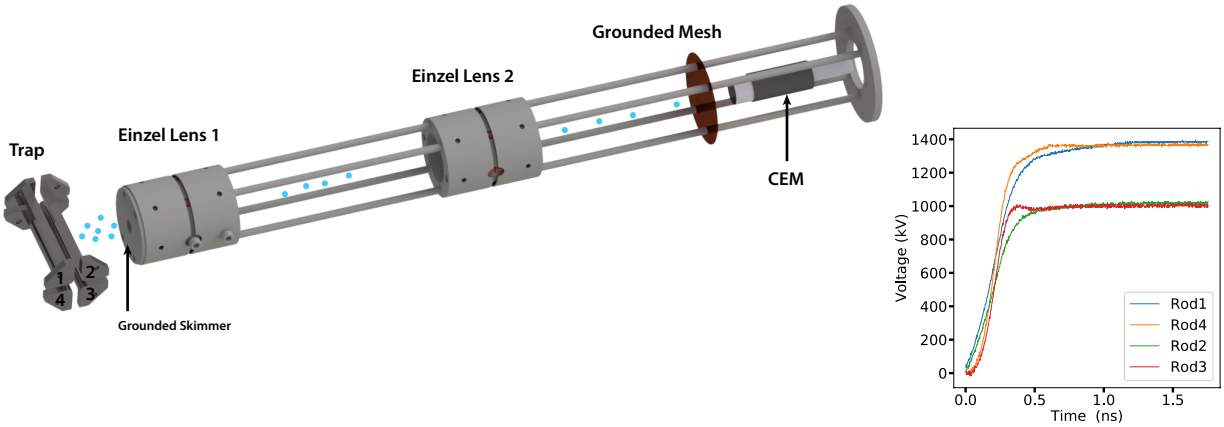

Figure 5.10: TOF and ion trap configuration.

TOF spectra for barium loaded from the naturally abundant $BaCl_2$ target. Arrival times have a square root dependence on mass as shown in Figure 5.11b.

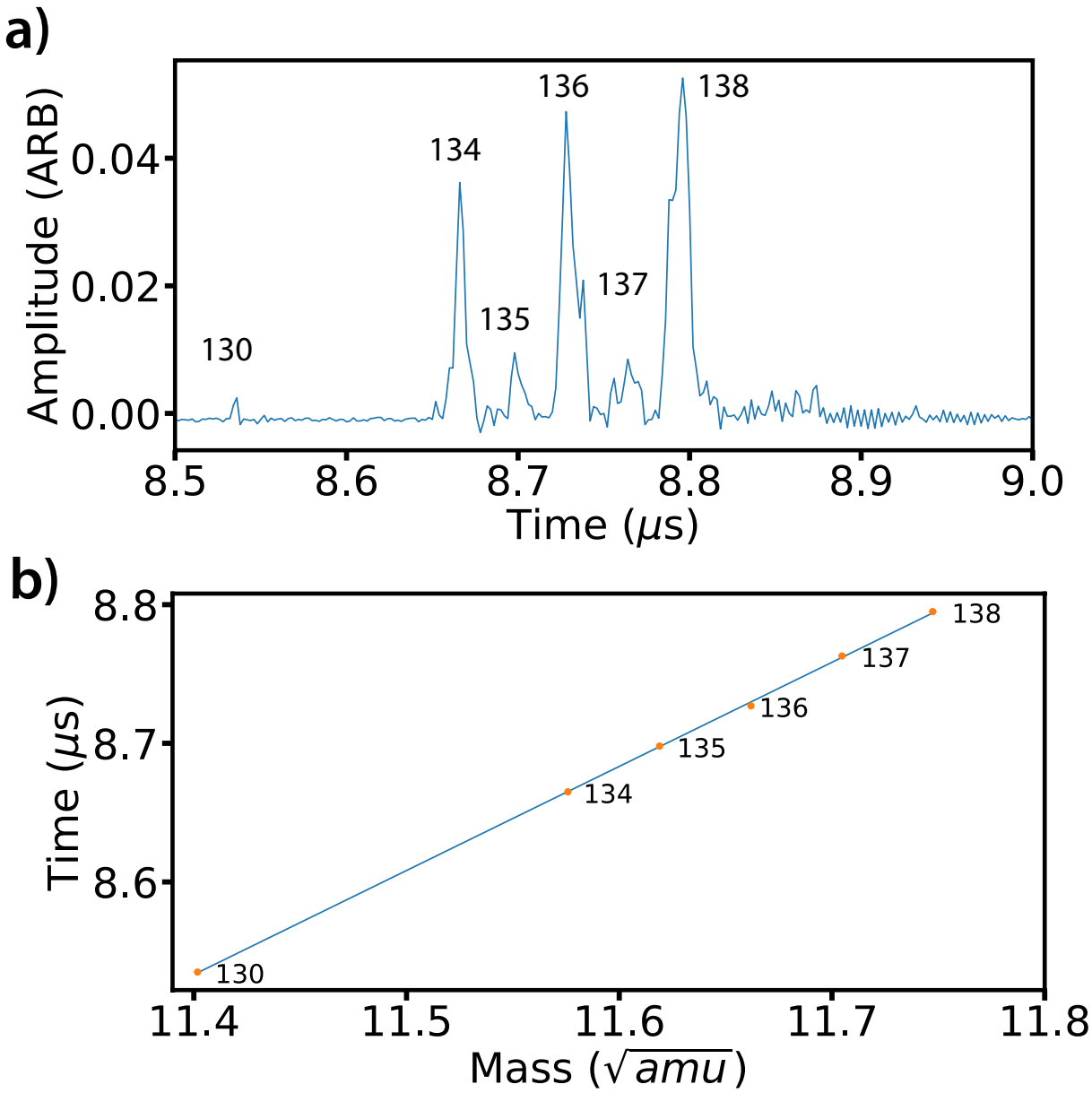

Figure 5.11: (a) Average of 25 TOF traces with laser cooled barium ions loaded from the naturally abundant $BaCl_2$ source. Loading and cooling without the sidebands necessary for $^{137}Ba^+$ and $^{135}Ba^+$ (Fig. 4.6) reduces capture and TOF efficiency. As a result, peak heights do not following isotopic abundances (Table 4.1). (b) Points are extracted arrival times from (a) verses square root of the mass. A solid line of the form $t = m \times \sqrt{mass} + b$ is fit to the points. Lighter masses undergo a larger acceleration resulting in an earlier arrival time at the detector. [WM55]

CHAPTER 6

$^{133}Ba^{+}$: The Qubit

"*Wait, I'm having one of those things, you know, a headache with pictures.*" - Philip J. Fry

The choice of atomic species as qubit host relies on the availability of long-lived electronic states to use a qubit levels, as well as relatively simple electronic structure enabling Doppler cooling, state manipulation, state preparation, and state readout. Alkaline-earth metals, coulmn IIB transition metals, and Yb of the Lanthanides are ideal choices offering hydrogen-like structure when singly ionized. While the nuclear spin-1/2 species $^{171}Yb^{+}$, $^{111/113}Cd^{+}$, and $^{199}Hg^{+}$ offer fast, high-fidelity state preparation requiring only frequency control of the applied electromagnetic radiation, they lack suitable cycling transitions far detuned from nearby levels for state readout. These nearby states limit the readout fidelity via off-resonant scatter, mixing qubit states during detection. Species such as Ca^{+}, Sr^{+}, and stable isotopes of Ba^{+} utilize metastable D states directly as qubit levels, or as storage for ground state qubits. These D states are many THz detuned from Doppler cooling cycling transitions allowing high-fidelity readout. However, state preparation in these species require higher precision polarization and frequency control, with the best demonstrated initialization fidelities an order of magnitude lower with respect to their nuclear spin-1/2 counterparts. In addition, ultraviolet (UV) light required by some species for Doppler cooling and gate operations restricts available photonic technologies available for manipulating and directing electromagnetic radiation, most notably the high attenuation in optical fibers. With no stable atomic species presenting a clear advantage, a search outside of the "accepted" list was needed.

$^{133}Ba^{+}$ provides a new qubit host, combining the advantages of many atomic species into a single system. These include (1) a spin-1/2 nucleus, (2) visible wavelength electronic transitions for Doppler cooling and qubit operations, (3) and longest-lived $^2D_{5/2}$ state ($\tau \approx$ 30 s) of all alkali-earth and alkali-earth like species. In addition to the available clock-states (described below) in the $^2S_{1/2}$ manifolds, the $^2D_{5/2}$ state possesses a pair of $m_F = 0$ levels which can be used to define a metastable hyperfine qubit, or optically separated $^2D_{5/2} \leftrightarrow {}^2S_{1/2}$ qubit (Fig. 6.1), all well protected from magnetic field noise decoherence effects.

With efficient loading from a microgram source and laser cooling demonstrated, as well as unknown state energies required for high fidelity readout measured, a path for use amongst the trapped ion community has been established. In what follows, the utility of this nearly ideal qubit is demonstrated with high-fidelity operation of the ground state hyperfine qubit, including state preparation and readout using optically pumped electron shelving detection.

6.1 Ground State Hyperfine Qubit

The ground state hyperfine qubit is defined on the pair of $m_F = 0$ states in the $^2S_{1/2}$ manifold as $|0\rangle \equiv |F{=}0\rangle$ and $|1\rangle \equiv |F{=}1; m_F{=}0\rangle$ (Fig. 6.1). Coupling of the ion's magnetic moment to the static magnetic field used to define the quantization axis and destabilize dark states induces an energy shift of the qubit levels. Described in Chapter 4, results from first-order perturbation theory give zero energy shift for states with $m_F = 0$ (Eq. 4.20). This leads to the designation of "clock-state" qubit, denoting reduced qubit frequency fluctuations from magnetic field noise compared to states with $m_F \neq 0$. However, by not including the small mixing of hyperfine states with first order perturbation theory, we have not sufficiently described the qubit frequency change as a function of magnetic field. Using the Breit-Rabi formula (Eq. 4.23), which treats Hyperfine and Zeeman interactions on equal footing, an analytic solution to the energy shift is possible.

$$E_{F=J\pm1/2} = -\frac{\Delta E_{HF}}{2(2J+1)} \pm \frac{\Delta E}{2}\sqrt{1 + \left[\frac{(g_J\mu_B - g_I\mu_N)B}{\Delta E_{HF}}\right]^2}. \tag{6.1}$$

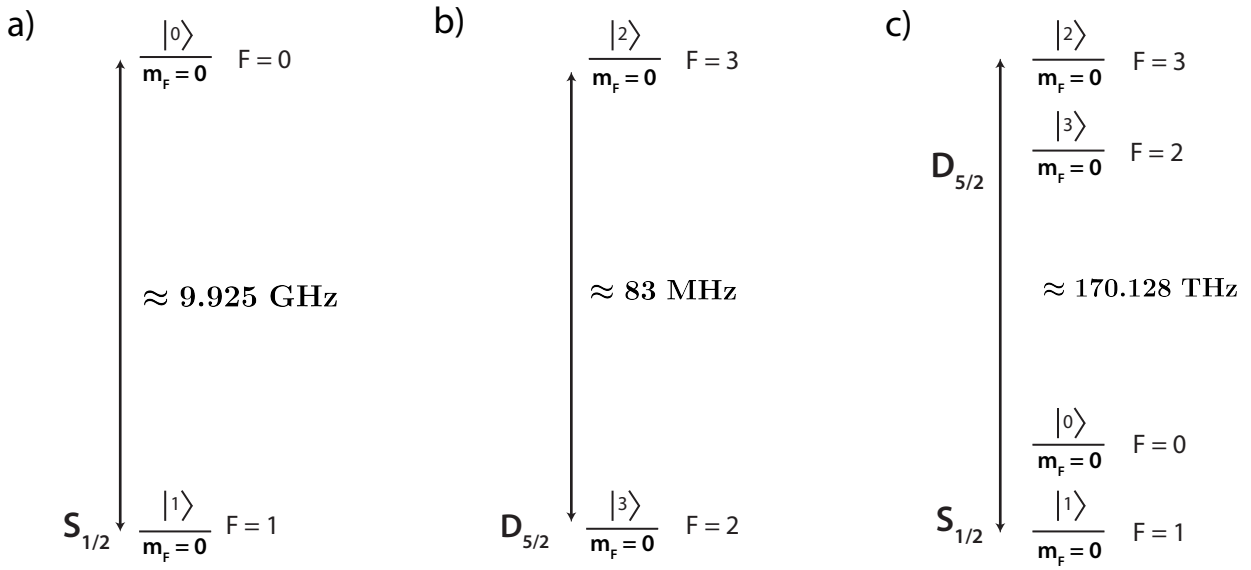

Figure 6.1: Partial list of available clock-state qubits $^{133}Ba^{+}$. (a) The $^{2}S_{1/2}$ ground state hyperfine qubit. (b) $^{2}D_{5/2}$ metastable hyperfine qubit. (c) $^{2}D_{5/2} \leftrightarrow ^{2}S_{1/2}$ optical qubits.

We would like to set our magnetic field such that $\frac{dE}{dB} = 0$. For qubits defined on $m_F = 0$ states, this only occurs at zero magnetic field, not compatible with the practical use of a magnetic field to destabilize dark states and provide a quantization axis. However, a large reduction in magnetic field sensitivity is still obtained at finite field, and shown by an expansion in powers of B around the field strength used in this experiment ($B \approx 5$ G):

$$\begin{aligned} \Delta E &\approx c_0 + c_1 \Delta B + c_2 \Delta B^2 \\ c_0 &= 9925.453554 \text{ MHz} \\ c_1 &= 0.00395 \text{ MHz/G} \\ c_2 &= 0.000395 \text{ MHz/G}^2. \end{aligned} \tag{6.2}$$

First order shifts of $c_1 \approx 4$ kHz/G are approximately three orders of magnitude smaller than qubits defined with $m_F \neq 0$ states. These approximate "clock-state" qubits have already been demonstrated in other atomic species, and shown coherence times of up to ten minutes [Fis97, WUZ17].

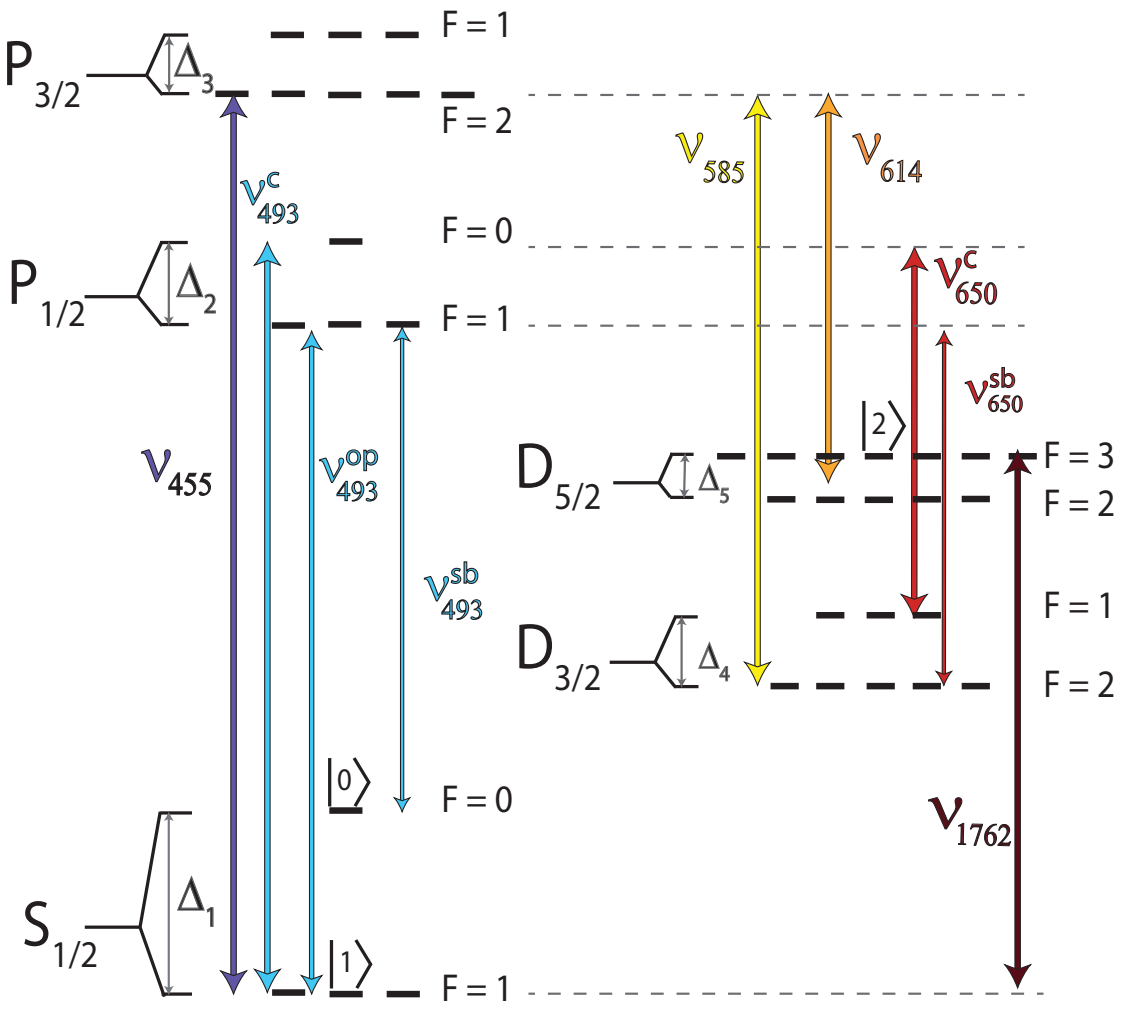

Figure 6.2: Energy level diagram of $^{133}Ba^{+}$.

6.2 Hyperfine-Selective SPAM

With nuclear spin-1/2, the $^{133}Ba^{+}$ $^{2}S_{1/2}$ and $^{2}P_{1/2}$ manifolds posses $F = 0$ states (Figure 6.2), allowing fast, hyperfine-selective state preparation ($|0\rangle$ state) and readout ($|0\rangle$ and $|1\rangle$ states) relying solely on frequency selectivity. $|0\rangle$ is initialized after Doppler cooling (ν^{c}_{493}, ν^{sb}_{493}, ν^{c}_{650}, and ν^{sb}_{650}) by removing the repumper resonant with the $|^{2}P_{1/2};F{=}1\rangle \leftrightarrow |^{2}S_{1/2};F{=}0\rangle$ transition (ν^{sb}_{493}), and applying a tone (ν^{op}_{493}) resonant with the $|^{2}P_{1/2};F{=}1\rangle \leftrightarrow |^{2}S_{1/2};F{=}1\rangle$ states (Figure 6.2). Spontaneous emission quickly populates the $|0\rangle$ state with high-fidelity as shown in the simplified level diagram of Figure 6.3a. To estimate errors in preparation,

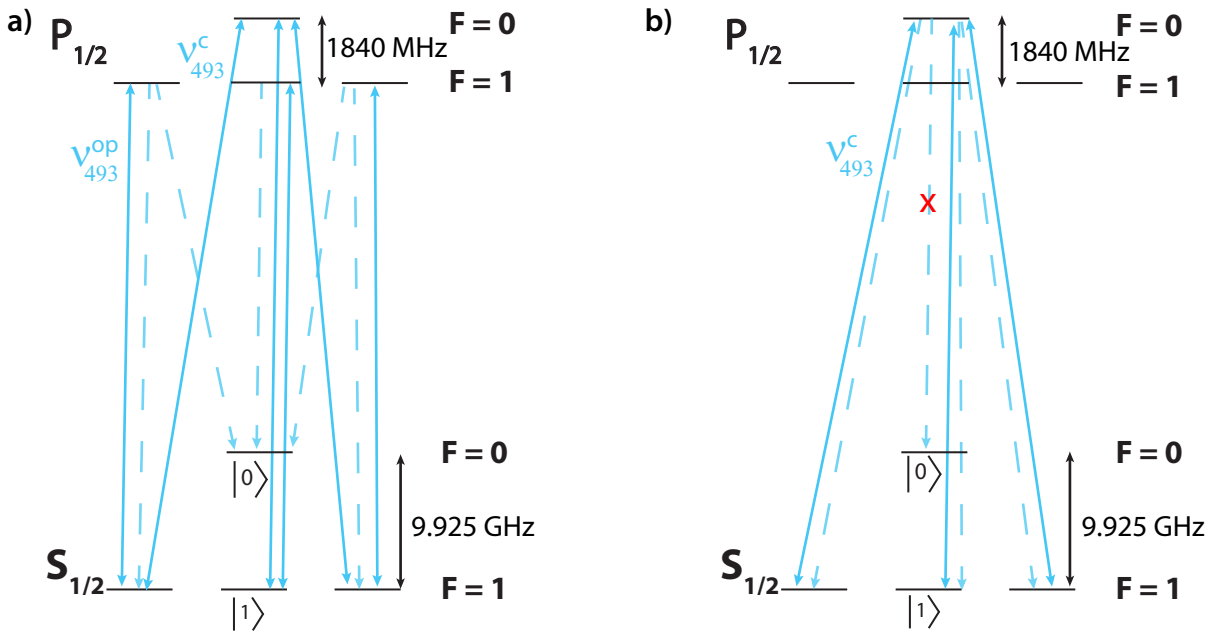

Figure 6.3: Hyperfine-selective state preparation and readout scheme. Repumping of the $^2D_{3/2}$ states near 650 nm (Fig. 6.2) have been omitted for clarity. (a) 493 nm frequencies applied for state preparation of $|0\rangle$. The laser carrier (ν^c_{493}) resonant with the $|^2P_{1/2};F{=}0\rangle \leftrightarrow |^2S_{1/2};F=1\rangle$ transition is phase modulated using a fiber EOM producing a firt-order sideband resonant with the $|^2P_{1/2};F{=}1\rangle \leftrightarrow |^2S_{1/2};F=1\rangle$ transition (ν^{op}_{493}), quickly populating the $|0\rangle$ state. (b) 493 nm frequency applied for hyperfine-selective state readout. Dipole selection rules forbid decay of the $|^2P_{1/2};F{=}0\rangle$ to the $|0\rangle$ state.

the off-resonant scattering rate (Eq. 3.28) out of $|0\rangle$ via ν^{op}_{493} is compared to the resonant scattering rate in. Assuming the saturation parameter (Eq. 3.29) is small ($s \ll 1$), the preparation infidelity ($\epsilon_{|0\rangle}$) is estimated as:

$$\epsilon_{|0\rangle} \approx \left(\frac{\Gamma}{2\Delta}\right)^2 \approx 10^{-6}. \tag{6.3}$$

Hyperfine-selective readout is accomplished by applying tones ν^c_{493} and ν^c_{650} resonant with $|^2P_{1/2};F{=}0\rangle \leftrightarrow |^2S_{1/2};F{=}1\rangle$ and $|^2P_{1/2};F{=}0\rangle \leftrightarrow |^2D_{3/2};F{=}1\rangle$ transitions (Figure 6.2). As shown in the simplified diagram in Figure 6.3b, an ion in the $|1\rangle$ state ("bright state") scatters many photons, while an ion in the $|0\rangle$ state ("dark state") does not. The dipole selection rule $F' = 0 \not\leftrightarrow F'' = 0$ forbids mixing of the two qubit states via spontaneous emission from the $|^2P_{1/2};F{=}0\rangle$ state. However, off-resonant scatter and emission from the

$|^2\mathrm{P}_{1/2}\,;\mathrm{F}{=}1\rangle$ manifold can cause population in the $|1\rangle$ state to decay to $|0\rangle$.

Given population in either $|0\rangle$ or $|1\rangle$, we'd like to use any collected fluorescence to discriminate between our two qubit states with minimal error. During hyperfine-selective readout, the probability of detecting n photons during detection time t_D after initialization to $|0\rangle$ is given by [ABH06]:

$$P_{|0\rangle}(n) = e^{-\alpha_1\lambda_0/\eta}\left[\delta_n + \frac{\alpha_1/\eta}{(1-\alpha_1/\eta)^{n+1}}\mathcal{P}(n+1,(1-\alpha_1/\eta)\lambda_0)\right] \tag{6.4}$$

where $\mathcal{P}(a,x)$ is the incomplete gamma function, η total photon collection efficiency, α_1 leak probability per emitted photon, and λ_0 number of detected photons when starting in $|1\rangle$. The total photon collection efficiency is given by:

$$\eta = \eta_\mathrm{D}\frac{d\Omega}{4\pi}T \tag{6.5}$$

with η_D the detector efficiency, $\frac{d\Omega}{4\pi}$ solid angle of light collected, and T transmission through the collection optics. The leak probability per emitted photon is given by:

$$\alpha_1 = \frac{t_\mathrm{D}\eta}{\tau_{L1}\lambda_0} \tag{6.6}$$

with τ_{L1} the time constant to leak from the $|0\rangle$ state to the $|1\rangle$ state. Leakage to the bright state occurs via off-resonant scatter from ν^c_{493}, detuned by the approximate sum of the $^2\mathrm{S}_{1/2}$ and $^2\mathrm{P}_{1/2}$ hyperfine splittings (Figure 6.3). The ratio of resonant to off-resonant scattering rates (Eq. 3.28) determine α_1:

$$\alpha_1 = M_1\left((1+s+\left(\frac{2\delta}{\gamma}\right)^2\right)\left(\frac{\gamma}{2(\Delta_1+\Delta_2)}\right)^2 \tag{6.7}$$

with M_1 the branching ratio tot the $|1\rangle$ state, s the saturation parameter, δ the laser detuning (ν^c_{493}) during detection, γ the excited state linewidth, and Δ_1 (Δ_2) the ground (excited) state hyperfine splitting (Fig. 6.2). Using parameters from this experiment (Chapter 5), as well as $^{133}\mathrm{Ba}^+$ atomic parameters (Chapter 4), the probability of detecting n photons is plotted in Figure 6.4a for different values of the number of collected photons when starting in the bright state.

Similarly, the probability during readout of detecting n photons with the population initialized to $|1\rangle$ is given by:

$$P_{|1\rangle}(n) = \frac{e^{-(1+\alpha_2/\eta)\lambda_0}\lambda_0^n}{n!} + \frac{\alpha_2/\eta}{(1+\alpha_2/\eta)^{n+1}}\mathcal{P}(n+1,(1+\alpha_1/\eta)\lambda_0) \tag{6.8}$$

with α_2 given by:

$$\alpha_2 = \frac{t_D \eta}{\tau_{L2}\lambda_0}. \tag{6.9}$$

The leak rate per emitted photon for the bright state is similar to α_1, but with new branching ratio and off-resonant detuning:

$$\alpha_2 = M_2\left((1+s+\left(\frac{2\delta}{\gamma}\right)^2\right)\left(\frac{\gamma}{2(\Delta_2)}\right)^2. \tag{6.10}$$

The first term in Equation 6.8 is the Poisson distribution from when the ion never leaves the $|^2P_{1/2};F{=}0\rangle \leftrightarrow |^2S_{1/2};F{=}1\rangle$ cycling transition. The second term accounts for leakage into the $|0\rangle$ state via off-resonant scatter through the $|^2P_{1/2};F{=}1\rangle$ states. Figure 6.4b shows a plot of Equation 6.8 for different values of the average number of collected photons when starting in the bright state. For larger values of s, and hence increased number of detected photons, a "bright state tail" can be seen due to the increased probability of off-resonant scatter during the early part of the detection window.

Detection fidelity is determined by a threshold discriminator (N_{th}) on the number of collected photons n, and is the probability of collecting $n > N_{th}$ when starting in the $|1\rangle$ state, and $n \leq N_{th}$ when starting in $|0\rangle$. The detection fidelity is maximized when the two fidelities are equal:

$$\mathcal{F} = \sum_{n=0}^{N_{th}} P_{|0\rangle}(n) = 1 - \sum_{n=0}^{N_{th}} P_{|1\rangle}(n). \tag{6.11}$$

Common practice in the field reports the average fidelity, defined as:

$$\mathcal{F} = \frac{1}{2}\left(\mathcal{F}_{|0\rangle} + \mathcal{F}_{|1\rangle}\right) \tag{6.12}$$

with $\mathcal{F}_{|0\rangle}$ the readout fidelity of $|0\rangle$ and $\mathcal{F}_{|1\rangle}$ the readout fidelity of $|1\rangle$. Using Equations 6.4 and 6.8 with current experimental parameters, a threshold value of $N_{th} = 0$ and $N_{th} = 1$ give maximum average fidelities of $\mathcal{F} = 0.985$ and $\mathcal{F} = 0.972$. The above theory does consider

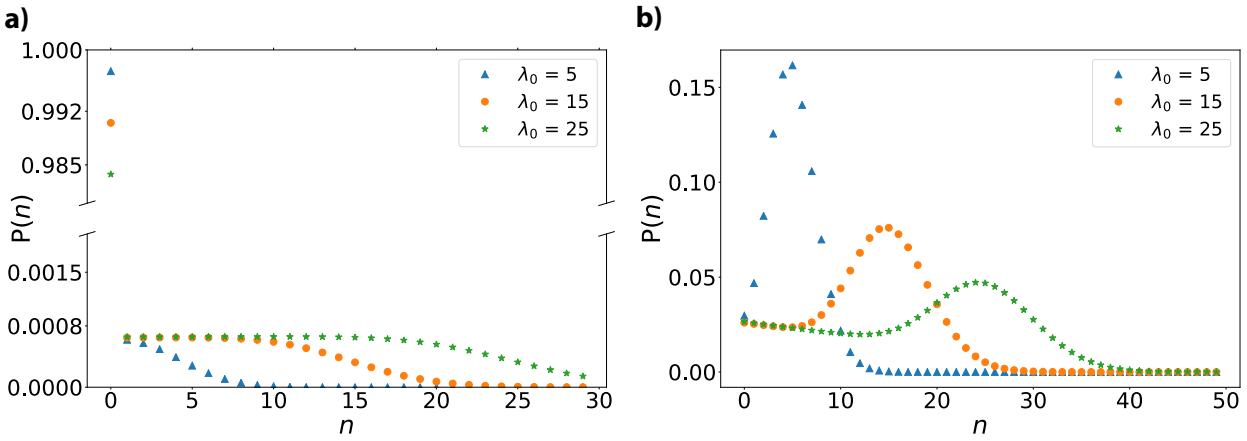

Figure 6.4: Probability of detecting n photons using the $^2P_{1/2}$ state for hyperfine-selective readout for different values of the average number of collected photons when starting in the bright state. Here, the detection time was fixed to 4.5 ms and the saturation parameter varied. (a) Probability of detecting n photons when starting in the $|0\rangle$ state. (b) Probability of detecting n photons when starting in the $|1\rangle$ state.

background scatter from the detection laser or PMT dead counts, which lead to a larger dark state mean count rate and reduced average fidelity.

The $|1\rangle$ state cannot be initialized via hyperfine-selective optical pumping using only frequency selectivity, however, high-fidelity preparation can still be accomplished with microwave radiation near 9.925 GHz. Application of time-dependent magnetic fields will coherently transfer population between qubit levels and are termed magnetic dipole (M1) transitions. The Hamiltonian for a magnetic dipole transition is given by:

$$H = -\vec{\mu} \cdot \vec{B} \tag{6.13}$$

where $\vec{\mu} = \vec{\mu_S} + \vec{\mu_L} + \vec{\mu_I}$. In the $^{133}Ba^+$ ground state, $\vec{L} = 0$, giving:

$$\vec{\mu} = -g_s \mu_B \vec{S} - g_I \mu_N \vec{I}. \tag{6.14}$$

The perturbing magnetic field is given by:

$$\vec{B} = B_0 \cos(\omega t)\hat{\epsilon} \tag{6.15}$$

with $\hat{\epsilon}$ a unit vector defining the polarization. The Hamiltonian in matrix form is given by:

$$\mathcal{H} = \begin{pmatrix} 0 & \frac{\Omega}{2}e^{-i\omega t} \\ \frac{\Omega}{2}^* e^{i\omega t} & \omega_0 \end{pmatrix} \tag{6.16}$$

where the Rabi frequency can be analytically calculated and is given by $\Omega = B_0(g_s\mu_B - g_I\mu_N)$. This Hamiltonian is of the same form as Equation 3.3, and using the rotation matrix (Eq. 3.23) previously calculated, rotations of the qubit Bloch vector about $\cos(\phi)\hat{x} + \sin(\phi)\hat{y}$ through angle θ, $R(\theta, \phi)$ are accomplished by controlling the amplitude, frequency, and phase of the applied radiation.

The $|1\rangle$ state can be prepared after initialization into $|0\rangle$ by $R(\pi, 0)$, however, a composite pulse sequence, referred to as the CP Robust 180 sequence (attributed to E. Knill) [RHC10], consisting of the five π-pulses $R(\pi, \frac{\pi}{6})R(\pi, 0)R(\pi, \frac{\pi}{2})R(\pi, 0)R(\pi, \frac{\pi}{6})$ improves fidelity in the presence of pulse area and detuning errors. Figure 6.5 shows a theoretical plot of the CP Robust 180 sequence where the $|1\rangle$ state population is plotted verses detuning and pulse area. The broad flat features in both curves near zero detuning and $\theta = \pi$ demonstrate resiliency to both pulse area and detuning errors as compared to single π-pulses.

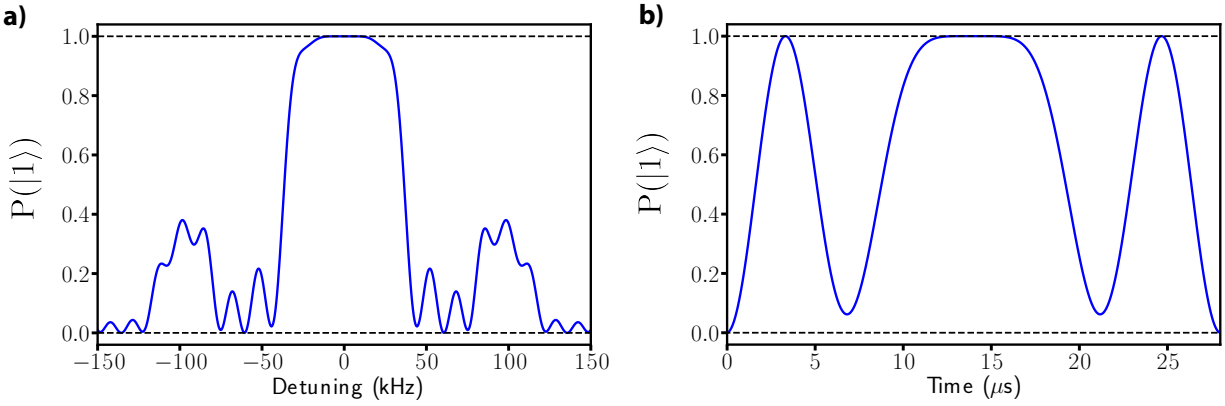

Figure 6.5: (a) Theoretical probability of $|1\rangle$ state population *vs.* microwave detuning ($\Delta = \omega -$ 9.925 GHz) using the CP Robust 180 sequence. (b) Theoretical probability of $|1\rangle$ state population *vs.* pulse area ($\theta = \Omega_R t$) using the CP Robust 180 sequence with $\Omega_R = 2\pi\times$ 35 kHz and no detuning.

6.3 Electron-Shelving Readout

6.3.1 Readout Fidelity

While high-fidelity SPAM has been demonstrated with hyperfine-selective optical cycling using large numerical aperture objectives [NVG13, CCV19], constraints on future architectures may ultimately limit readout fidelities using this scheme. $^{133}Ba^{+}$ offers another path to high-fidelity state detection utilizing a metastable state removed from the cooling cycle.

The $|1\rangle$ qubit state can be shelved [Deh75] to the long-lived ($\tau \approx 30$ s) metastable $^2D_{5/2}$ state via the $^2D_{5/2} \leftrightarrow {}^2S_{1/2}$ transition, or optically pumped via the $^2P_{3/2}$ state (Fig. 6.2), followed by Doppler cooling for state readout. As before, we'd like to use any collected fluorescence to discriminate between the $|0\rangle$ and $|1\rangle$ states, as an atom in the $|0\rangle$ state scatters many photons, while an atom in the $^2D_{5/2}$ state, indicating $|1\rangle$, does not. We note the labels have flipped, with $|0\rangle$ now the "bright" state and $|1\rangle$ the "dark" state.

Leakage from $|0\rangle \rightarrow |1\rangle$ is negligible as the Doppler cooling lasers are detuned by many THz from any $^2D_{5/2}$ state transition. Following previous works [Lan06, Bur10], the probability of detecting n photons when starting in $|0\rangle$ is given by a Possionian distribution:

$$P_{|0\rangle}(n) = \frac{e^{-\lambda_0}\lambda_0^n}{n!} \tag{6.17}$$

with λ_0 representing the mean number of collected photons during detection time t_D and includes contributions from background laser scatter. The probability of detecting n photons after shelving $|1\rangle$ to the $^2D_{5/2}$ state is given by:

$$P_{|1\rangle}(n) = e^{-t_D/\tau}\frac{e^{-\lambda_d}\lambda_d^n}{n!} + L(n). \tag{6.18}$$

The first term is a Poisson distribution with mean number of detected photons λ_d, weighted by the probability the ion does not decay during the detection time. λ_d is the mean number of collected photons when the ion stays in the $^2D_{5/2}$ state during the entire detection period. $L(n)$ is composed of weighted Possion distributions with means between λ_0 and λ_d, and

account for when the ion decays during readout. The distribution is given by:

$$L(n) = \frac{e^{-\xi}(\lambda_{\mathrm{d}}\tau/t_{\mathrm{D}})^n}{n!}\,(\lambda_{\mathrm{d}}\tau/t_{\mathrm{D}}-1)^{-(n+1)}\,\Gamma(n+1)\times \left[P(n+1,\xi(\lambda_{\mathrm{d}}\tau/t_{\mathrm{D}}-1)) - P\left((n+1),\frac{\lambda_0 t_{\mathrm{D}}}{\lambda_{\mathrm{d}}\tau}(\lambda_{\mathrm{d}}\tau/t_{\mathrm{D}}-1)\right)\right] \tag{6.19}$$

with ξ given by:

$$\xi = \frac{(\lambda_0+\lambda_{\mathrm{d}})t_{\mathrm{D}}}{\tau}. \tag{6.20}$$

$\Gamma(a)$ is the gamma function, and $P(a,x)$ the incomplete gamma function.

The detection fidelity of each state is calculated as before using Equation 6.11. Using experimental and $^{133}\mathrm{Ba}^+$ atomic parameters, Figure 6.6 shows the estimated number of collected photons in each of 10^5 readout trials after initialization to $|0\rangle$ or $|1\rangle$. A threshold discriminator at $N_{\mathrm{th}} = 12$ maximizes the estimated average fidelity of $\mathcal{F} = 0.9999$.

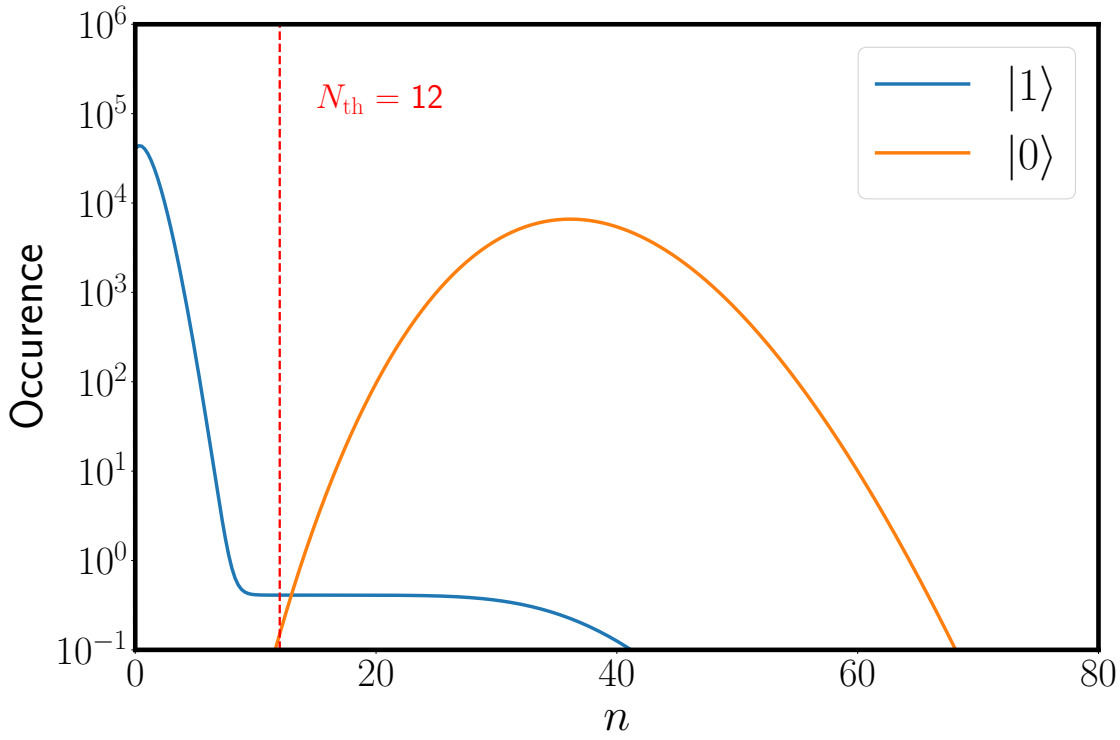

Figure 6.6: Estimated number of collected photons (10^5 readout trials for each state) after initialization to $|0\rangle$ or $|1\rangle$ using experimental and $^{133}\mathrm{Ba}^+$ atomic parameters. A threshold of $N_{th} = 12$ maximizes the average detection fidelity of $\mathcal{F} = 0.9999$.

6.3.2 Optically-Pumped Electron Shelving

The optically-pumped shelving scheme utilizes visible wavelength electronic dipole transitions and favorable branching ratios to quickly move population in the $|1\rangle$ state to the $^2\mathrm{D}_{5/2}$ manifolds. In what follows, three shelving schemes are described and their respective fidelities estimated.

Initialization to $|1\rangle$ is followed by illumination with a laser resonant with the $|\,^2\mathrm{P}_{3/2}\,;F{=}2\rangle \leftrightarrow |^2\mathrm{S}_{1/2}\,;F=1\rangle$ transition (ν_{455}) at an intensity below saturation (Fig. 6.2). After excitation of the atom, the $^2\mathrm{P}_{3/2}$ state quickly ($\tau \approx 10$ ns) spontaneously decays to either the $^2\mathrm{S}_{1/2}$, $^2\mathrm{D}_{5/2}$, or $^2\mathrm{D}_{3/2}$ state [DDY16]. Dipole selection rules forbid decay to the $|0\rangle$ state, resulting in $\mathcal{F} = 0.88$ shelving fidelity, limited by population stranded in the $^2\mathrm{D}_{3/2}$ states. To further increase the shelving fidelity, a 650 nm laser near resonant with the $|^2\mathrm{P}_{1/2}\,;F{=}0\rangle \leftrightarrow |^2\mathrm{D}_{3/2}\,;F{=}1\rangle$ transition (ν^c_{650}), and a laser near 585 nm (ν_{585}) resonant with the $|^2\mathrm{P}_{3/2}\,;F{=}2\rangle \leftrightarrow |^2\mathrm{D}_{3/2}\,;F{=}2\rangle$ transition can be applied at an intensity below saturation. The hyperfine structure of $^{133}\mathrm{Ba}^+$ allows for concurrent repumping of the $^2\mathrm{D}_{3/2}$ states (ν_{585} and ν^c_{650}) with all polarization components during the application of ν_{455}, simplifying the shelving sequence compared with other species [HAB14]. Dipole selection rules forbid spontaneous emission to the $|0\rangle$ state resulting in a fidelity of $\mathcal{F} \approx 0.999$. This scheme is limited by off-resonant scatter of ν_{455} to the $|^2\mathrm{P}_{3/2}\,;F{=}1\rangle$ state, where 0.44 of decays to the $^2\mathrm{S}_{1/2}$ are to $|^2\mathrm{S}_{1/2}\,;F{=}0\rangle$. If ν_{455} is linearly polarized parallel to the magnetic field direction (π-light), dipole selection rules forbid excitation from the $|^2\mathrm{P}_{3/2}\,;F{=}1;m_F{=}0\rangle \leftrightarrow |^2\mathrm{S}_{1/2}\,;F{=}1;m_F{=}0\rangle$ for the first scattered photon, and the expected fidelity increases to $\mathcal{F} = 0.9998$.

In addition to $|1\rangle$ state errors during shelving, off-resonant excitation to the $|^2\mathrm{P}_{3/2}\,;F{=}1\rangle$ followed by spontaneous emission can shelve an ion initialized in the $|0\rangle$ state to the $^2\mathrm{D}_{5/2}$ manifolds. This results in an expected $|0\rangle$ state SPAM fidelity of $\mathcal{F} = 0.9998$.

6.4 Experimental Results

With qubit operations and their respective fidelities estimated, we now move to experimental implementation. The general state of the qubit is given by:

$$|\psi\rangle = C_0(t)|0\rangle + C_1(t)e^{i\omega_0 t}|1\rangle \tag{6.21}$$

where the probability of a measurement yielding $|0\rangle$ is given by $|C_0|^2$, and the probability of measurement returning $|1\rangle$ given by $|C_1|^2$. However, the readout schemes previously described are single projective measurements returning the binary result of $|0\rangle$ or $|1\rangle$. To estimate probabilities, N_{tot} repeated trials of the same experiment attempt to produce the same quantum state, with each trial followed by a projective measurement. The average population is then given by:

$$\overline{P} = \frac{N}{N_{\text{tot}}} \tag{6.22}$$

where N is number of trials with $n > N_{\text{th}}$ (bright) or $n \leq N_{\text{th}}$ (dark). A histogram best visualizes the data and is shown in Figure 6.7 for three different initial quantum states.

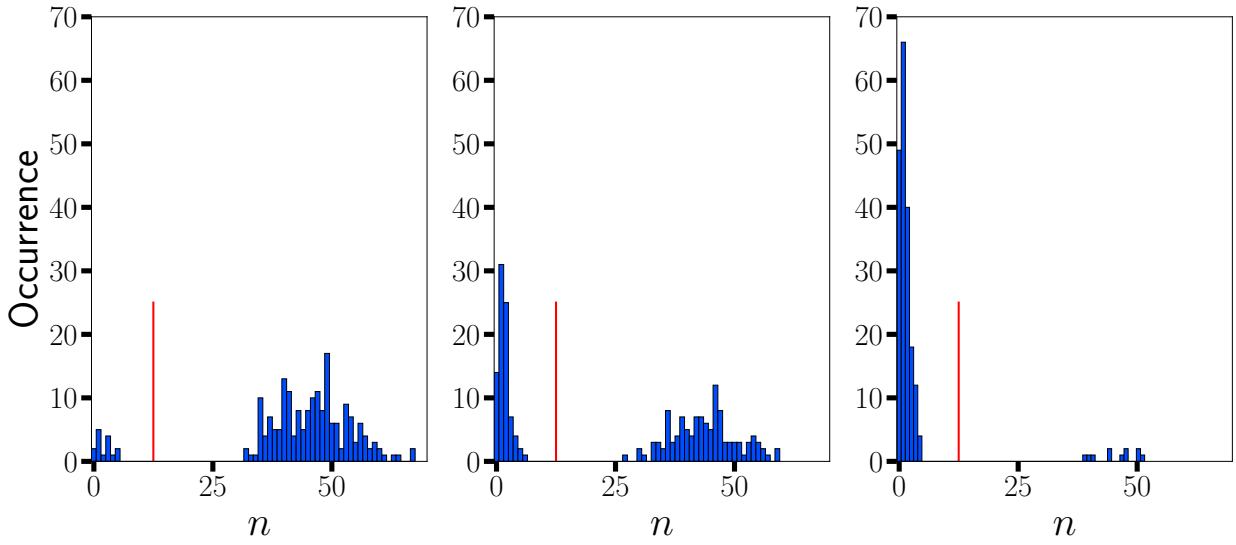

Figure 6.7: Three histograms estimating $|0\rangle$ state population with electron shelving detection. Left: $P(|0\rangle) \approx 1$, middle: $P(|0\rangle) \approx 0.5$, right: $P(|0\rangle) \approx 0$.

The $|0\rangle$ state is quickly prepared with high fidelity after Doppler cooling by applying frequencies ν^{c}_{493}, ν^{op}_{493}, ν^{c}_{650}, and ν^{sb}_{650}. Figure 6.8 shows the measured population of the $|0\rangle$

state as a function of preparation time using the electron shelving readout scheme. Each point represents 200 repeated trials using a threshold of $N_{\text{th}} = 12$ to discriminate between qubit states.

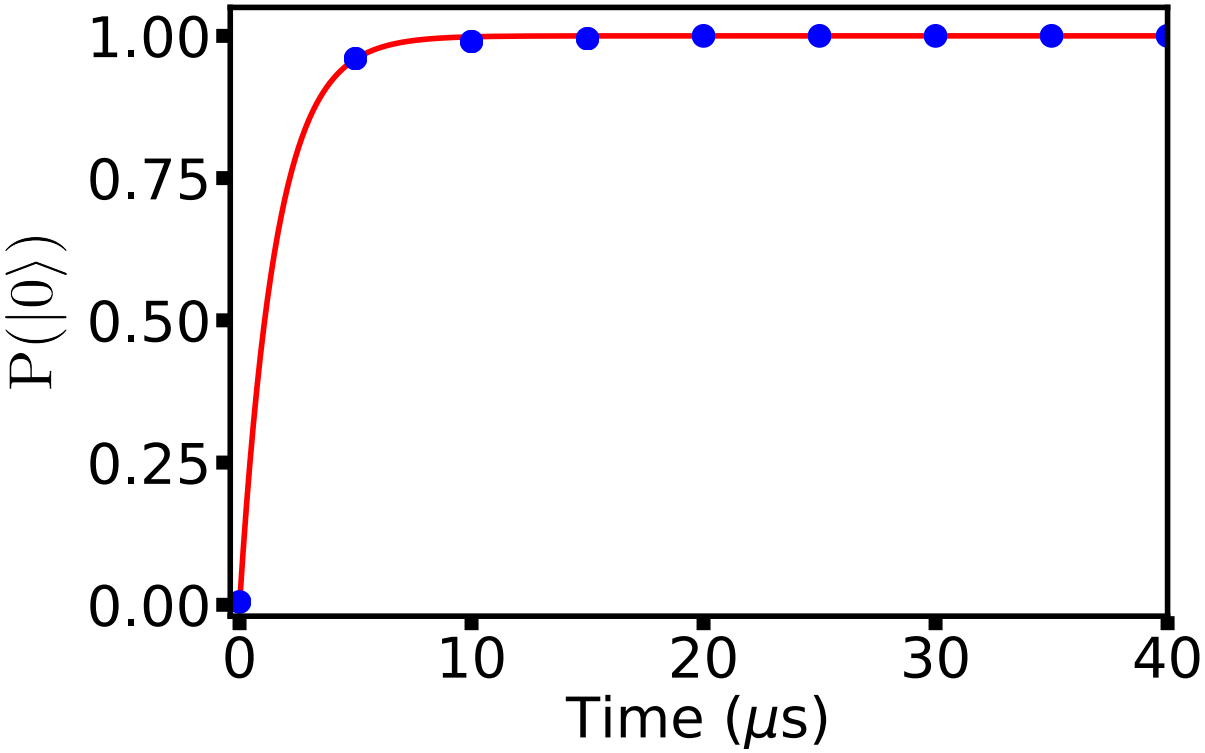

Figure 6.8: Measured population of the $|0\rangle$ state after applying frequencies ν^{c}_{493}, ν^{op}_{493}, ν^{c}_{650}, and ν^{sb}_{650} for a given period of time. Each point represents 200 repeated trials using electron shelving readout scheme and a threshold of $N_{\text{th}} = 12$ to discriminate between qubit states. Red line is an exponential fit to the data.

Given initialization into $|0\rangle$, the probability of finding the population in $|1\rangle$ after rotation $R(\Omega_R t, 0)$ is given by the well known Rabi equation:

$$P(|1\rangle\,) = \frac{\Omega^2}{\Omega^2 + \Delta^2} \sin^2\left(\frac{\sqrt{\Omega^2 + \Delta^2}}{2} t\right). \tag{6.23}$$

Figure 6.9a showns a Rabi flopping curve generated by application of microwaves near 9.925 GHz and $\Omega_R = 2\pi \times 57.03(3)$ kHz, with no decrease in contrast is observed over

many periods. To benchmark the coherence between the microwave and qubit oscillators, a

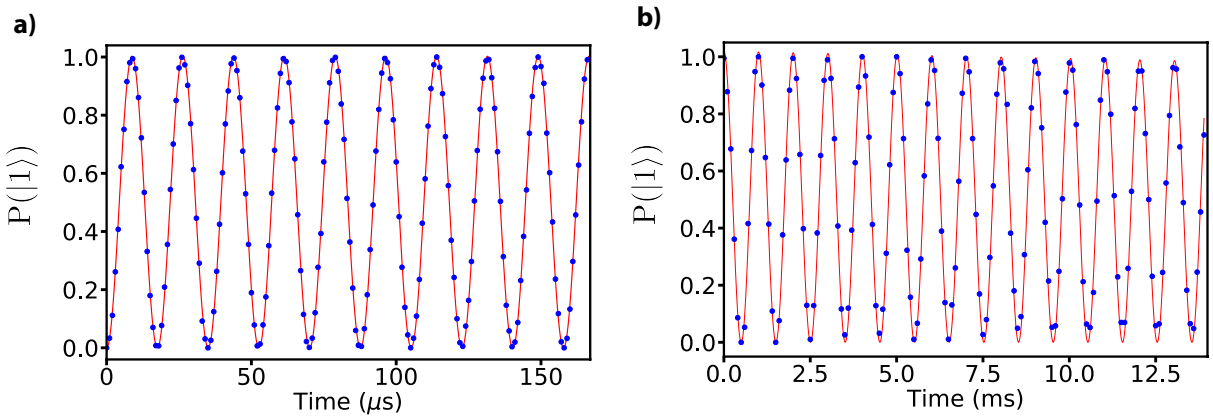

Figure 6.9: (a) Probability of detecting $|1\rangle$ after microwave rotations of the form $R(\Omega_R t, 0)$, where $\Omega_R = 2\pi \times 57.03(3)$ kHz. Each point represents 1000 repeated trials using threshold discrimination to determine the qubit state. Red line is a fit to Equation 6.23 with $\Delta = 0$. (b) Probability of detecting $|1\rangle$ as a function of Ramsey delay time using the Ramsey sequence $R(\pi/2, 0)$, $R(0 \times t_{\text{delay}}, 0)$,$R(\pi/2, 0)$. Each point represents 200 repeated trials and threshold discrimination of the two qubit states. Both plots use the high-fidelity electron shelving technique for state readout.

Ramsey sequence of the form $R(\pi/2, 0)$, $R(0 \times t_{\text{d}}, 0)$,$R(\pi/2, 0)$ was performed with a detuning of $\Delta \approx 1$ kHz. t_{d} represents the wait time in between $\pi/2$-pulses, and a plot of the $|1\rangle$ state population as a function of delay is given in Figure 6.9 b. The envelop of the data was fit to an exponential decay function and returned a time constant of 0.4(1) s. A large uncertainty in the fit results from the lack of data points at long delay times, where an unknown source of ion heating prevented measurement.

To prepare the $|1\rangle$ state, the $|0\rangle$ state is initialized followed by application of the CP Robust 180 sequence $R(\pi, \frac{\pi}{6})R(\pi, 0)R(\pi, \frac{\pi}{2})R(\pi, 0)R(\pi, \frac{\pi}{6})$. To experimentally test the predicted line shapes in Figure 6.5, the probability of the $|1\rangle$ state is measured as a function of pulse area and detuning, shown in Figure 6.10. Each data point represents 200 trials with electon shelving detection and threshold discrimination to determine the qubit state. Solid red lines are theory with no fit parameters. To estimate and separate the contribution of microwave errors from $|0\rangle$ state initialization in preparing the $|1\rangle$ state, CP Robust 180

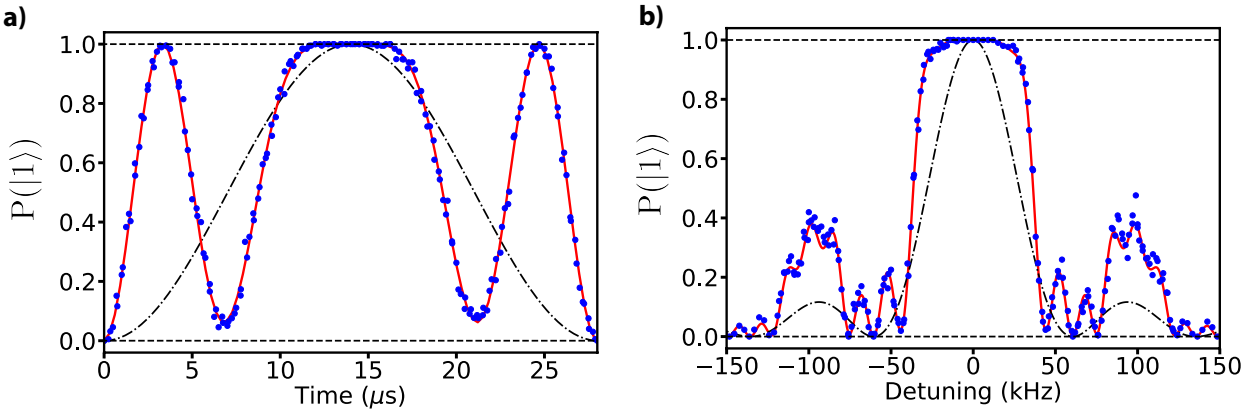

Figure 6.10: (a) Probability of $|1\rangle$ *vs.* microwave detuning using the CP Robust 180 sequence with $\Omega_R = 2\pi\times$ 35.4(1) kHz. Points are experimental data and solid line represents theoretical prediction for this composite pulse sequence with no fit parameters (b) Pulse area ($t = \frac{\theta}{\Omega_R}$) scan at zero detuning using the CP Robust 180 sequence. Dashed dotted lines in (b,c) are theory for a single π-pulse, $R(\pi, 0)$. Statistical error bars on individual data points are smaller than markers

sequences are concatenated together. The microwave phase is randomly chosen before each sequence to remove coherent effects, and numerical simulations modeling pulse area and detuning errors show a linear decrease in population transfer as a function of concatenated composite sequences. Figure 6.11 shows a plot of $|1\rangle$ state infidelity as a function of concatenated CP Robust 180 sequences, with a straight line fit giving a error per pulse sequence of $\epsilon = 9(1) \times 10^{-5}$.

6.4.1 SPAM Results

We use the same single trapped $^{133}Ba^{+}$ ion to determine our state preparation and measurement fidelity (SPAM) using the hyperfine-optical cycling combined with the CP Robust 180 sequence. Before each SPAM attempt, the Doppler cooling fluorescence is monitored to determine if a SPAM attempt can be made. If the count rate does not reach a predetermined threshold of 2σ below the Doppler cooling mean count rate, chosen before the experiment begins and constant for all SPAM measurements, the subsequent SPAM attempt is not included. Laser cooling is accomplished using external cavity diode lasers (ECDLs)

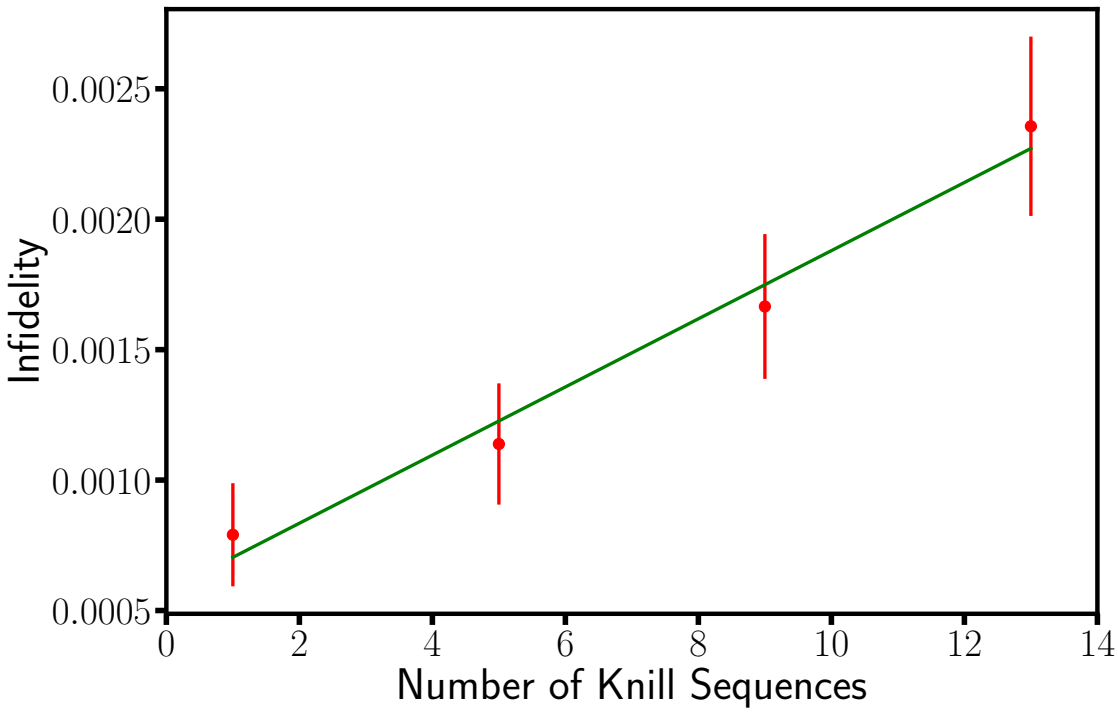

Figure 6.11: Measurement of the $|1\rangle$ state infidelity versus number of concatenated CP Robust 180 sequences. Straight line fit gives a error per pulse sequence of $\epsilon = 9(1) \times 10^{-5}$

near 493 nm and 650 nm detuned approximately half an atomic linewidth from the resonant transitions (ν^c_{493} and ν^c_{650}) with saturation parameters $s \approx 10$. Preparation of the $|0\rangle$ state is accomplished by removing ν^{sb}_{493} and adding ν^{op}_{493} for 100 μs after Doppler cooling with a saturation parameters of $s \approx 1$. The $|1\rangle$ state is prepared via the CP Robust 180 sequence with approximately 3 W of microwave power directed with a microwave horn for ≈ 15 μs. State detection is accomplished by applying ν^c_{493} and ν^c_{650} for 4.5 ms with saturation parameters of $s \approx 0.1$. 493 nm photons are collected using a 0.28 NA commercial objective and photomultiplier tube (PMT) with approximately 20% quantum efficiency.

Each qubit state is attempted in blocks of 200 consecutive trials, followed by the other qubit state, for a combined total of 217,748 trials. The number of photons detected after each experiment is plotted in Fig. 6.12, and a threshold at $n_{th} \leq 1$ photons maximally discriminates between $|0\rangle$ and $|1\rangle$. Using this hyperfine-selective optical cycling for SPAM, we measure the fraction of events in which an attempt to prepare the $|0\rangle$ state was determined

to be $|1\rangle$, $\epsilon_{|0\rangle} = 3.03(4)\times10^{-2}$, and the fraction of experiments in which an attempt to prepare the $|1\rangle$ state was determined to be $|0\rangle$, $\epsilon_{|1\rangle} = 8.65(9) \times 10^{-2}$. The average SPAM fidelity is = 0.9415(5). Ultimately, the fidelity of this technique is limited by off-resonant excitation to the $|^2\mathrm{P}_{1/2}, F{=}1\rangle$ manifold during readout, which can decay to either $|0\rangle$ or $|1\rangle$, thereby causing misidentification of the original qubit state [OYM07]. In this experiment, readout fidelity could be improved with increased light collection efficiency [NVG13, CCV19] and reduced background counts from laser scatter.

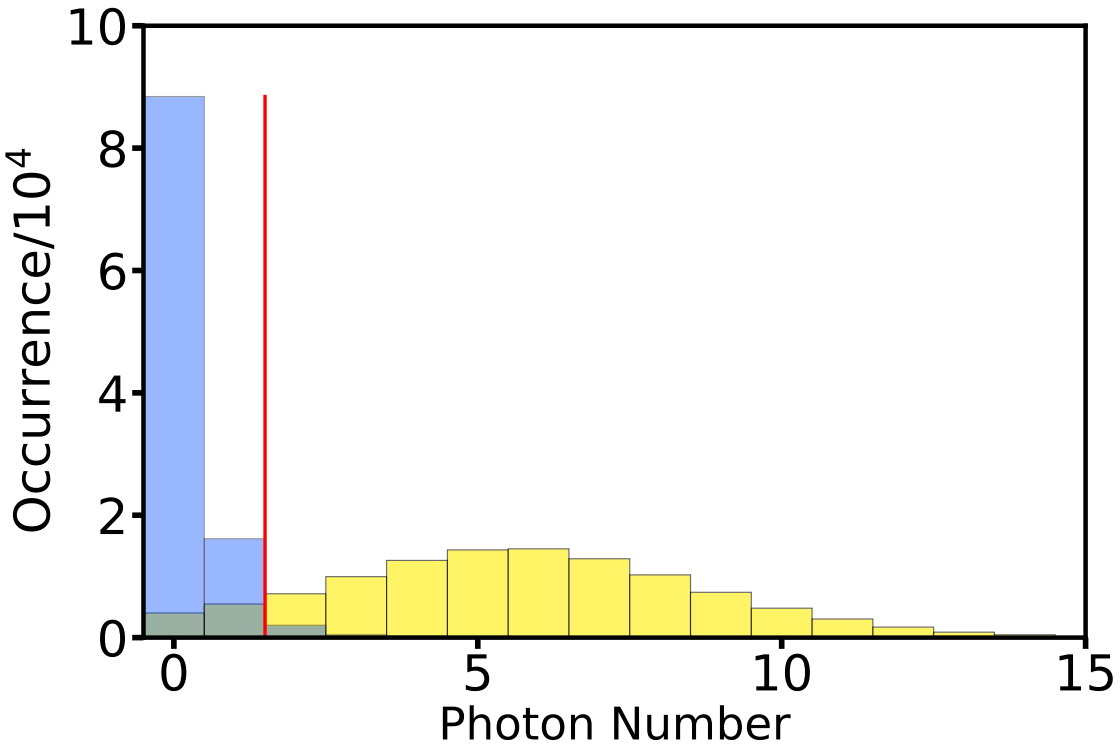

Figure 6.12: Histogram of detected photons during the attempted preparation and measurement of the $|0\rangle$ and $|1\rangle$ qubit states using hyperfine-selective preparation and readout. The fraction of events in which an attempt to prepare the $|0\rangle$ state was determined to be $|1\rangle$ was $\epsilon_{|0\rangle} = 3.03(4) \times 10^{-2}$, and the fraction of experiments in which an attempt to prepare the $|1\rangle$ state was determined to be $|0\rangle$, $\epsilon_{|1\rangle} = 8.65(9) \times 10^{-2}$. The average SPAM fidelity is $\mathcal{F} = 0.9415(5)$

To benchmark SPAM using the highest fidelity optically pumped shelving scheme, state preparation of each qubit state is applied to a single trapped $^{133}\mathrm{Ba}^+$ ion and read out (Fig. 6.13).

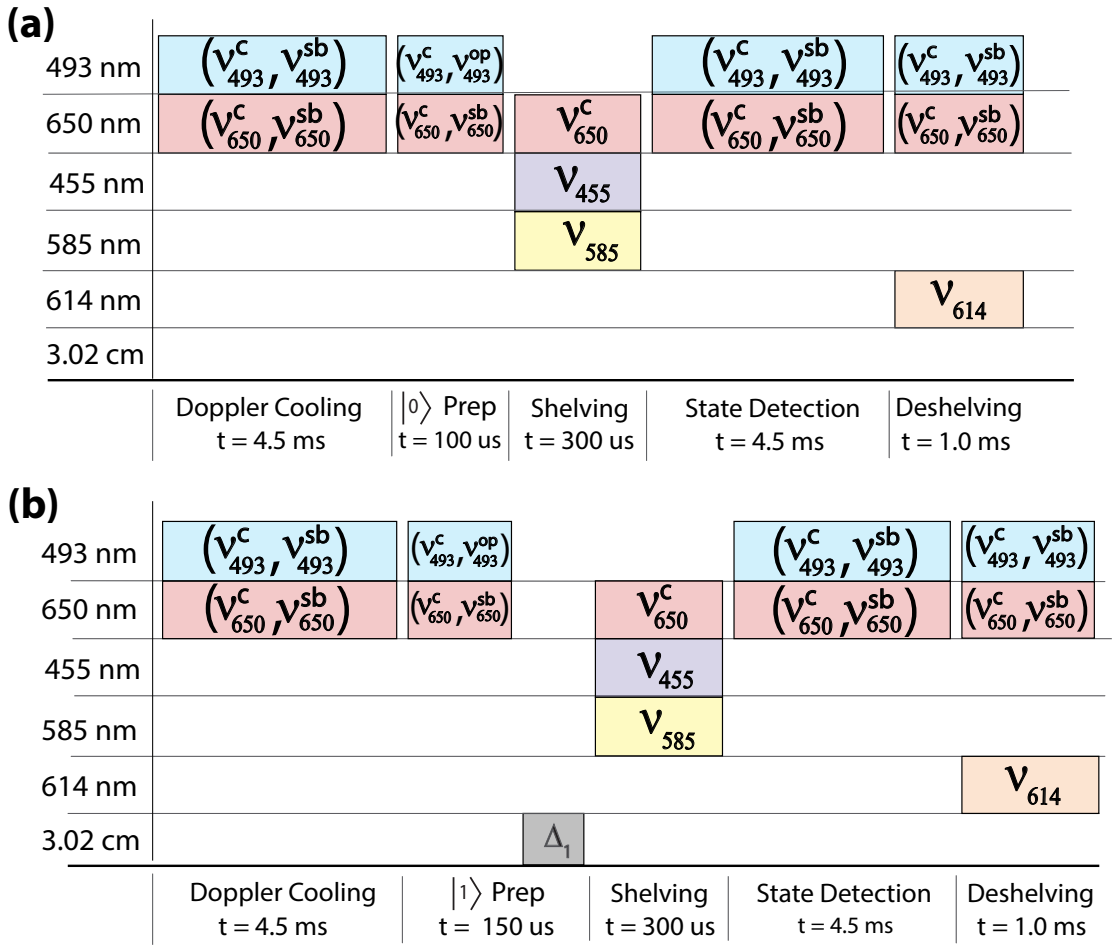

Figure 6.13: Experimental sequence for $|0\rangle$ and $|1\rangle$ SPAM using the electron shelving detection scheme. All lasers are linearly polarized $\approx 45°$ from the magnetic field except the laser near 455 nm (ν_{455}) linearly polarized along the magnetic field (π-light). (a) Sequence for $|0\rangle$ SPAM. (b) Sequence for $|1\rangle$ SPAM.

Before each SPAM attempt, the Doppler cooling fluorescence is monitored to determine if a SPAM attempt can be made using the same protocol as the hyperfine-selective SPAM measurement. The $|0\rangle$ and $|1\rangle$ states are prepared using the same parameters as the hyperfine-selective optical cycling scheme. Electron shelving is accomplished by simultaneously applying three lasers near 455 nm, 585 nm, and 650 nm for 300 μs. The ECDL laser near 455 nm tuned resonant with the $|^2\mathrm{P}_{3/2}\,;F{=}2\rangle \leftrightarrow |^2\mathrm{S}_{1/2}\,;F{=}1\rangle$ transition (ν_{455}) is linearly polarized parallel to the magnetic field (π-light) with saturation parameter $s \approx 1\times10^{-3}$. The ECDL near 1171 nm frequency doubled using a periodically poled lithium niobate (PPLN)

waveguide is tuned resonant with $|^2\mathrm{P}_{3/2};F=2\rangle \leftrightarrow |^2\mathrm{D}_{3/2};F=2\rangle$ transition (ν_{585}). The laser is linearly polarized $\approx 45°$ from the magnetic field direction with saturation parameter $s \approx 1\times10^{-2}$. The ECDL near 650 nm is tuned to the same parameters as Doppler cooling except for the reduction of saturation parameter to $s \approx 1$. Deshelving of the $^2\mathrm{D}_{5/2}$ manifold back to the cooling cycle is accomplished with an ECDL near 1228 nm frequency doubled with a PPLN waveguide and linearly polarized $\approx 45°$ from the magnetic field direction. The frequency is detuned approximately 40 MHz from the $|^2\mathrm{P}_{3/2};F{=}2\rangle \leftrightarrow |^2\mathrm{D}_{5/2};F{=}2\rangle$ transition and applied for 500 μs with saturation parameter $s \approx 1$.

Each qubit state is attempted in blocks of 200 consecutive trials, followed by the other qubit state, for a combined total of 313,792 trials. The number of photons detected after each experiment is plotted in Fig. 6.14, and a threshold at $n_{th} \leq 12$ photons maximally discriminates between $|0\rangle$ and $|1\rangle$. The fraction of events in which an attempt to prepare the $|0\rangle$ state was measured to be $|1\rangle$ is $\epsilon_{|0\rangle} = 1.9(4)\times10^{-4}$, while the fraction of experiments in which an attempt to prepare the $|1\rangle$ state was measured to be $|0\rangle$ is $\epsilon_{|1\rangle} = 3.8(5)\times10^{-4}$. The average SPAM fidelity is $\mathcal{F} = 1-\frac{1}{2}(\epsilon_{|0\rangle}+\epsilon_{|1\rangle}) = 0.99971(3)$.

Table 6.1 provides an error budget with estimates of the individual sources of error that comprise the observed infidelity. In addition to the previously discussed errors, the readout of the $^2\mathrm{S}_{1/2}$ manifold is limited by background gas collisions, characterized by the preparation and readout fidelities of the $^2\mathrm{S}_{1/2}$ and $^2\mathrm{D}_{5/2}$ manifolds in $^{138}\mathrm{Ba}^+$, for which we achieve $\mathcal{F} = 0.99997(1)$. The state readout duration is determined by the need to separate the $|0\rangle$ and $|1\rangle$ state photon distributions. Our limited numerical aperture requires detection for 4.5 ms, leading to an error due to spontaneous emission from the $^2\mathrm{D}_{5/2}$ state of $\epsilon \approx 1.5\times10^{-4}$. This could be reduced with maximum likelihood methods [Lan06, MSW08] or higher efficiency light collection [NVG13].

It should be possible to further improve the fidelity to $\mathcal{F} > 0.9999$. Errors due to $|0\rangle \rightarrow |1\rangle$ state transfer and spontaneous emission during readout could be reduced with higher fidelity population transfer and improved light collection efficiency [HAB14, NVG13]. The shelving fidelity could be improved using a pulsed shelving scheme [MSW08], or by addition

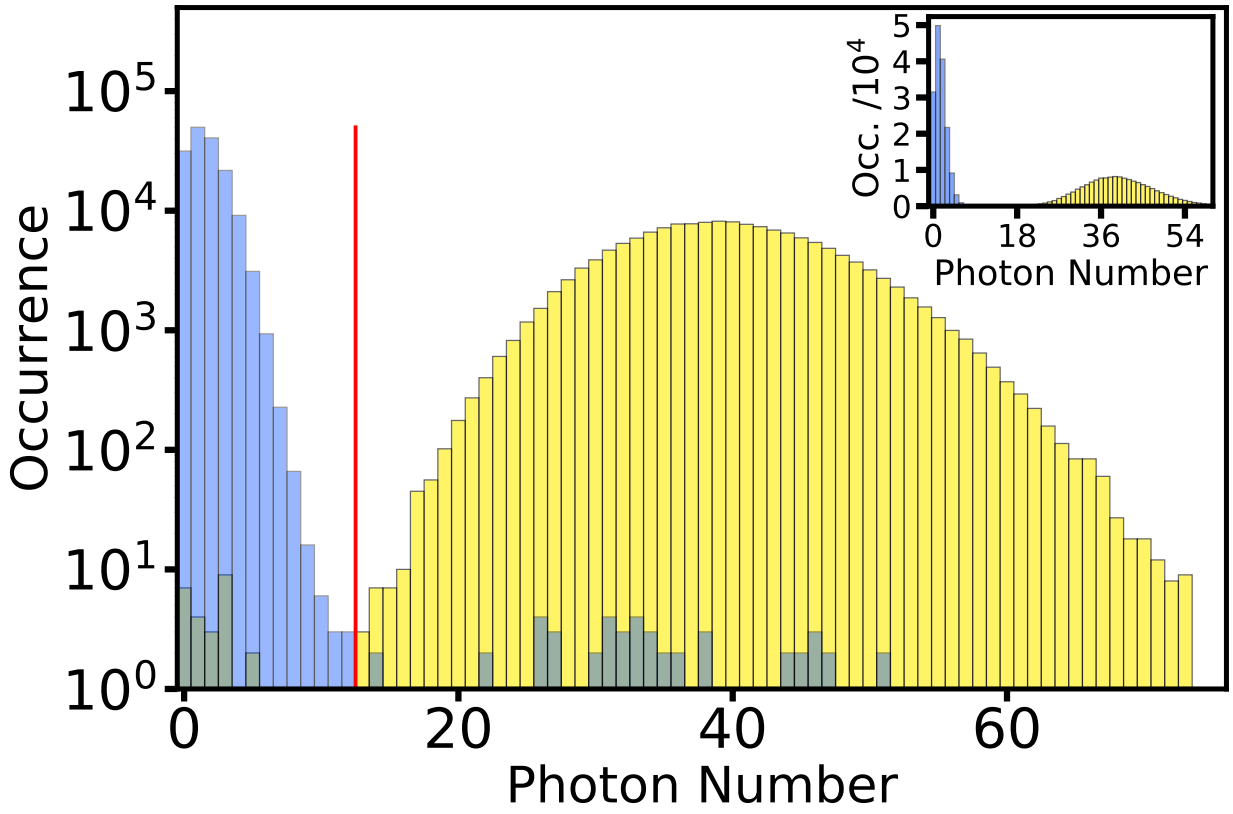

Figure 6.14: Histogram of detected photons using high-fidelity electron shelving state detection.

of a 1762 nm transfer step before optical pumping (Fig. 6.2). Optical-frequency qubit manipulations have been demonstrated (in other species) with a π-pulse fidelity of $\mathcal{F} = 0.99995$ [GTL16], suggesting that high-fidelity, unitary transfer to $^2D_{5/2}$ may be possible. With population first transfered via 1762 nm, followed by the optically-pumped shelving scheme, infidelity below 10^{-6} should be achievable.

6.5 Summary

High-fidelity qubit operations have been demonstrated using a composite pulse sequence and optically-pumped electron shelving state detection. A measured average single-shot SPAM fidelity of $\mathcal{F} = 0.99971(3)$ is the highest reported value to date on any qubit platform.

Currently, implementing fault-tolerant error correction is still too resource intensive given

Process	Average error $\times 10^{-4}$
Initialization to $\|0\rangle$	0.1
Off-resonant shelving $\|0\rangle$	1.0
Readout of $^2S_{1/2}$ manifold	0.1
$\|0\rangle \rightarrow \|1\rangle$ CP Robust 180 sequence	0.5
Shelving $\|1\rangle$	1.0
Spontaneous decay during readout	0.5
Total average SPAM error	3.2

Table 6.1: Experimental error budget for state preparation and measurement (SPAM) of the $^{133}Ba^+$ hyperfine qubit. Errors are estimates based on theoretical models and auxiliary experiments. The $|0\rangle$ state SPAM is limited by off-resonant scatter from the laser used for electron shelving. The $|1\rangle$ state electron shelving is limited by the $^2P_{3/2}$ hyperfine splitting, where off-resonant scatter can cause spontaneous emission to the $|0\rangle$ state. Spontaneous emission of the $^2D_{5/2}$ state and preparation of the $|1\rangle$ state via microwaves are the next largest contribution to the $|1\rangle$ state SPAM error.

the best demonstrated single and two-qubit gate fidelities. Without fault-tolerant error correction, single-shot preparation and readout fidelity of multiple qubits is exponentially dependent on qubit number $\mathcal{F} = (1-\epsilon)^N$. The results presented here provide a path to increased fidelities for multi qubit experiments. The largest system to date has demonstrated readout of 53 qubits with only 99% individual SPAM fidelities, giving a total single-shot SPAM fidelity of $\approx 59\%$. While the individual readout fidelities presented may decrease in multi qubit systems, we still expect improved total readout fidelity in large qubit systems given the advantageous electronic structure of $^{133}Ba^+$.

A clear path for improving SPAM in $^{133}Ba^+$ is possible with the addtion of a laser near 1762 nm. A Stable Laser Systems cavity for 1762 nm stabilization has recently been installed with a quoted linedwidth of < 1 Hz at 1 s. In addition, we expect improved single qubit gate fidelity, as well as demonstrated high-fidelity two qubit gates with the addition of a laser

near 532 nm allowing stimulated Raman transitions.

APPENDIX A

Radioactive Details

A.1 Activity and Shielding

The radioactive isotope ^{133}Ba has a half-life of 10.51(5) years [ABB04] and decays via electron capture to produce ^{133}Cs:

$$p + e^- \longrightarrow n + \nu_e.$$

The main safety concerns are from the resulting decay of metastable ^{133m}Cs states producing gamma rays with photon energies give in Table A.1. The gamma dose constant is listed as 2.4 mR/hr per 1 mCi at 30 cm, meaning the dose rate in one hour is 2.4 mR from a 1 mCi source at a distance of 30 cm [ucs]. The Currie is defined as 1 Ci = 3.7×10^{10} decays/sec = 3.7×10^{10} (Bq), and 1 Bq is 1 decay/sec. The maximum dosage for a radiation safety worker in the United States is 5000 mR/yr, and the average dose a person living in the united states receives annually is $\approx$ 620 mR [nrc]. To alleviate more stringent radiation safety requirements and keep lab personal well within safety limits, we chose to work with a maximum activity of 1 mCi at any given time.

A Beer's law equation is used to calculate the shielding required to attenuate a given source, and is given by:

$$R = R_0 e^{-\frac{\mu}{\rho}x} \tag{A.1}$$

where μ is the linear attenuation coefficient, a function of the photon energy, R_0 the unshielded dose rate, and ρ the density of the shielding material. Figure A.1 shows the attenuation coefficient μ/ρ for lead over the photon energy of interest. If we assume the dedicated graduate student spends 20 hours a day in the lab every day of the year, and is always 30

E (keV)	per 100 Decays
81	31.06
303	18.33
356	62.05

Table A.1: Dominant gamma ray energies and intensities resulting from the decay of $^{133}Ba^{+}$ [ucs, SAD16].

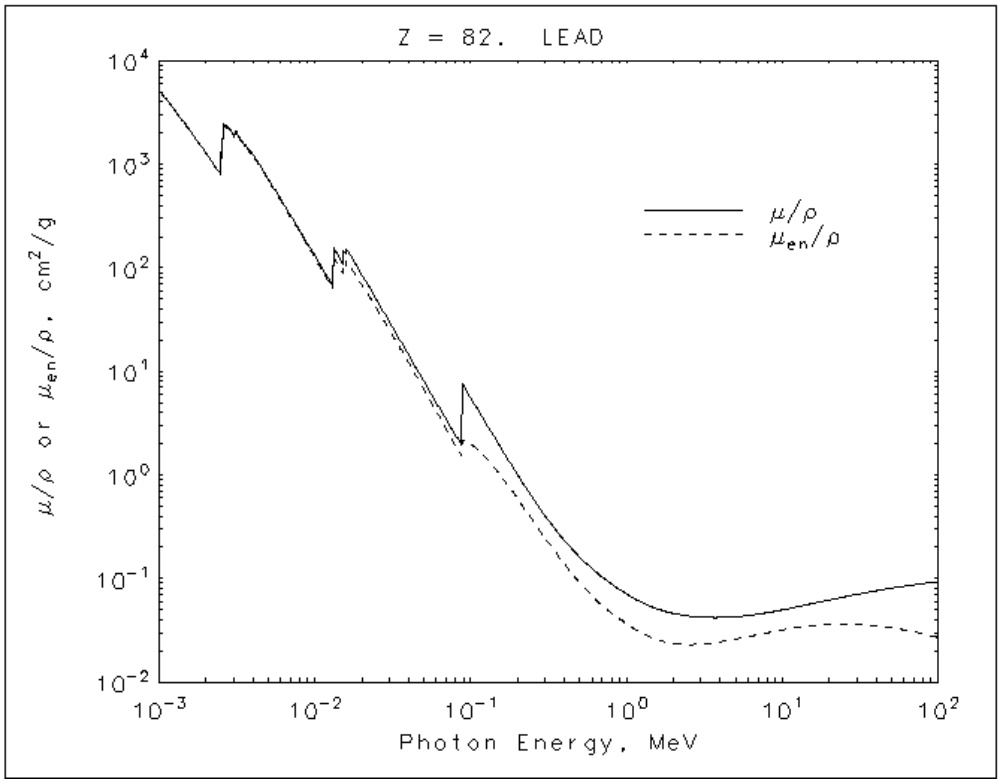

Figure A.1: Absorption coefficient of lead as a function of photon energy [nis].

cm away from a 1 mCi source, than they would need attenuate the does rate by a factor of 30 to receive the same dose as the average person per year. Using equation A.1 and figure A.1 to estimate the attenuation coefficient (0.4) for the largest gamma ray energy of $\approx$ 350 keV, a lead thickness of 1 cm attenuates the dose rate by a factor of 100. Since even the most enthusiastic grad student probably won't be sleeping with the source, this amount of shielding is more than sufficient. The radiation safety departments at UCLA provided lead

bricks which surrounds the majority of the experiment (Fig. A.2).

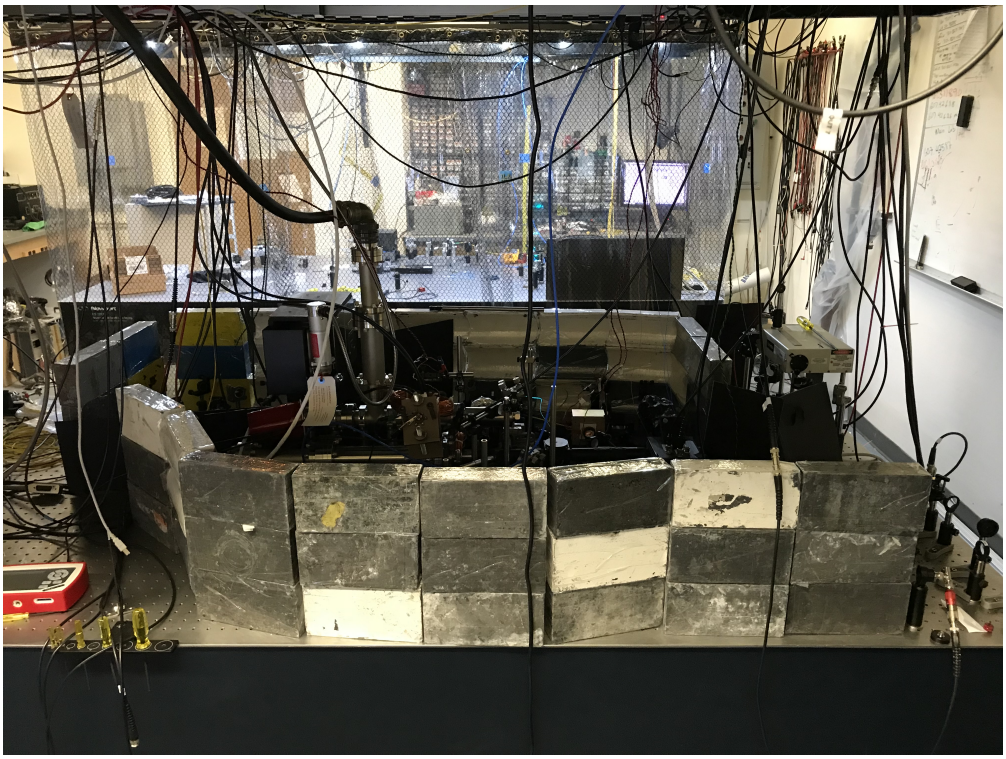

Figure A.2: Vacuum chamber surrounded by lead bricks provided by UCLA.

The number of atoms in 1 Ci depends on the decay constant λ which is specific to each radioactive species:

$$N_{atoms} = \frac{3.7 \times 10^{10}\text{Bq}}{\lambda}. \tag{A.2}$$

The half-life (τ) is often given instead of the decay constant, and a straight-forward calculation using the general decay rate equation can be used to calculate it:

$$\lambda = \frac{log(2)}{\tau_{1/2}}. \tag{A.3}$$

Using the half-life for barium-133, the number of atoms in a 1 mCi source is $N_{atoms} \approx 1 \times 10^{16}$.

A.2 $^{133}Ba^{+}$ Production and Availability

^{133}Ba is produced by various methods including cyclotron bombardment of Xenon gas with alpha particles, proton or dueteron bombardment of cesium, or neutron bombardment of

^{132}Ba [Nei77, CPL57]. Our source is purchased from Eckert & Ziegler [EZ] and is manufactured via neutron bombardment of ^{132}Ba. Production runs may last up to several years which allows for accumulation of both ^{133}Ba and ^{133}Cs, and the company states they have no control over the amount of ^{133}Cs in a purchases source. In addition, the company adds naturally abundant Ba to their sources. When purchasing from Eckert & Ziegler a request can be made for the highest specific activity and no additional barium, "carier" is the company term, added. Sources are only available as $BaCl_2$ dissolved in 0.1M HCl, and ordering the smallest quantity of liquid (1 ml) is best for making a target for loading ions. Figure A.3 shows a source purchased from Eckert & Ziegler. ^{133}Ba can also be purchased from Oakridge

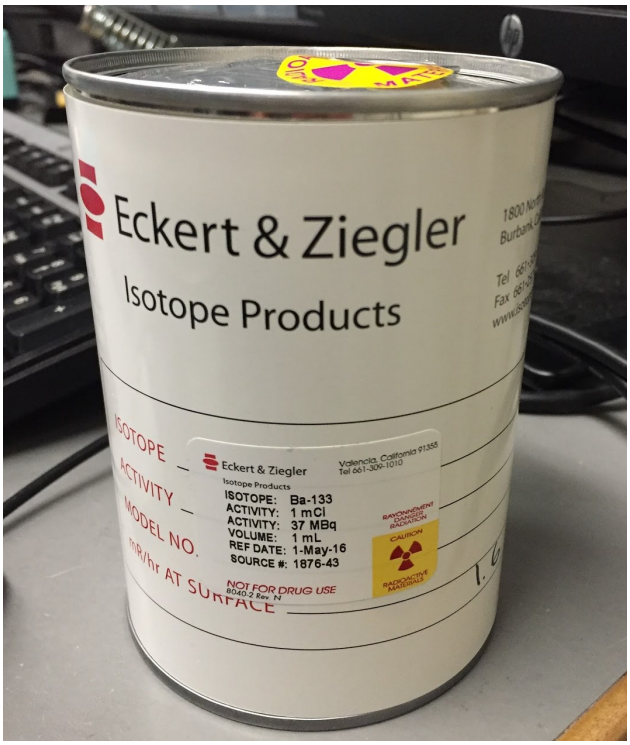

Figure A.3: $^{133}Ba^{+}$ source purchased from Eckert & Ziegler

National Laboratories, and for an additional fee will chemically remove any ^{133}Cs present.

A.3 Handling and Dosimetry

Dosimetry chest badges and rings are provided by the radiation safety department at UCLA, and a Ludlum 3 rate meter with sodium iodide probe (model 44-2) is kept in the lab to monitor for contamination. In addition, a personal radiation dose meter (RAD-60R) is worn whenever handling ^{133}Ba, including production of a source for loading ions. Transfer of radioactive material is done inside a glove tent (Fig. A.4) and moved into a fume hood for production of an ion source.

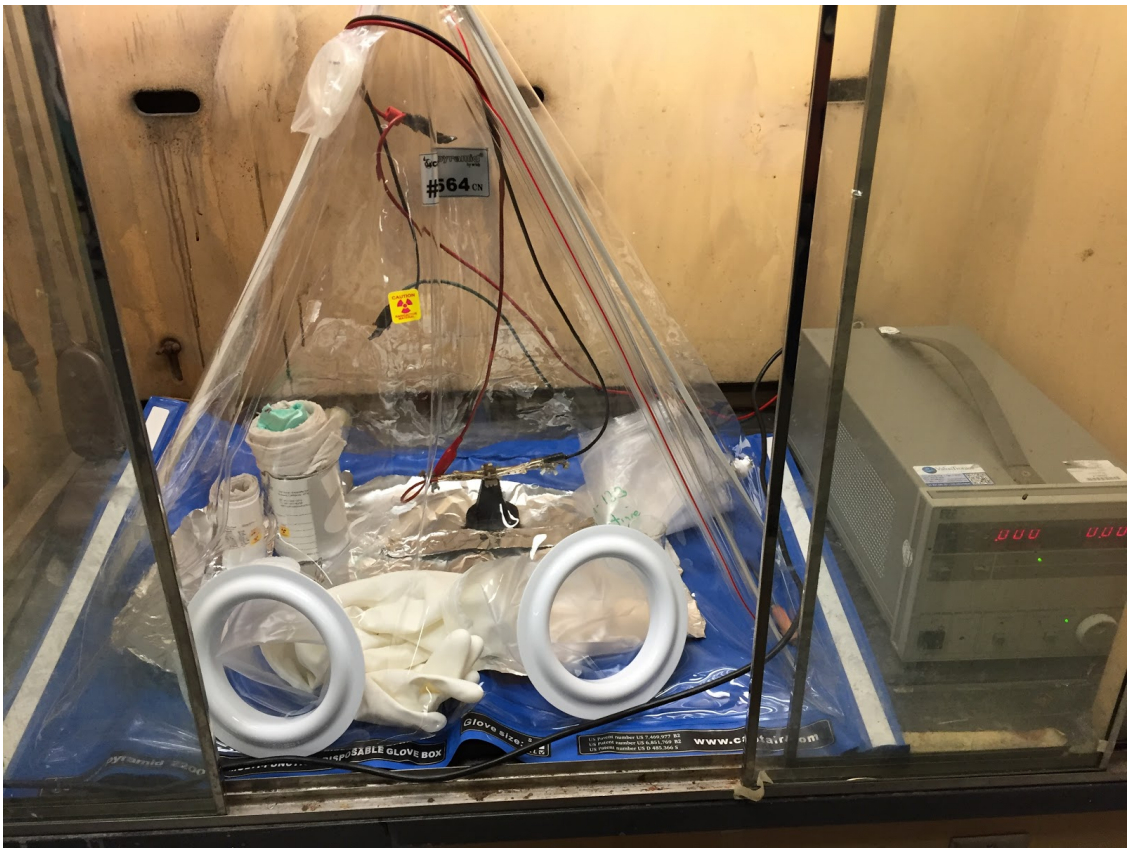

Figure A.4: Glove tent inside of a fume hood used to produce a $^{133}Ba^{+}$ ion source.

APPENDIX B

Mathieu Equations and Stability Diagram

Solutions to the Mathieu equations 2.14 led to the recursion relationship:

$$C_{2n+2,i} + D_{2n,i}C_{2n,i} + C_{2n-2,i} = 0 \tag{B.1}$$

and the question of solving an infinite determinant (Eq 2.2). A solution formed by Timothy Jones [Jon08] was followed to determine stable solution as a funtion of a_i and q_i, and his C code modified to generate stability diagrams in Python.

```
import numpy as np
import matplotlib.pyplot as plt
a = np.arange(-.3,.3,.001)
q = np.arange(0,1.0,.001)
gamma = np.zeros(101)
dets = np.zeros(len(gamma))
#z = np.ones((len(a)*len(q), 3))
z1 = np.ones((len(a),len(q)))
det_error = np.zeros(len(a)*len(q))
for i in range(len(a)):
    for j in range(len(q)):
        for k in range(len(gamma)):
            # Here my definition is slightly different than Timothy's
            # I use the index i while his index is 2*i
            gamma[k] = q[j]/((2*k)**2 - a[i])

        #print gamma[-20:-1]
        # Next need to calculate seed determinants
        d0 = np.array([1])
```

```
d1 = np.array([[1, gamma[1], 0 ], [gamma[0], 1, gamma[0]], \
        [0, gamma[1], 1]])

d2 = np.array([[1, gamma[2], 0, 0, 0], [gamma[1], 1, gamma[1], \
        0, 0], [0, gamma[0], 1, gamma[0], 0], [0, 0, \
        gamma[1], 1, gamma[1]], [0, 0, 0, gamma[2], 1]])

'''
d3 = np.array([[1, gamma[3], 0, 0, 0, 0, 0], [gamma[2], 1, \
        gamma[2], 0, 0, 0, 0], [0, gamma[1], 1, gamma[1], \
        0, 0, 0], [0, 0, gamma[0], 1, gamma[0], 0, 0], \
        [0, 0, 0, gamma[1], 1, gamma[1], 0],\
        [0, 0, 0, 0, gamma[2], 1, gamma[2]], \
        [0, 0, 0, 0, 0, gamma[3], 1]])
'''
dets[0] = 1 # np.linalg.det(d0), doesn't like this
dets[1] = np.linalg.det(d1)
dets[2] = np.linalg.det(d2)
#dets[3] = np.linalg.det(d3)

for k in range(3,len(gamma)):
    alpha = gamma[k]*gamma[k-1]
    beta = 1-alpha
    alpha1 = gamma[k-1]*gamma[k-2]

    dets[k] = beta*dets[k-1] - alpha*beta*dets[k-2] +  \
    alpha*alpha1**2*dets[k-3]



if a[i] > 0:
    mu = np.arccos(1-dets[len(dets)-1]* \
        (1-np.cos(np.pi*np.sqrt(a[i]))))/np.pi
```

```
        else:
            mu = np.arccos(1-dets[len(dets)-1]* \
                (1-np.cosh(np.pi*np.sqrt(abs(a[i])))))/np.pi


        if np.isreal(mu) != True or np.isnan(mu) == True:
            mu = 0

        #row = len(q)*i + j
        #z[row,0] = a[i]
        #z[row,1] = q[j]
        #z[row,2] = mu
        z1[i,j] = mu

        #det_error[row] = (abs(dets[-2] - dets[-1]))/dets[-1]

## For Plotting only
#print np.amax(det_error)
Qx ,Ax = np.meshgrid(q,-a)
Qy ,Ay = np.meshgrid(q, a)
Cx = plt.contour(Qx,Ax,z1, levels = np.arange(0.005,1.05,.05))

plt.clabel(Cx, fontsize = 8, inline = 1)
plt.xlabel(r'$q_{x,y}$', fontsize = 24)
plt.ylabel(r'$a_{x,y}$', fontsize = 24)
plt.xlim([0,.9])
plt.ylim([-.28,.3])
plt.xticks(fontsize = 24)
plt.yticks(fontsize = 24)

Cy = plt.contour(Qy,Ay,z1, levels = np.arange(0.005,1.05,.05))
plt.clabel(Cy, fontsize = 8, inline = 1)
```

To find the stability region in three dimensions, we simply need to scale a_z and q_z using the relationship:

$$a_z = 2a_{x,y} \quad q_z = 2q_{x,y}.$$

Then the same code as above can be used. Finally we'd like to fit a polynomial to the boundary of the region of overlap in the a and q plane. This will allow us to easily determine when an ion is in the stability region (2D case below):

```
from scipy.optimize import curve_fit

# Polynomial to fit the lines to
def my_fit(x, a, b, c, d, e):
    return a + b*x + c*x**2 + d*x**3 + e*x**4

level = Cx.levels
#print level
cs = Cx.collections[2]  # indice of level is indice with contour data
# paths are contour xy data.
# single contour is 2 paths, split around the label
paths = cs.get_paths()
#print len(paths)
path0 = paths[2]
path1 = paths[3]
x_edge20 = path0.vertices
x_edge21 = path1.vertices
x1x = np.append(x_edge20[:,0],x_edge21[:,0])
x1y = np.append(x_edge20[:,1], x_edge21[:,1])

cs1 = Cx.collections[19]
paths = cs1.get_paths()
#print len(paths)
path0 = paths[2]
path1 = paths[1]
x_edge20 = path0.vertices
x_edge21 = path1.vertices
```

```
x2x = np.append(x_edge20[:,0],x_edge21[:,0])
x2y = np.append(x_edge20[:,1], x_edge21[:,1])
plt.plot(x1x, x1y, color = 'k', linewidth = 3)
plt.plot(x2x, x2y, color = 'k', linewidth = 3)


"""
fit_x1 = curve_fit(my_fit, x1x, x1y)
print fit_x1[0]
x = np.linspace(x1x[0], x1x[-1], 1e2)
y = my_fit(x, fit_x1[0][0],fit_x1[0][1], \
fit_x1[0][2],fit_x1[0][3], fit_x1[0][4])
plt.plot(x,y, color = 'r', linestyle = '--')


fit_x2 = curve_fit(my_fit, x2x, x2y)
print fit_x2[0]
x2 = np.linspace(x2x[0], x2x[-1], 1e2)
y2 = my_fit(x2, fit_x2[0][0],fit_x2[0][1], \
fit_x2[0][2],fit_x2[0][3], fit_x2[0][4])

plt.plot(x2,y2, color = 'r', linestyle = '--')
"""
#np.savetxt("x_stable1.txt", np.column_stack((x1x,x1y)))
#np.savetxt("x_stable2.txt", np.column_stack((x2x,x2y)))

level = Cy.levels
#print level
cs = Cy.collections[2]
paths = cs.get_paths()
#print len(paths)
path0 = paths[2]
path1 = paths[3]
y_edge20 = path0.vertices
```

```
y_edge21 = path1.vertices
y1x = np.append(y_edge20[:,0],y_edge21[:,0])
y1y = np.append(y_edge20[:,1], y_edge21[:,1])

cs = Cy.collections[19]
paths = cs.get_paths()
#print len(paths)
path0 = paths[2]
path1 = paths[1]
y_edge20 = path0.vertices
y_edge21 = path1.vertices
y2x = np.append(y_edge20[:,0],y_edge21[:,0])
y2y = np.append(y_edge20[:,1], y_edge21[:,1])

#np.savetxt("y_stable1.txt", np.column_stack((y1x,y1y)))
#np.savetxt("y_stable2.txt", np.column_stack((y2x,y2y)))
plt.plot(y1x, y1y, color = 'k', linewidth = 3)
plt.plot(y2x, y2y, color = 'k', linewidth = 3)



plt.xlabel('q', fontsize = 20)
plt.ylabel('a', fontsize = 20)
plt.tick_params(labelsize = 20)
plt.tick_params(width=5, length=10)

plt.show()
```

Figure 2.5 in the main text shows the fitted boundary region and gives the fit parameters.

APPENDIX C

Langevin Capture Theory

The collision rate is often modeled using Langevin capture theory, which describes the ion induced-dipole coupling between a charged particle and polarizable neutral atom or molecule. Within a critical impact parameter b_c, the neutral spirals into the ion and the assumed probability of a reaction/collision is one. Below, the reaction rate constant is derived, which can then be used to predict the collision rate between a trapped atomic ion and a neutral background particle. This problem is analogous to the two-body central force problem described in classical mechanics texts, and the approach here will be the same. Starting with the Lagrangian we have:

$$\mathcal{L} = \frac{1}{2}\mu(\dot{r}^2 + \dot{\phi}^2 r^2) - U(r)$$

with

$$U(r) = -\vec{P} \cdot \vec{E}.$$

$\vec{P}$ is the dipole moment of the neutral atom or molecule, and $\vec{E}$ the electric field produced by the ion. If we assume linear media:

$$\vec{P} = \alpha \vec{E}$$

where α is the polorizability of the atom/molecule. The potential then energy becomes:

$$U(r) = -\frac{\alpha e^2}{16\pi^2 \epsilon_0^2 r^4}.$$

For each generalized coordinate we have:

$$\frac{\partial \mathcal{L}}{\partial q} = \frac{d}{dt}\frac{\partial \mathcal{L}}{\partial \dot{q}}.$$

For the radial coordinate we get:

$$\mu\ddot{r} = \mu\dot{\phi}^2 r - \frac{\alpha e^2}{4\pi^2\epsilon_0^2 r^5}$$

and for the angular coordinate we get:

$$\mu\dot{\phi}r^2 = L$$

where L represents the angular momentum, and is a constant. Using the angular equation to eliminate the angular variable in the radial equation, we have:

$$\mu\ddot{r} = \frac{L^2}{\mu r^3} - \frac{\alpha e^2}{4\pi^2\epsilon_0^2 r^5}.$$

From this we want to extract the effective potential and analyze its form. Since:

$$F = -\frac{dU_{eff}}{dr}$$

we have:

$$U_{eff} = \frac{L^2}{2\mu r^2} - \frac{\alpha e^2}{16\pi^2\epsilon_0^2 r^4}.$$

Initially we assume the two particles are far enough away that $U_{eff} = 0$. Then the total energy is just the initial kinetic energy.

$$E_{tot} = \frac{1}{2}\mu v_0^2.$$

We define the impact parameter as:

$$b = r sin\theta$$

which can be related to the angular momentum by:

$$L = \vec{r} \times \vec{p} = r\mu v_0 sin\theta = \mu v_0 b.$$

We can now replace the angular momentum term in the effective potential:

$$U_{eff} = \frac{(\mu v_0 b)^2}{2\mu r^2} - \frac{\alpha e^2}{16\pi^2\epsilon_0^2 r^4}$$

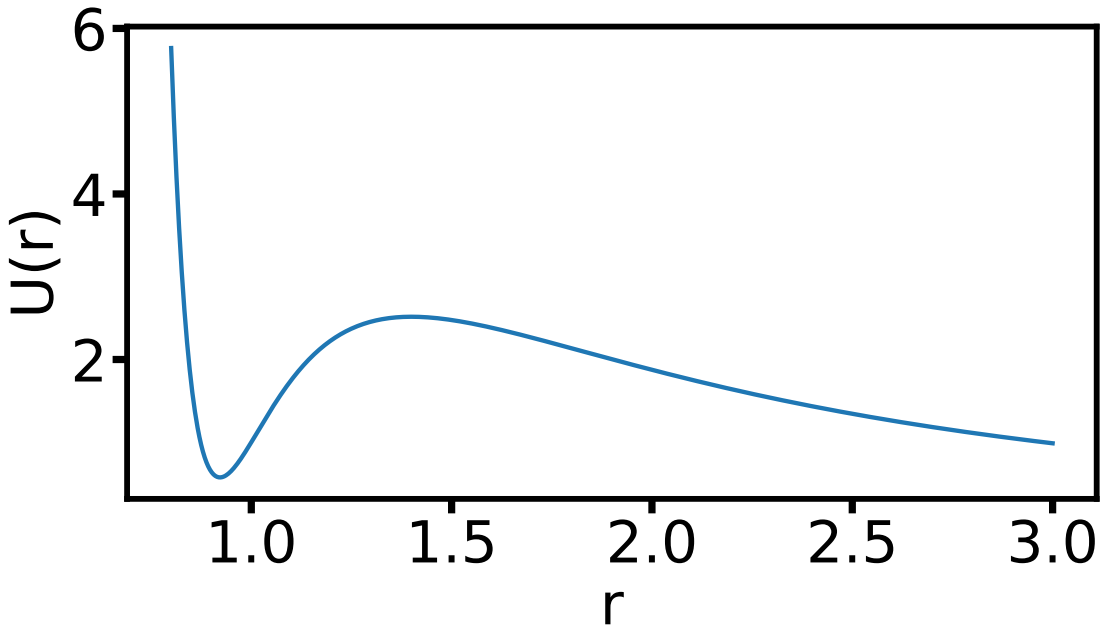

Figure C.1: Effective potential vs ion-neutral distance in an ion induced-dipole interaction between a charged ion and a polarizable neutral atom or molecule.

and we can replace the velocity term with the initial kinetic energy:

$$U_{eff} = \frac{E_{KE_0} b^2}{r^2} - \frac{\alpha e^2}{16\pi^2 \epsilon_0^2 r^4}.$$

An effective potential may look like Figure C.1 which includes a $\frac{1}{r^{12}}$ nuclear repulsion term. In order for the ion and neutral to get close enough to react, they must overcome the potential barrier, the height of which depends on the impact parameter and the kinetic energy. In the Langevin theory once this barrier is overcome, the probability to react is one. Finding the maximum and where it occurs:

$$\frac{dU}{dr} = -\frac{2E_{KE_0} b^2}{r^3} + \frac{\alpha e^2}{4\pi^2 \epsilon_0^2 r^5} = 0$$

$$r_0 = \sqrt{\frac{\alpha e^2}{8E_{KE_0} \pi^2 \epsilon_0^2 b^2}}$$

$$U_{max}(r_0) = \frac{4\pi^2 \epsilon_0^2 E_{KE_0}^2 b^4}{\alpha e^2}.$$

A large impact parameter means a large angular momentum, and the large "centrifugal force" prevents the particle from falling towards the center. The same is true for a large kinetic energy, increasing the angular momentum, and increasing the height of the potential barrier. In order to overcome the potential barrier, the total energy of the particle must be greater than or equal to the maximum barrier height. By setting the height of the potential barrier equal to the total energy, the initial kinetic energy, we can solve for the critical impact parameter.

$$b_c = \left(\frac{\alpha e^2}{4\pi^2 \epsilon_0^2 E_{KE_0}} \right)^{1/4}.$$

With the critical impact parameter we can now define the cross section:

$$\sigma = \pi b_c^2 = \left(\frac{\pi \alpha e^2}{4\epsilon_0^2 E_{KE_0}} \right)^{1/2}$$

or back in terms of the initial velocity v_o

$$\sigma(v) = \left(\frac{\pi \alpha e^2}{2\epsilon_0^2 \mu v_0^2} \right)^{1/2}.$$

To determine the reaction rate, we imagine an infinitesimally thick slab of space, where the number of particles in that volume is given by:

$$N = \rho A_0 dx$$

with ρ the number density, A_0 the area of the slab, and dx the thickness. The total scattering area is the number of particles times the cross section:

$$A_{scatt} = \sigma(v) \rho A_0 dx$$

and the probability that a scattering event occurs is the scattering area divided by the total area of the slab:

$$dP = \sigma(v) \rho dx.$$

We can write this in terms of velocity by multiplying by $\frac{dt}{dt}$:

$$dP = \sigma(v) \rho v dt.$$

The average number of ions that experience a collision per unit time, is the probability of a collision multiplied by the number of ions in the system:

$$\frac{dN_i}{dt} = (\sigma(v)\rho v)N_i.$$

In chemistry, reaction rates are defined per unit density. Assuming a single ion, we have for the rate constant:

$$\Gamma = \sigma(v)v.$$

Finally, we consider that the particles have a Maxwell-Boltzmann velocity distribution. To find the average reaction rate, we need to integrate over this distribution:

$$\Gamma = \int_0^\infty v\sigma(v)f(v)dv.$$

However, plugging in our cross section we see that the velocities cancel out:

$$\Gamma = \left(\frac{\pi\alpha e^2}{2\epsilon_0^2\mu}\right)^{1/2} \int_0^\infty f(v)dv$$

and the integral equal to one. The final calculated rate constant is:

$$\Gamma = \left(\frac{\pi\alpha e^2}{2\epsilon_0^2\mu}\right)^{1/2}.$$

The surprising result is that the rate does not depend on temperature.

APPENDIX D

Thermionic Emission

Various methods exist for producing singly charged particles for confinement, not limited to resonant enhanced multi-photon ionization (REMPI), laser ablation, and electron-impact ionization. REMPI is commonly chosen in trapped-ion quantum information experiments since it allows precision control of the ionization rate and region. Laser ablation and electron impact ionization are less common, as the large flux of stray charges produced on nearby insulators can create stray fields at the trap center, requiring large compensation voltages to null. Another, perhaps forgotten technique, is the process of thermionic emission.

Thermionic emission is the production of charges from a heated substrate. In the event an atom on a metal surface possesses and ionization energy ($\mathcal{E}$) lower than the metal's work function (Φ), desorption by heating results in a free atomic ion. The ratio of ions (n_i) to neutrals (n_n) desorbing from a metal surface is given by the Saha-Langmuir equation:

$$\frac{n_i}{n_n} = \frac{g_i}{g_n} e^{\frac{\Phi - \mathcal{E}}{kT}} \tag{D.1}$$

where g_i and g_n are the degeneracies of the ion an neutral ground states.[1] Many alkali and alkali-earth species have ionization energies less than effective work functions [KMM00] ($\Phi - \mathcal{E} \geq 1$ eV) of readily obtainable common metals (Pt, Re, W). A ratio $\frac{n_i}{n_n} \gg 1$ can readily be achieved with $\Phi - \mathcal{E} \approx 0.3$ eV and T = 500 K, temperatures easily achieved with resistive heating using thin metal filaments or wires.

Thermionic emission provides the advantage of simplicity, directly producing multiple species from a single source by heating a metal substrate. Previous ground state hyperfine

[1] Negative ions are also produced via thermionic emission, described by equation D.1 with the electron affinity (EA) replacing the ionization energy [HEG95].

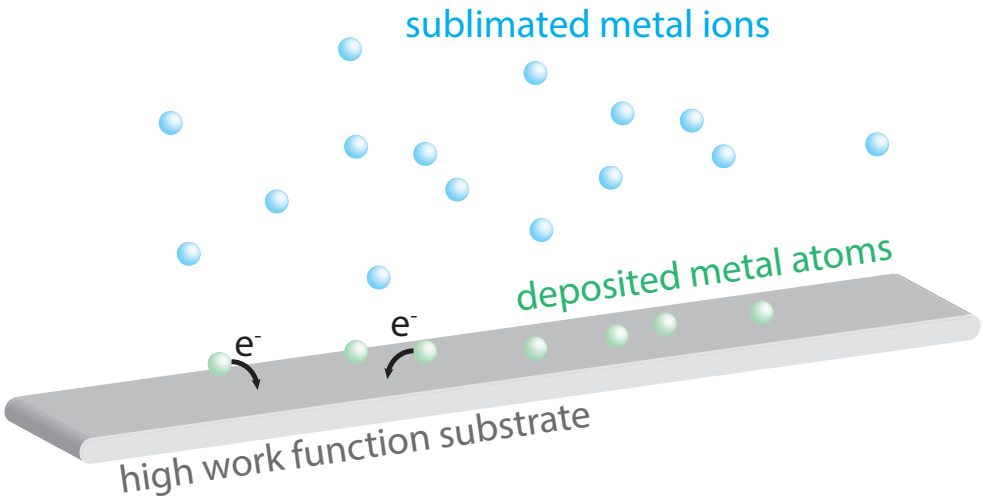

Figure D.1: Depiction of thermionic emission. The majority of atoms with ionization energy $\mathcal{E}$ desorbing from a metal surface with work function Φ will leave singly charged if $\mathcal{E} < \Phi$.

spectroscopy on $^{137}Ba^{+}$, $^{135}Ba^{+}$, and $^{133}Ba^{+}$ have demonstrated the utility of this technique for loading ions [KSW87, BW82, BB81]. A platinum filament impregnated with barium atoms and placed inside an RF Paul trap loaded $\approx 10^5$ ions per attempt after heating to 1200 °C. In particular, for a radioactive source of ^{133}Ba atoms, impregnation in the bulk of a metal provides an easy to transport, non-reactive, confined stable source.

In what follows, we describe preparation of a thermionic source of barium ions using a platinum filament, applicable to various atomic species and metal substrates. After, spectra of various atomic species are presented followed by results for loading ions into an RF Paul trap.

D.1 Source Preparation

A list of materials and atomic sources purchased for construction of platinum and rhenium thermionic sources are given in Table D.1. Platinum strips are cut approximately 1.5 mm x 10 mm, Figure D.2, with homogeneous heating requiring an approximately uniform width. Each strip is cleaned with acetone in an ultrasonic cleaner for 30 minutes before impregnation.

Item	Details	Manufacture
Platinum Foil	0.125 mm, 99.9%	Sigma Aldrich
Rhenium Foil	0.1 mm, 99.97%	Alft Aesar
Constantan Foil	.001" x 2.94" x 5.46"	ESPI Metals
Barium Chloride	99.999% anhydrous	Sigma Aldrich
Strontium Chloride	99.99% anhydrous	Sigma Aldrich
Calcium Chloride	97% anhydrous	Sigma Aldrich
Yb Metal	99.9%	Sigma Aldrich

Table D.1: List of materials and atomic sources purchased for construction of platinum and rhenium thermionic sources.

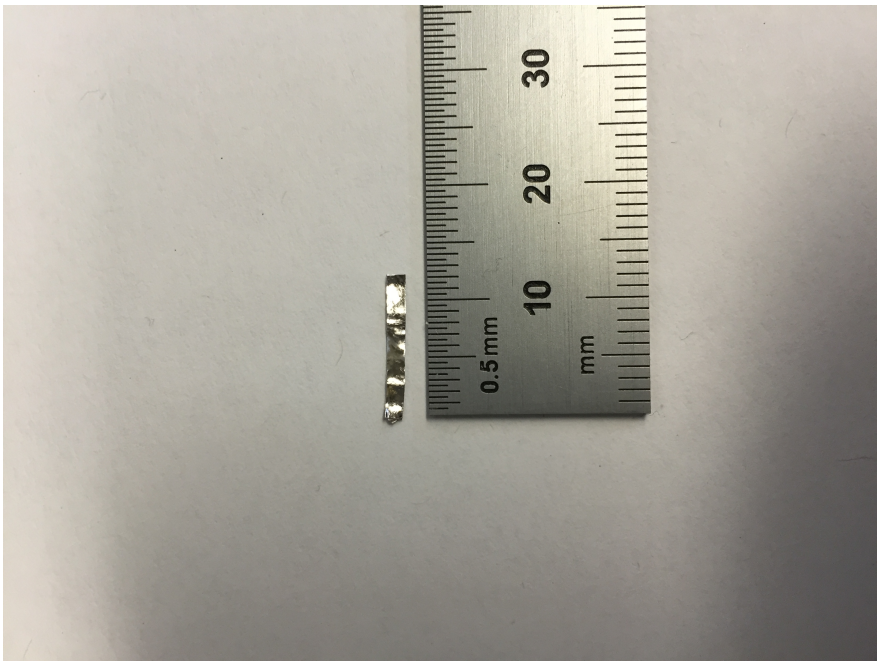

Figure D.2: Cut strip of Pt for use as a thermionic source. Dimensions are $\approx$ 1.5 mm $\times$ 10 mm $\times$ 0.1 mm. Uniform resistive heating requires a relatively constant width.

To impregnate the atom of choice, a mortar and pestle is used to grind 300-400 mg of the

corresponding chloride salt into a powder (for Yb, small pieces of metal are used). Alligator clips connected to a power supply hold the platinum (same procedure for Rhenium) at each end such that the wide surface is parallel to the table, Figure D.3. A layer of ground salt is deposited on the platinum and approximately 20 A of current runs through the strip until it develops an orange-white color. This causes the salt to melt and wick over the platinum strip. The current turns off after approximately one minute, and upon cooling a thin layer of the salt typically remains. A tissue removes the remaining bulk salt, and no additional cleaning is preformed.

Figure D.3: To impregnate the salt or metal of interest, a filament is connected to a power supply via aligator clips, and salt deposited on the surface. A current of up to 20 A heats the filament to an orange-white color for 1 min, impregnated atoms. This procedure is performed inside a fume hood.

The platinum connects inside the vacuum chamber using constantan foil and copper wire. The high conductivity of copper makes a direct weld to platinum difficult, so constantan foil is used as a bridge. Constantan cut approximately 5 mm x 15 mm, folded in half with the ends spot-welded together, slides over the copper wire and is spot-welded securely, Figure D.4.

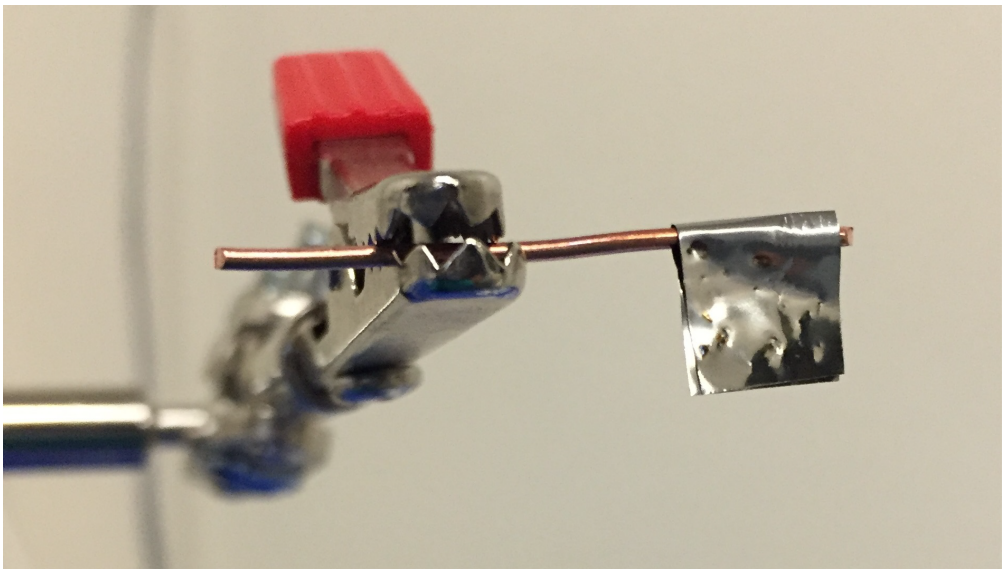

Figure D.4: Constantan foil spot-welded to copper wire. The high conductivity of copper and platinum make a direct spot weld difficult. Constantan foil is used a a bridge.

The platinum is bent into a "u" shape, and each end spot-welded to the constantan foil, figure D.5. This completes the ion source which attaches via barrel connectors to a

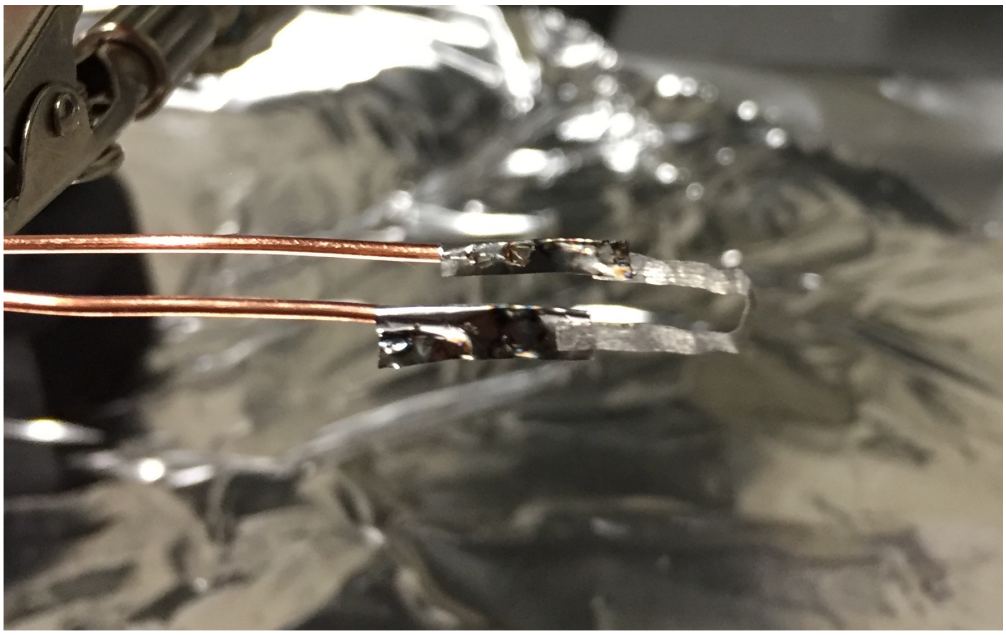

Figure D.5: Platinum spot-welded to constantan foil and copper wires.

feedthrough. The surface of platinum which the salt was deposited faces the center of the

ion trap approximately 3 mm from the outer rod edge, Figure 5.3.

D.2 Mass Spectra

Before loading an ion trap via thermionic emission, numerous filaments with various atomic species were tested using a Stanford Research Systems residual gas analyzer (RGA). All ionizing elements were removed, and the filaments mounted at the entrance of the mass filter. A channel electron multiplier (CEM) was purchased with the RGA and allowed single ion counting. Filaments were tested over a variety of temperatures (currents) and spectra of the different atomic species recorded. A plot of four spectra are shown in Figure D.6. Below

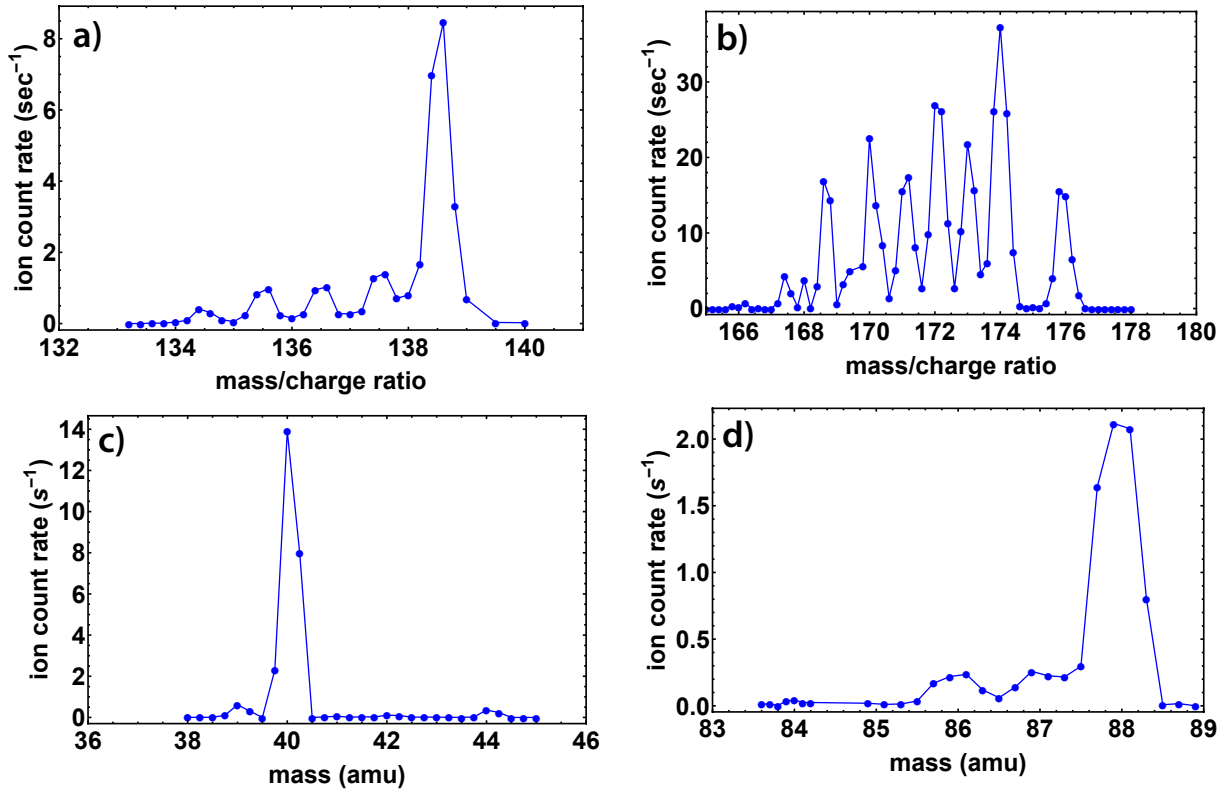

Figure D.6: Thermionic emission measured using an RGA. (a) Barium spectrum with platinum filament, (b) ytterbium spectrum with rhenium filament, (c) calcium spectrum with platinum filament, (d) strontium spectrum with platinum filament.

we highlight some of the major observations:

- Both platinum and rhenium contain impurities which diffuse from the bulk and desorb as ions. For platinum, potassium was the dominant species followed by sodium (Fig. D.7). For rhenium, potassium, sodium, and small amounts of aluminum were observed. These species would desorb at lower temperatures with larger observed count rates than the impregnated atomic species.

- Platinum sublimation was observed on various viewports and ceramic surfaces, often resulting in shorted electrodes. This motivated the switch to Rhenium, with no sublimation observed at temperatures required to produce similar ion fluxes.

- Measured ion count rates exhibited and exponential turn on with time, particularly when heated for the first time, and highly dependent of temperature.

- Adding a positive bias to the filament improved the measured count rate, and a negative bias could be used to reduce the count rate to zero.

The metal substrate contaminants were all observed to desorb at temperatures below that required for Ba^+. A filament could be heated in vacuo for multiple days to reduce count rates of unwanted species by orders of magnitude. In addition, the decay product of ^{133}Ba , ^{133}Cs, could be removed at lower temperatures. This is an important observation since no other scheme exists for removing $^{133}Cs^+$ inside the RF trap. Figure D.8 shows a plot were a platinum filament was impregnated with both barium and cesium, and monitored for several days.

We were able to increase the observed count rate of a given species impregnated in platinum with an increase in temperature until breakage of the filament. Initial experiments maximized the count rate by heating filaments to an estimated 1000 K, producing a yellow-white glow. At these temperatures platinum sublimation was observed on all nearby ceramic surfaces and windows, shorting electrodes and reducing transparency. Rhenium was tested and produced no visible sublimation at similar observed ion fluxes.

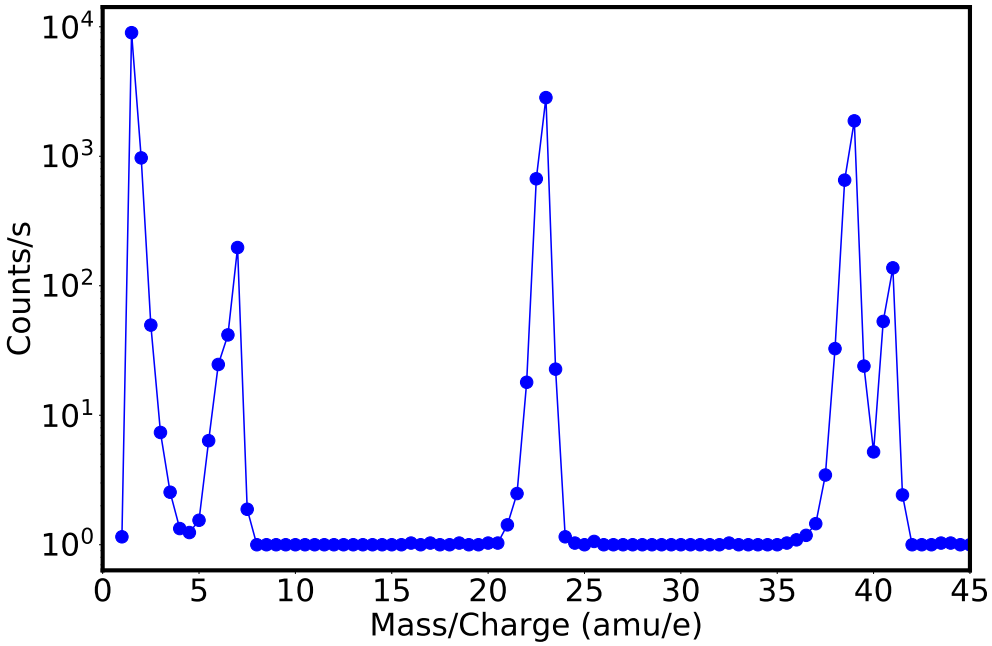

Figure D.7: Thermionic emission measured using an RGA up to 45 AMU from a platinum filament before impregnation. Potassium and sodium ions are produced in quantities equal to or larger than the impregnated atom of interest.

The exponential increase in count rate with time at a fixed temperature is thought to derive from contamination of the filament surface. Exposed to atmosphere, carbon and oxygen can deposit on the surface reducing the work function. As these species desorb, the work function is increased and ion production begins.

To reduce unwanted charging on nearby insulators and sublimation of platinum, an ion gun based on previous work was constructed [EZ82]. Effectively, an ion gun is a set of Einzel lenses, with a rendering of the design and fully constructed prototype shown in Figure D.9a, b. Using a platinum filament impregnated with naturally abundant barium, an improved count rate was observed with optimized einzel lens voltges compared to the zero voltage case (Fig D.9 c).

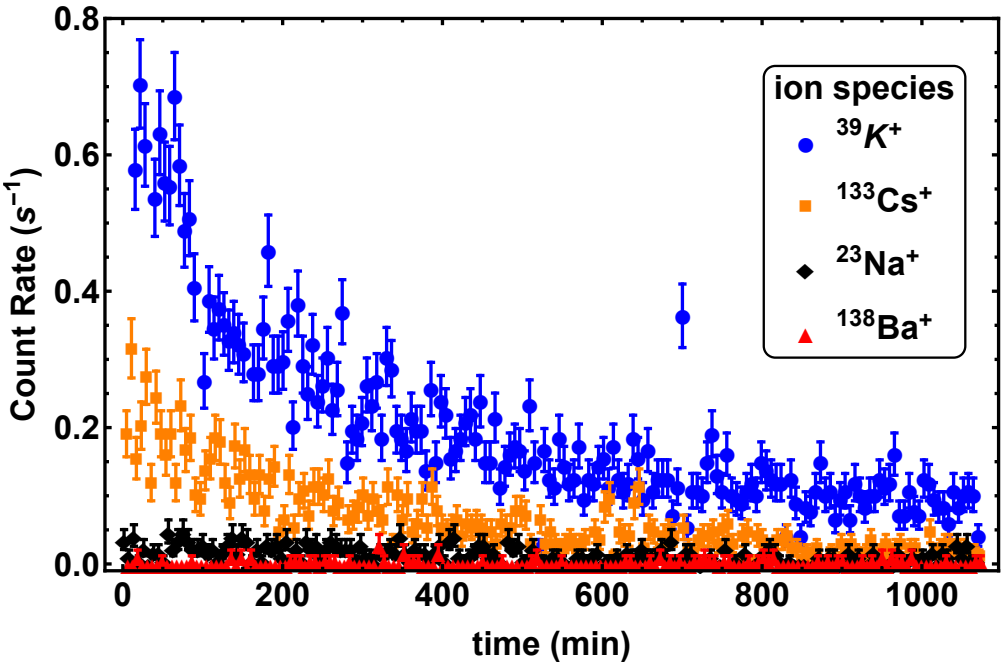

Figure D.8: Platinum filament impregnated with barium and cesium. At temperatures below significant barium desorption, impurities in the platinum as well as the cesium can be removed.

D.3 Loading

To load ions, the platinum heats to a red-orange color, a lower temperature than the impregnation step, leaving all trap voltages on. Successful loading was achieved with the filament both outside and just inside the trapping volume[2], and ions start to load as soon as the platinum becomes hot. Changing the bias on the filament between ≈ 1-5 V had no observable effect on loading rates, but did push any trapped ions away from the trap center. In addition, the current that heats the platinum produces a small voltage difference across the filament, also pushing ions away from the trap center and preventing crystallization. After removing the current, the ions returned to near the trap center. Charging is observed from nearby insulating surfaces from the isotropically emitted ion flux requiring increased compensation voltages after multiple loading attempts.

[2]The filament was placed ≈ 8 mm from the trap center when outside of the trapping volume and ≈ 3 mm from the trap center when inside the trapping volume.

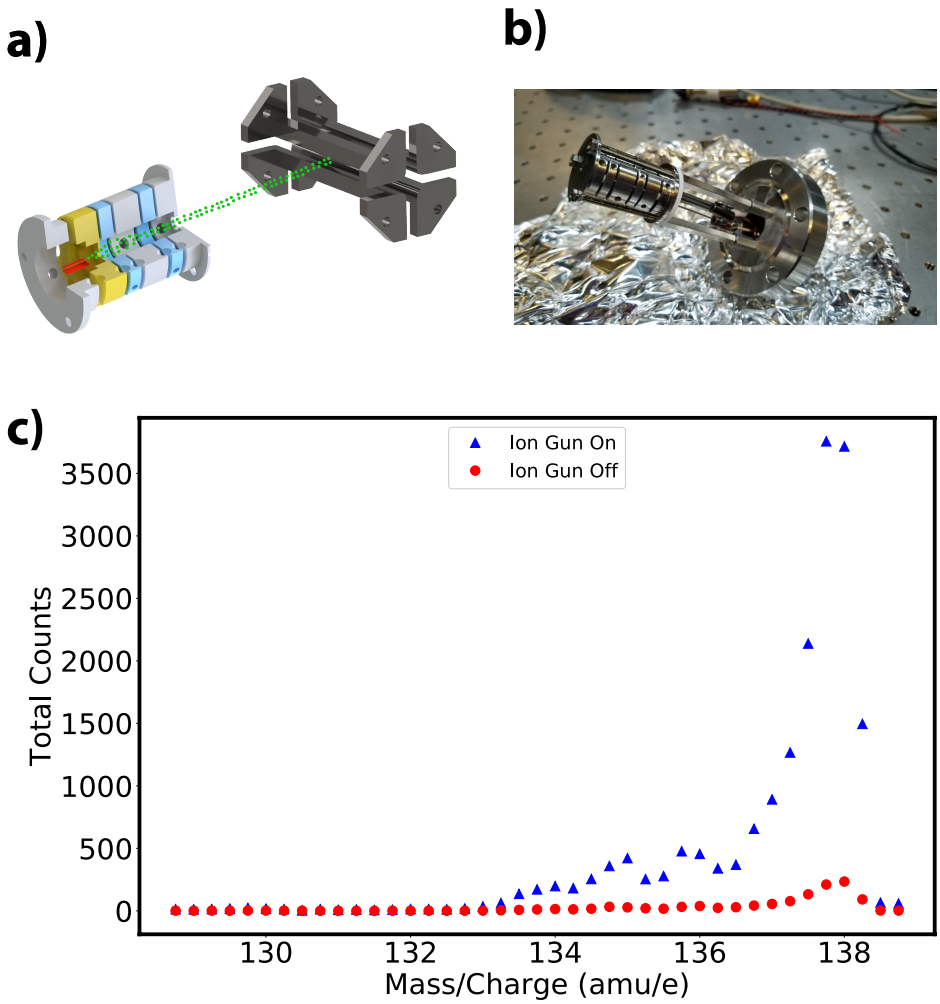

Figure D.9: (a) Rendering of ion gun and trap. (b) Constructed ion gun with platinum source. (c) Barium spectra measured with an RGA for the cases when the ion gun voltages are on or set to zero.

In addition to barium, trapped ions loaded from a platinum filament were observed with masses ranging between $\approx$ 100-270 AMU. Figure D.10 shows the various masses observed using the TOF. $BaCl^+$ has an ionization energy lower than platinum's work function, likely accounting for the mass observed near 173 AMU. The masses near 100, 115, 207, and 265 AMU were not positively identified.

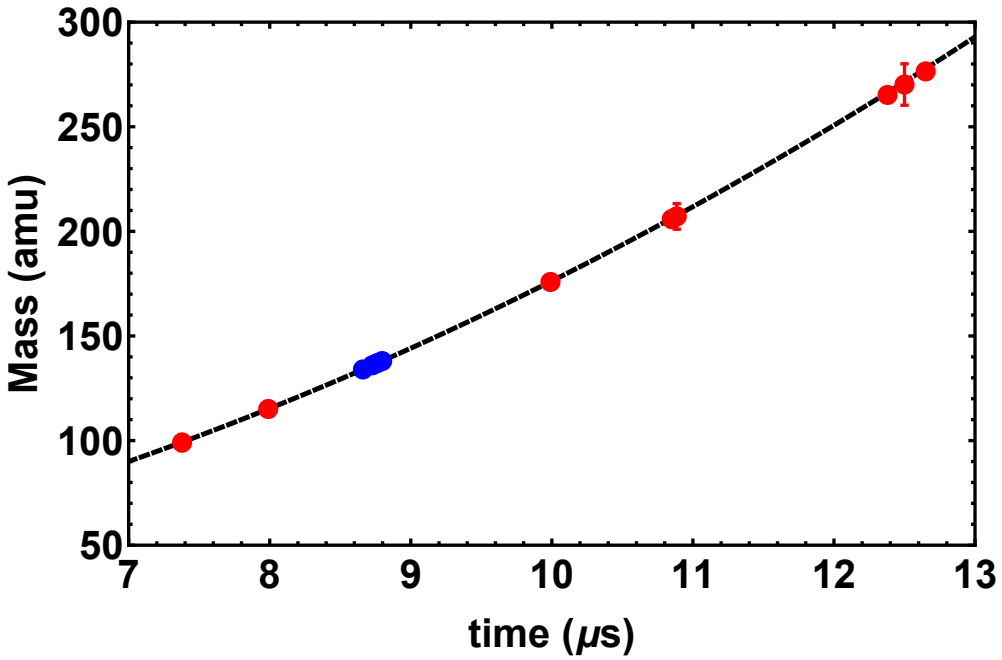

Figure D.10: Plot of mass versus arrival time measured with the TOF for charged species loaded from barium impregnated platinum filament. Blue circles represent barium isotopes. Masses near 176 amu and 207 amu are likely $BaCl^+$ and $BaCl_2^+$. Other masses could not be identified.

D.4 Summary

Successful loading of an ion trap was demonstrated via thermionic emission using a platinum filament impregnated with naturally abundant barium. While use in trapped-ion quantum information experiments would require reducing charging effects and a better understanding of the loading mechanism, other atomic physics experiments may benefit from practical advantages. Direct production of ions without the need for lasers reduce experimental complexity and costs.

In addition, laser ablation may offer an alternative to resistively heating a filament for ion production. Preliminary results have shown successful 413 nm two photon photoionization of barium atoms generated by laser ablating our naturally abundant $BaCl_2$ target. However, photoionization was not observed with similar ablation and trapping parameters when ablating the radioactive filament, possibly indicating the majority of liberated atoms

were charged.

Future concepts include a filament impregnated with many atomic species of interest, focused with an ion gun, and filtered before the trapping region. Whatever the implementation, we expect this work will find practical use in future experiments.

[ABB04] G. Audi, O. Bersillon, J. Blachot, and A. H. Wapstra. "The NUBASE evaluation of nuclear and decay properties." pp. in2p3–00020241, 2004.

[ABH06] M. Acton, K. A. Brickman, P.C. Haljan, P.J. Lee, L. Deslauriers, and C. Monroe. "Near-Perfect Simultaneous Measurement of a Qubit Register." *Quantum. Inf. Comp.*, **6**:465, 2006.

[adv] "https://advr-inc.com/ktp-phase-modulator.".

[ANH14] Carolyn Auchter, Thomas W. Noel, Matthew R. Hoffman, Spencer R. Williams, and Boris B. Blinov. "Measurement of the branching fractions and lifetime of the $5D_{5/2}$ level of Ba^+." *Phys. Rev. A*, **90**:060501, 2014.

[Arm71] L. Armstrong. "Theory of the hyperfine structure of free atoms." *Wiley-Interscience*, 1971.

[BB81] W. Becker and r. Blatt. "Precise Determination of $^{135}Ba^+$ and $^{137}Ba^+$ Hyperfine Structure." *Journal de Physique Colloques*, **42**(C8):339, 1981.

[BB02] D. J. Berkeland and M. G. Boshier. "Destabilization of dark states and optical spectroscopy in Zeeman-degenerate atomic systems." *Phys. Rev. A*, **65**:033413, Feb 2002.

[BBF20] C. H. Baldwin, B. J. Bjork, M. Foss-Feig, J. P. Gaebler, D. Hayes, M. G. Kokish, C. Langer, J. A. Sedlacek, D. Stack, and G. Vittorini. "A high fidelity light-shift gate for clock-state qubits.", 2020.

[BHL16] C. J. Ballance, T. P. Harty, N. M. Linke, M. A. Sepiol, and D. M. Lucas. "High-Fidelity Quantum Logic Gates Using Trapped-Ion Hyperfine Qubits." *Phys. Rev. Lett.*, **117**:060504, 2016.

[BKD10] D. Budker, D. F. Kimball, and D. P. DeMille. "Atomic Physics." 2010.

[BLP93] J.P. Buhler, H.W. Lenstra, and C. Pomerance. "Factoring integers with the number field sieve. In: Lenstra A.K., Lenstra H.W. (eds) The development of the number field sieve. Lecture Notes in Mathematics." *Springer, Berlin*, **1554**, 1993.

[BMB98] D. J. Berkeland, J. D. Miller, J. C. Berquist, W. M. Itano, and D. J. Wineland. "Minimization of ion micromotion in a Paul trap." *Journal of Applied Physics*, **83**:5025–5033, 1998.

[BR31] G. Breit and I. I. Rabi. "Measurement of Nuclear Spin." *Phys. Rev.*, **38**:2082–2083, Dec 1931.

[Bur10] A. H. Burrell. "High Fidelity Readout of Trapped Ion Qubits, Ph.D." 2010.

[BW82] R. Blatt and G. Werth. "Precision determination of the ground-state hyperfine splitting in $^{137}Ba^{+}$ using the ion-storage technique." *Phys. Rev. A*, **25**(3):1476, 1982.

[BXN17] A. Bermudez, X. Xu, R. Nigmatullin, J. O'Gorman, V. Negnevitsky, P. Schindler, T. Monz, U. G. Poschinger, C. Hempel, J. Home, F. Schmidt-Kaler, M. Biercuk, R. Blatt, S. Benjamin, and M. Müller. "Assessing the Progress of Trapped-Ion Processors Towards Fault-Tolerant Quantum Computation." *Phys. Rev. X*, **7**:041061, 2017.

[CCV19] Stephen Crain, Clinton Cahall, Geert Vrijsen, Emma E. Wollman, Matthew D. Shaw, Varun B. Verma, Sae Woo Nam, and Jungsang Kim. "High-speed low-crosstalk detection of a 171Yb+ qubit using superconducting nanowire single photon detectors." *Communications Physics*, **2**:97, 2019.

[cer] *"https://indico.cern.ch/event/569714/contributions/2303719/attachments/1336477/159374/Lecture*$_{2V}$*acuum*$_{S}$*ystems*$_{-VB}$*aglin*$_{-J}$*UAS*$_{2}$*017*$_{-1}$*3*$_{f}$*eb*$_{2}$*017.pdf". PhDthesis.*

[CHB85] Steven Chu, L. Hollberg, J. E. Bjorkholm, Alex Cable, and A. Ashkin. "Three-dimensional viscous confinement and cooling of atoms by resonance radiation pressure." *Phys. Rev. Lett.*, **55**:48–51, Jul 1985.

[CPL57] Bernd Crasemann, J. G. Pengra, and I. E. Lindstrom. "Radiations from Ba^{133}." *Phys. Rev.*, **108**:1500–1505, Dec 1957.

[CY95] Isaac L. Chuang and Yoshihisa Yamamoto. "Simple quantum computer." *Phys. Rev. A*, **52**:3489–3496, Nov 1995.

[CZ95] J. I. Cirac and P. Zoller. "Quantum Computations with Cold Trapped Ions." *Phys. Rev. Lett.*, **74**:4091–4094, May 1995.

[DAB06] L. Deslauriers, M. Acton, B. B. Blinov, K.-A. Brickman, P. C. Haljan, W. K. Hensinger, D. Hucul, S. Katnik, R. N. Kohn, P. J. Lee, M. J. Madsen, P. Maunz, S. Olmschenk, D. L. Moehring, D. Stick, J. Sterk, M. Yeo, K. C. Younge, and C. Monroe. "Efficient photoionization loading of trapped ions with ultrafast pulses." *Phys. Rev. A*, **74**:063421, Dec 2006.

[DBD03] J. R. De Laeter, J. K. Bohlke, P. De Bievre, H. Hidaka, H. S. Peiser, K. J. R. Rosman, and P. D P. Taylor. *Pure Appl. Chem.*, **75**:683–800, 2003.

[DBI89] F. Diedrich, J. C. Bergquist, Wayne M. Itano, and D. J. Wineland. "Laser Cooling to the Zero-Point Energy of Motion." *Phys. Rev. Lett.*, **62**:403–406, Jan 1989.

[DC13] M. V. DePalatis and M. S. Chapman. "Production of translationally cold barium monohalide ions." *Phys. Rev. A*, **88**:023403, Aug 2013.

[DDY16] Tarun Dutta, Debashis De Munshi, Dahyun Yum, Riadh Rebhi, and Manas Mukherjee. "An exacting transition probability measurement - a direct test of atomic many-body theories." *Scientific Reports*, **6**:29772, 2016.

[Deh75] H. G. Dehmelt. *Bull. Am. Phys. Soc.*, **20**:60, 1975.

[Die09] M. R. Dietrich. "Barium Ions for Quantum Computing, Ph.D. Thesis." *University of Washington*, 2009.

[DK02] Ralph G. DeVoe and Christian Kurtsiefer. "Experimental study of anomalous heating and trap instabilities in a microscopic ^{137}Ba ion trap." *Phys. Rev. A*, **65**:063407, Jun 2002.

[DKN10] M. R. Dietrich, N. Kurz, T. Noel, G. Shu, and B. B. Blinov. "Hyperfine and optical barium ion qubits." *Phys. Rev. A*, **81**:052328, 2010.

[DP97] Divincenzo D.P. "Topics in Quantum Computers." *In: Sohn L.L., Kouwenhoven L.P., Schön G. (eds) Mesoscopic Electron Transport. NATO ASI Series (Series E: Applied Sciences)*, **345**, 1997.

[DSV92] M. D. Davidson, L. C. Snoek, H. Volten, and A. Doenszelmann. "Oscillator strengths and branching ratios of transitions between low-lying levels in the barium II spectrum." *Astronomy and Astrophysics*, **255**:457–458, 1992.

[Duh92] P. Duhem. *Bulletin of the Amer*, **1**:156–168, 1892.

[Ear42] S. Earnshaw. "On the nature of the molecular forces which regulate the constitution of the luminferous ether." *Trans. Camb. Phil. Soc*, **7**:97–112, 1842.

[EWP19] A. Erhard, J.J. Wallman, L. Postler, M. Meth, R. Stricker, E. A. Martinez, P. Schindler, T. Monz, J. Emerson, and R. Blatt. "Characterizing large-scale quantum computers via cycle benchmarking." *Nature Communications*, **10**:5347, 2019.

[EZ] Eckert and Ziegler. *https://www.ezag.com/home/products/isotope$_p$roducts/*.

[EZ82] Peter W. Erdman and Edward C. Zipf. "Low-voltage, high-current electron gun." *Review of Scientific Instruments*, **53**(2):225–227, 1982.

[Fis97] Peter T H Fisk. "Trapped-ion and trapped-atom microwave frequency standards." *Reports on Progress in Physics*, **60**(8):761–817, 1997.

[FMM12] Austin G. Fowler, Matteo Mariantoni, John M. Martinis, and Andrew N. Cleland. "Surface codes: Towards practical large-scale quantum computation." *Phys. Rev. A*, **86**:032324, 2012.

[Foo12] C. J. Foot. "Atomic Physics." 2012.

[GBB07] J. Gurell, E. Biémont, K. Blagoev, V. Fivet, P. Lundin, S. Mannervik, L.-O. Norlin, P. Quinet, D. Rostohar, P. Royen, and P. Schef. "Laser-probing measurements and calculations of lifetimes of the $5d\,^2D_{32}$ and $5d\,^2D_{52}$ metastable levels in Ba II." *Phys. Rev. A*, **75**:052506, May 2007.

[Gho95] P. K. Ghosh. "Ion Traps." *Clarendon Press, Oxford*, 1995.

[GKP01] Daniel Gottesman, Alexei Kitaev, and John Preskill. "Encoding a qubit in an oscillator." *Phys. Rev. A*, **64**:012310, Jun 2001.

[GKS76] Vittorio Gorini, Andrzej Kossakowski, and E. C. G. Sudarshan. "Completely positive dynamical semigroups of N-level systems." *Journal of Mathematical Physics*, **17**(5):821–825, 1976.

[Gri05] D. J. Griffiths. "Introduction to Quantum Mechanics." *Pearson Prentice Hall*, 2005.

[Gro96] L.k. Grover. "A fast quantum mechanical algorithm for database search." *Proceedings, 28th Annual ACM Symposium on the Theory of Computing*, p. 212, 1996.

[GTL16] J. P. Gaebler, T. R. Tan, Y. Lin, Y. Wan, R. Bowler, A. C. Keith, S. Glancy, K. Coakley, E. Knill, D. Leibfried, and D. J. Wineland. "High-Fidelity Universal Gate Set for $^{9}Be^{+}$ Ion Qubits." *Phys. Rev. Lett.*, **117**:060505, Aug 2016.

[HAB14] T. P. Harty, D. T. C. Allcock, C. J. Ballance, L. Guidoni, H. A. Janacek, N. M. Linke, D. N. Stacey, and D. M. Lucas. "High-Fidelity Preparation, Gates, Memory, and Readout of a Trapped-Ion Quantum Bit." *Phys. Rev. Lett.*, **113**:220501, 2014.

[HBB82] M. Van Hove, G. Borghs, P. De Bisschop, and R. E. Silverans. "J-dependent isotope shifts in the 5d 2 D J doublet of barium II." *Journal of Physics B: Atomic and Molecular Physics*, **15**(12):1805, 1982.

[HEG95] K. G. Heumann, S. Eisenhut, S. Gallus, E. H. Hebeda, R. Nusko, A. Vengosh, and T. Walczyk. "Recent developments in thermal ionization mass spectrometric techniques for isotope analysis: a review." *Analyst*, **120**, 1995.

[HHM76] C. Höhle, H. Hühnermann, Th. Meier, H.R. Ihle, and R. Wagner. "Nuclear moments and optical isotope shift of radioactive 133Ba." *Physics Letters B*, **62**(4):390 – 392, 1976.

[Hig14] High Finesse. *WS Ultimate 2 User Manual*, 2014.

[HS74] K. Heilig and A. Steudel. *Atomic Data and Nuclear Data Tables*, **14**:613–638, 1974.

[JND85] G. Janik, W. Nagourney, and H. Dehmelt. "Doppler-free optical spectroscopy on the Ba+ mono-ion oscillator." *J. Opt. Soc. Am. B*, **2**(8):1251–1257, Aug 1985.

[Jon08] T. Jones. "Mathieu Equations and the Ideal RF-Paul Trap." *https://www.physics.drexel.edu/ tim/open/mat/mat.html*, 2008.

[Kap51] P. L. Kapitsa. *Zh. Eksp. Teor. Fiz.*, **34**:242, 1951.

[KCA11] A. Keselman, Y. Clickman, N. Akerman, S. Kotler, and R. Ozeri. "High-Fidelity State Detection and Tomography of a Single Ion Zeeman Qubit." *New J. Phys.*, **13**:073027, 2011.

[KHS12] Adam Kleczewski, Matthew R. Hoffman, J. A. Sherman, Eric Magnuson, B. B. Blinov, and E. N. Fortson. "Coherent excitation of the $6S_{1/2}$ to $5D_{3/2}$ electric-quadrupole transition in $^{138}Ba^{+}$." *Phys. Rev. A*, **85**:043418, Apr 2012.

[Kin63] W. H. King. "Comments on the Article "Peculiarities of the Isotope Shift in the Samarium Spectrum"." *J. Opt. Soc. Am.*, **53**(5):638–639, May 1963.

[Kin84] W. H. King. "Isotope Shifts in Atomic Spectra." *Springer*, 1984.

[Kin99] B. E. King. "Quantum State Engineering and Information Processing with Trapped Ions. PhD." *University of Colorado, Boulder*, 1999.

[KMM00] H. Kawano, H. Mine, M. Moriyama, M. Tanigawa, and Y. Zhu. "Selection of the substrate metal best for thermal positive ionization." *Review of Scientific Instruments*, **71**(2):856–858, 2000.

[KSW87] H. Knab, M. Schupp, and G. Werth. "Precision Spectroscopy on Trapped Radioactive Ions: Ground-State Hyperfine Splittings of $^{133}Ba^{+}$ and $^{131}Ba^{+}$." *Europhys. Lett.*, **4**(12):1361, 1987.

[Lan06] C.E. Langer. *High-fidelity quantum information processing with trapped ions*. PhD thesis, University of Colorado, Boulder, 2006.

[LD98] Daniel Loss and David P. DiVincenzo. "Quantum computation with quantum dots." *Phys. Rev. A*, **57**:120–126, Jan 1998.

[Lin76] G. Linblad. "On the generators of quantum dynamical semigroups." *Commun. Math. Phys*, **119**:48, 1976.

[LMH16] Regina Lechner, Christine Maier, Cornelius Hempel, Petar Jurcevic, Ben P. Lanyon, Thomas Monz, Michael Brownnutt, Rainer Blatt, and Christian F. Roos. "Electromagnetically-induced-transparency ground-state cooling of long ion strings." *Phys. Rev. A*, **93**:053401, May 2016.

[LWC19] Pei Jiang Low, Brendan M. White, Andrew A. Cox, Matthew L. Day, and Crystal Senko. "Practical trapped-ion protocols for universal qudit-based quantum computing.", 2019.

[MCB94] I. Marzoli, J. I. Cirac, R. Blatt, and P. Zoller. "Laser cooling of trapped three-level ions: Designing two-level systems for sideband cooling." *Phys. Rev. A*, **49**:2771–2779, Apr 1994.

[MEK00] Giovanna Morigi, Jürgen Eschner, and Christoph H. Keitel. "Ground State Laser Cooling Using Electromagnetically Induced Transparency." *Phys. Rev. Lett.*, **85**:4458–4461, Nov 2000.

[MHP01] A. P. Meshik, C. M. Hohenberg, O. V. Pravdivtseva, and Ya. S. Kapusta. "Weak decay of ^{130}Ba and ^{132}Ba : Geochemical measurements." *Phys. Rev. C*, **64**:035205, 2001.

[min] "https://amplitude-laser.com/wp-content/uploads/2019/01/Minilite.pdf.".

[MMK95] C. Monroe, D. M. Meekhof, B. E. King, W. M. Itano, and D. J. Wineland. "Demonstration of a Fundamental Quantum Logic Gate." *Phys. Rev. Lett.*, **75**:4714–4717, Dec 1995.

[MS90] A. A. Madej and J. D. Sankey. "Quantum jumps and the single trapped barium ion: Determination of collisional quenching rates for the $5d^2D_{5/2}$ level." *Phys. Rev. A*, **41**:2621–2630, Mar 1990.

[MSW08] A. H. Myerson, D. J. Szwer, S. C. Webster, D. T. C. Allcock, M. J. Curtis, G. Imreh, J. A. Sherman, D. N. Stacey, A. M. Steane, and D. M. Lucas. "High-Fidelity Readout of Trapped-Ion Qubits." *Phys. Rev. Lett.*, **100**:200502, 2008.

[NDM11] S. Narayanan, N. Daniilidis, S. A. Möller, R. Clark, F. Ziesel, K. Singer, F. Schmidt-Kaler, and H. Häffner. "Electric field compensation and sensing with a single ion in a planar trap." *Journal of Applied Physics*, **110**(11):114909, 2011.

[Nei77] R.D. Neirincky. "Production of 133mBa for medical purposes." *The International Journal of Applied Radiation and Isotopes*, **28**(3):323 – 325, 1977.

[NHT78] W. Neuhauser, M. Hohenstatt, P. Toschek, and H. Dehmelt. "Optical-Sideband Cooling of Visible Atom Cloud Confined in Parabolic Well." *Phys. Rev. Lett.*, **41**:233–236, 1978.

[NHT80] W. Neuhauser, M. Hohenstatt, P. E. Toschek, and H. Dehmelt. "Localized visible Ba^+ mono-ion oscillator." *Phys. Rev. A*, **22**:1137–1140, 1980.

[nis] *https://physics.nist.gov/PhysRefData/XrayMassCoef/ElemTab/z82.html.*

[NPT99] Y. Nakamura, Yu A. Pashkin, and J. S. Tsai. "Coherent control of macroscopic quantum states in a single-Cooper-pair box." *Nature*, **398**(6730):786–788, 1999.

[nrc] *https://www.nrc.gov/about-nrc/radiation/around-us/doses-daily-lives.html.*

[NSD86] Warren Nagourney, Jon Sandberg, and Hans Dehmelt. "Shelved optical electron amplifier: Observation of quantum jumps." *Phys. Rev. Lett.*, **56**:2797–2799, Jun 1986.

[NVG13] Rachel Noek, Geert Vrijsen, Daniel Gaultney, Emily Mount, Taehyun Kim, Peter Maunz, and Jungsang Kim. "High speed, high fidelity detection of an atomic hyperfine qubit." *Opt. Lett.*, **38**:4735–4738, 2013.

[ORF88] T Olsson, A Rosén, B Fricke, and G Torbohm. "Analysis of the electronic structure, hyperfine structure, and volume isotope shifts in the low lying states of Ba I and Ba II." *Physica Scripta*, **37**(5):730–741, may 1988.

[OYM07] S. Olmschenk, K. C. Younge, D. L. Moehring, D. N. Matsukevich, P. Maunz, and C. Monroe. "Manipulation and detection of a trapped Yb^+ hyperfine qubit." *Phys. Rev. A*, **76**:052314, 2007.

[Pau90] W. Paul. "Electromagnetic traps for charged and neutral particles." *Reviews of Modern Physics*, **62**:3, 1990.

[PK15] Thaned Pruttivarasin and Hidetoshi Katori. "Compact field programmable gate array-based pulse-sequencer and radio-frequency generator for experiments with trapped atoms." *Review of Scientific Instruments*, **86**:115106, 2015.

[POF58] W. Paul, O. Osberghaus, and E. Fischer. *Forschungsber. Wirtsch. Verkehrsminist.*, **415**, 1958.

[Pre97] J. Preskill. "FAULT-TOLERANT QUANTUM COMPUTATION." *Introduction to Quantum Computation and Information*, pp. 213–269, 1997.

[Pru14] T. Pruttivarasin. "Spectroscopy, fundamental symmetry tests and quantum simulation with trapped ions. PhD." *University of California, Berkeley*, 2014.

[PTH88] C. R. Phipps, T. P. Turner, R. F. Harrison, G. W. York, W. Z. Osborne, G. K. Anderson, X. F. Corlis, L. C. Haynes, H. S. Steele, K. C. Spicochi, and T. R. King. "Impulse coupling to targets in vacuum by KrF, HF, and CO2 single-pulse lasers." *Journal of Applied Physics*, **64**(3):1083–1096, 1988.

[pyt] *https://www.python.org/.*

[RGL07] P. Royen, J. Gurell, P. Lundin, L.-O. Norlin, and S. Mannervik. "Monitoring the weak collisional excitation of a stored ion beam reveals the radiative decay rate of extremely long-lived metastable levels." *Phys. Rev. A*, **76**:030502, Sep 2007.

[RHC10] C. A. Ryan, J. S. Hodges, and D. G. Cory. "Robust Decoupling Techniques to Extend Quantum Coherence in Diamond." *Phys. Rev. Lett.*, **105**:200402, 2010.

[ROW05] B Roth, A Ostendorf, H Wenz, and S Schiller. "Production of large molecular ion crystals via sympathetic cooling by laser-cooled Ba." *Journal of Physics B: Atomic, Molecular and Optical Physics*, **38**(20):3673–3685, sep 2005.

[RSS13] Wade G. Rellergert, Scott T. Sullivan, Steven J. Schowalter, Svetlana Kotochigova, Kuang Chen, and Eric R. Hudson. "Evidence for sympathetic vibrational cooling of translationally cold molecules." *Nature*, **495**(7442):490–494, 2013.

[SAD16] R L da Silva, M C M de Almeida, J U Delgado, R Poledna, A Santos, E V de Veras, J Rangel, and O L Trindade. "Metrological activity determination of133Ba by sum-peak absolute method." *Journal of Physics: Conference Series*, **733**:012095, jul 2016.

[SBD80] R. E. Silverans, G. Borghs, G. Dumont, and J. M. Van den Cruyce. "Collinerar Fast Beam-Laser Spectroscopy on $5d^2D_{3/2,5/2}$ Barium Ions." *Z. Physik A - Atoms and Nuclei*, **295**:311–314, 1980.

[SD12] C Shen and L-M Duan. "Correcting detection errors in quantum state engineering through data processing." *New Journal of Physics*, **14**:053053, may 2012.

[SDC16] Steven J. Schowalter, Alexander J. Dunning, Kuang Chen, Prateek Puri, Christian Schneider, and Eric R. Hudson. "Blue-sky bifurcation of ion energies and the limits of neutral-gas sympathetic cooling of trapped ions." *Nature Communications*, **7**(1):12448, 2016.

[SGS06] N. D. Scielzo, J. R. Guest, E. C. Schulte, I. Ahmad, K. Bailey, D. L. Bowers, R. J. Holt, Z.-T. Lu, T. P. O'Connor, and D. H. Potterveld. "Measurement of the lifetimes of the lowest $^3P_1$ state of neutral Ba and Ra." *Phys. Rev. A*, **73**:010501, Jan 2006.

[SHL14] Christopher M. Seck, Edward G. Hohenstein, Chien-Yu Lien, Patrick R. Stollenwerk, and Brian C. Odom. "Rotational state analysis of AlH+ by two-photon dissociation." *Journal of Molecular Spectroscopy*, **300**:108 – 111, 2014. Spectroscopic Tests of Fundamental Physics.

[Sho94] P. W. Shor. "Algorithms for quantum computation: discrete logarithms and factoring." In *Proceedings 35th Annual Symposium on Foundations of Computer Science*, pp. 124–134, 1994.

[SKD16] Christopher M. Seck, Mark G. Kokish, Matthew R. Dietrich, and Brian C. Odom. "Raman sideband cooling of a $^{138}Ba^+$ ion using a Zeeman interval." *Phys. Rev. A*, **93**:053415, May 2016.

[SM89] J. D. Sankey and A. A. Madej. "The production of ions for single-ion traps." *Appl. Phys. B*, **49**:69–72, 1989.

[SSC14] Christian Schneider, Steven J. Schowalter, Kuang Chen, Scott T. Sullivan, and Eric R. Hudson. "Laser-Cooling-Assisted Mass Spectrometry." *Phys. Rev. Applied*, **2**:034013, Sep 2014.

[SSY16] Christian Schneider, Steven J. Schowalter, Peter Yu, and Eric R. Hudson. "Electronics of an ion trap with integrated time-of-flight mass spectrometer." *International Journal of Mass Spectrometry*, **394**:1 – 8, 2016.

[Sto05] N. J. Stone. "Table of nuclear magnetic dipole and electric quadrupole moments." *Atomic Data and Nuclear Data Tables*, **90**:75–176, 2005.

[SZB18] Tomasz P. Sakrejda, Liudmila Zhukas, and Boris B. Blinov. "Effcient sympathetic cooling in mixed barium and ytterbium ion chains.", 2018.

[Tam96] C. Tamm. "Talk presented in Proceedings of the Fifth Symposium on Frequency Standards and Metrology, edited by C. Bergquist (unpublished)." *World Scientific, Singapore*, 1996.

[ucs] *https://ehs.ucsd.edu/rad/radionuclide/Ba-133.pdf*.

[VAH93] P. Villemoes, A. Arnesen, F. Heijkenskjold, and A. Wannstrom. "Isotope shifts and hyperfine structure of134-138Ba II by fast ion beam-laser spectroscopy." *Journal of Physics B: Atomic, Molecular and Optical Physics*, **26**(22):4289–4299, nov 1993.

[VBB85] M. Van Hove, G. Borgs, P. Bisschop, and R. E. Silverans. "Hyperfine Structure of $5d^2D_{3/2}^{135,137}$ Ba Ions by Collinear Fast Beam Laser-rf Double Resonance Spectroscopy." *Z. Phys. A - Atoms and Nuclei*, **321**:215–219, 1985.

[WAB84] K. Wendt, S. A. Ahmad, F. Buchinger, A. C. Mueller, R. Neugart, and E. W. Otten. *Z. Phys. A - Atoms and Nuclei*, **318**:125–129, 1984.

[WBG08] A. L. Wolf, S. A. van den Berg, C. Gohle, E. J. Salumbides, W. Ubachs, and K. S. E. Eikema. "Frequency metrology on the $4s\,^2S_{12} - -4p\,^2P_{12}$ transition in $^{40}Ca^+$ for a comparison with quasar data." *Phys. Rev. A*, **78**:032511, Sep 2008.

[WD75] D. J. Wineland and H. Dehmelt. "Proposed $10^{14}\delta\nu/\nu$ Laser Fluorecscence Spectroscopy on Ti^+ Mono-Ion Oscillator." *Bull. Am. Phys. Soc.*, **20**:637, 1975.

[WH00] P. R. Willmott and J. R. Huber. "Pulsed laser vaporization and deposition." *Rev. Mod. Phys.*, **72**:315–328, Jan 2000.

[WM55] W. C. Wiley and I. H. McLaren. "Time of Flight Mass Spectrometer with Improved Resolution." *Review of Scientific Instruments*, **26**(12):1150–1157, 1955.

[WMI98] D. J. Wineland, C. Monroe, W. M. Itano, D. Leibfried, B. E. King, and D. M. Meekhof. "Experimental Issues in Coherent Quantum-State Manipulation of Trapped Atomic Ions." *J. Res. Natl. Inst. Stand. Technol.*, **103**(3):259–328, 1998.

[Woo18] G. K. Woodgate. "Elementary Atomic Structure." *Oxsford Science Publications*, **11**:646, 2018.

[WS75] Hänsch T. W. and A. L. Schawlow. "Cooling of Gases by Laser Radiation." *Opt. Commun.*, **13**:68–71, 1975.

[WUZ17] Ye Wang, Mark Um, Junhua Zhang, Shuoming An, Ming Lyu, Jing-Ning Zhang, L.-M. Duan, Dahyun Yum, and Kihwan Kim. "Single-qubit quantum memory exceeding ten-minute coherence time." *Nature Photonics*, **11**:646–650, 2017.

[YND97] N. Yu, W. Nagourney, and H. Dehmelt. "Radiative Lifetime Measurement of the Ba^+ Metastable $D_{3/2}$ State." *Phys. Rev. Lett.*, **78**:4898–4901, Jun 1997.